Diffusion Microscopist Simulator - The Development and Application of a Monte Carlo Simulation System for Diffusion MRI

Chun Hung Yeh

Diffusion Microscopist Simulator

- The Development and Application of a Monte Carlo Simulation System for Diffusion MRI

A Joint Dissertation Submitted to
Department of Biomedical Imaging and Radiological Sciences,
National Yang-Ming University, Taiwan; and
Graduate School of Sciences and Technologies of Information,
Telecommunications, and Systems, Paris-Sud XI University, France;
In Partial Fulfillment of the Requirements for the
Doctor of Philosophy Degree in Physics and Biomedical Imaging

Chun-Hung Yeh

Reviewers	Daniel Alexander	University College London, United Kingdom
	Jason Jeun-Shenn Lee	National Yang-Ming University, Taiwan
Examiners	Emmanuel Durand	Paris-Sud XI University, France
	Denis Le Bihan	CEA NeuroSpin, France
	Jean-François Mangin	CEA NeuroSpin, France
Supervisors	Ching-Po Lin	National Yang-Ming University, Taiwan
	Cyril Poupon	CEA NeuroSpin, France

September 2011

Diffusion Microscopist Simulator

- Développement et Application d'un Simulateur de Monte Carlo pour l'IRM de Diffusion

Thèse de Doctorat en Cotutelle entre
Department of Biomedical Imaging and Radiological Sciences,
National Yang-Ming University, Taiwan; et l'Ecole Doctorale,
Sciences et Technologies de l'Information des Télécommunications
et des Systèmes, Université Paris-Sud XI, France;
Pour Obtenir le Titre de DOCTEUR EN SCIENCES

Chun-Hung Yeh

Rapporteurs	Daniel Alexander	University College London, United Kingdom
	Jason Jeun-Shenn Lee	National Yang-Ming University, Taiwan
Examinateurs	Emmanuel Durand	Université Paris-Sud XI, France
	Denis Le Bihan	CEA NeuroSpin, France
	Jean-François Mangin	CEA NeuroSpin, France
Directeurs	Ching-Po Lin	National Yang-Ming University, Taiwan
	Cyril Poupon	CEA NeuroSpin, France

Septembre 2011

Abstract

Diffusion magnetic resonance imaging (dMRI) has made a significant breakthrough in neurological disorders and brain research thanks to its exquisite sensitivity to tissue cytoarchitecture. However, as the water diffusion process in neuronal tissues is a complex biophysical phenomena at molecular scale, it is difficult to infer tissue microscopic characteristics on a voxel scale from dMRI data. The major methodological contribution of this thesis is the development of an integrated and generic Monte Carlo simulation framework, 'Diffusion Microscopist Simulator' (DMS), which has the capacity to create 3D biological tissue models of various shapes and properties, as well as to synthesize dMRI data for a large variety of MRI methods, pulse sequence design and parameters. DMS aims at bridging the gap between the elementary diffusion processes occurring at a micrometric scale and the resulting diffusion signal measured at millimetric scale, providing better insights into the features observed in dMRI, as well as offering ground-truth information for optimization and validation of dMRI acquisition protocols for different applications.

We have verified the performance and validity of DMS through various benchmark experiments, and applied to address particular research topics in dMRI. Based on DMS, there are two major application contributions in this thesis. First, we use DMS to investigate the impact of finite diffusion gradient pulse duration (δ) on fibre orientation estimation in dMRI. We propose that current practice of using long δ, which is enforced by the hardware limitation of clinical MRI scanners, is actually beneficial for mapping fibre orientations, even though it violates the underlying assumption made in q-space theory. Second, we employ DMS to investigate the feasibility of estimating axon radius using a clinical MRI system. The results suggest that the algorithm for mapping the direct microstructures is applicable to dMRI data acquired from standard MRI scanners.

Keywords: Diffusion MRI; Monte Carlo simulation; MRI pulse sequence; Tissue model; Microstructure; Validation;

Abstract (Français)

L'imagerie par résonance magnétique de diffusion (IRMd) a fait une percée significative dans les troubles neurologiques et les recherches sur le cerveau grâce à son extraordinaire sensibilité à la cytoarchitecture des tissus. Cependant, comme le processus de diffusion de l'eau dans les tissus neuronaux est un phénomène biophysique complexe à l'échelle moléculaire, il est difficile d'en déduire les caractéristiques microscopiques des tissus à l'échelle du voxel, à partir des données d'IRMd. La contribution méthodologique majeure de cette thèse est le développement d'un cadre de simulation de type Monte Carlo intégré et générique, appelé 'Diffusion Microscopist Simulator' (DMS), qui permet d'élaborer des modèles de tissus biologiques tridimensionnels aux géométries et propriétés variées et qui permet de synthétiser des données d'IRMd correspondantes pour une grande variété d'IRM, de séquences d'impulsions et de paramètres. L'outil DMS vise à combler le fossé entre les processus de diffusion élémentaires, qui se produisent à une échelle micrométrique, et le signal de diffusion résultant, mesuré à l'échelle millimétrique, qui offre un meilleur aperçu des caractéristiques observées dans l'IRMd, tout en offrant une information vérité terrain pour l'optimisation et la validation des protocoles d'acquisition de l'IRMd pour différentes applications.

Nous avons vérifié les performances et la validité du simulateur à travers différents tests, et appliqué cet outil pour aborder des thèmes de recherche particuliers à l'IRMd. Il y a deux contributions majeures dans cette thèse. Tout d'abord, nous avons utilisé l'outil DMS pour étudier l'impact de la durée d'impulsions de gradient de diffusion finies (δ) sur l'estimation de l'orientation des fibres par l'IRMd. Nous avons démontré que la pratique actuelle qui utilise un δ long, imposée par la limitation physique des scanners d'IRM cliniques, est en fait bénéfique pour la cartographie des orientations des fibres, même si elle viole l'hypothèse sous-jacente faite dans la théorie de l'espace q. Deuxièmement, nous avons employé le simulateur pour étudier la possibilité d'estimer le rayon des axones en utilisant un système d'IRM clinique. Les résultats suggèrent que la technique d'inférence de la taille des axones reposant sur un modèle analytique de la réponse IRM d'un axone au processus de diffusion est applicable aux données d'IRMd acquises avec des scanners IRM standards.

Mots-clés: IRM de diffusion; Simulation Monte Carlo; Séquence IRM; Modèle de tissu; Microstructure; Validation;

Contents

List of Figures

List of Tables

List of Symbols

δ	Diffusion gradient pulse duration
Δ	Diffusion time
Δ_e	Effective diffusion time
N_i	Number of iteration
N_p	Number of particles
t_s	Time step
2D	2-dimensional
3D	3-dimensional
ADC	Apparent diffusion coefficient
BOLD	Blood-oxygen level dependent
CNS	Central nervous system
CHARMED	Composite hindered and restricted model of diffusion
DMS	Diffusion microscopist simulator
dfMRI	Diffusion functional magnetic resonance imaging
dMRI	Diffusion magnetic resonance imaging
DOT	Diffusion orientation transform
DPI	Diffusion propagator imaging
DSI	Diffusion spectrum imaging
DTI	Diffusion tensor imaging
DT	Diffusion tensor
DW	Diffusion weighted
FA	Fractional anisotropy
FOD	Fibre orientation distribution
fODF	Fibre orientation distribution function
FOV	Field of view
FT	Fourier transform
HARDI	High angular resolution diffusion imaging
MC	Monte Carlo
MCMC	Markov Chain Monte Carlo
MD	Mean diffusivity
MR	Magnetic resonance
MRI	Magnetic resonance imaging
MSDI	Multiple scattering diffusion imaging
NMR	Nuclear magnetic resonance
OGSE	Oscillating gradient spin echo

PAS-MRI	Persistant angular structure MRI
PDF	Probability density function
PGSE	Pulsed gradient spin echo
QBI	Q-ball imaging
RF	Radiofrequency
RMS	Root mean square
SDT	Sharpening deconvolution transform
SGP	Short gradient pulse
SNR	Signal-to-noise ratio
SR	Slew rate
STE	Stimulated echo
T_1	Spin-lattice relaxation time
T_2	Spin-spin relaxation time
TE	Echo time
T_M	Mixing time
TR	Repetition time
TRSE	Twice refocused spin echo

Résumé

Préface

Pour l'être humain, l'eau semble statique à l'oeil nu, cependant à l'échelle microscopique les molécules d'eau apparaissent en état d'oscillation dynamique. Ce mouvement aléatoire de molécule, appelé mouvement brownien, fut observé en 1827 par le botaniste Robert Brown à partir de grains de pollen en suspension dans de l'eau [Brown (1828)]. Il devint alors évident que la diffusion moléculaire dans les liquides et les gaz est la conséquence de l'énergie thermique stockée par les molécules [Einstein (1905)].

Imaginons que nous puissions marquer une molécule d'eau au sein d'un tissu cérébral et garder la trace de son mouvement dû à la diffusion. Nous pourrions alors constater que son parcours épouserait la forme de la géométrie des tissus cérébraux. Ceci permet d'appréhender le concept de base de l'imagerie par résonance magnétique de diffusion (IRMd). Cette technique utilise le déplacement microscopique naturel des molécules d'eau ayant lieu dans les tissus cérébraux de manière à obtenir une cartographique quantitative de paramètres de la la microstructure du tissu cérébral. L'IRMd utilise également les molécules d'eau comme un traceur endogène pouvant mettre en évidence des détails microscopiques de l'architecture des tissus qu'ils soient sains ou pathologiques.

L'IRM de diffusion est apparue au milieu des années 1980 [Wesbey et al. (1984a,b); Le Bihan et al. (1986)] et a est devenue au cours des 25 dernières années un outil IRM incontourable pour étudier le système nerveux central (CNS). Son application clinique est majeure pour le diagnostic des troubles neurologiques, en particulier pour la prise en charge des patients atteints d'accidents vasculaires cérébraux ou d'ischémies au stade aigu. L'IRMd est rapidement devenue un standard pour l'étude des pathologies de la substance blanche (WM) grâce à l'imagerie du tenseur de diffusion (DTI) qui permet de révéler les anomalies structurelles des faisceaux de fibres la constituant,

mais également grâce aux remarquables cartographies de la connectivité cérébrale qu'elle permet d'obtenir. [Basser et al. (1994a,b); Conturo et al. (1999); Mori et al. (1999); Basser et al. (2000); Poupon et al. (2000)]. Sa capacité à révéler la connectivité anatomique reliant les différentes aires du cerveau, de manière non invasive et à l'échelle du sujet, est apparue comme une découverte majeure pour les neurosciences. Plus récemment, il a été démontré que l'IRMd pouvait également être utilisée pour établir directement les caractéristiques de la microstructure du cerveau [Alexander (2008); Assaf et al. (2008)] ainsi que pour détecter les changements des tissus cérébraux associés à l'activité neuronale [Le Bihan et al. (2006)].

Motivations & Objectifs

IRM de Diffusion et Microstructure des Tissus - Un Problème d'Echelle

Le principe de base de l'IRM de diffusion (IRMd) est d'observer les déplacements microscopiques naturels des molécules d'eau ayant lieu dans les tissus cérébraux. Les molécules d'eau peuvent alors être utilisées comme un vecteur permettant de mettre en évidence les détails microscopiques de l'architecture des tissus sains ou pathologiques. Il faut cependant garder à l'esprit que le signal global observé à une résolution *millimètrique* sur les images IRM résulte de l'intégration statistique de toutes les distributions de déplacement *microscopique* des molécules d'eau présentes en chaque voxel. Les processus complexes de diffusion ayant lieu dans un tissu biologique à l'échelle d'un voxel sont souvent décrits par une mesure moyenne de leur mobilité: le Coefficient de Diffusion Apparent (ADC) [Le Bihan et al. (1986)]. L'utilisation de l'ADC global pour représenter le processus de diffusion permet de représenter les processus physiques ayant lieu à une échelle plus petite que celle de la méthode d'acquisition. L'échelle la plus grande est imposée par des limites techniques (par exemple l'IRM) tandis que l'échelle du théâtre des processus biophysiques élémentaires est déterminée par les phénomènes physiques à l'échelle moléculaire. L'effet de lissage moyen dû à cette mise à l'échelle nécessite un *a priori* sur la géométrie membranaire en chaque voxel, ce qui rend difficile l'interprétation physique directe à partir de ce paramètre global à moins que l'on puisse faire certaines hypothèses. L'ADC du cerveau est 2 à 10 fois plus petit que celle de l'eau libre en solution aqueuse [Le Bihan (2003)]. La diminution de la diffusion de l'eau dans le milieu intra-cellulaire s'explique souvent par une viscosité importante, l'encombrement moléculaire et les effets de restriction [Hazlewood et al. (1991)] tandis que l'on explique la diminution de la diffusion dans le milieu extra-cellulaire par les effets de tortuosité [Nicholson and Phillips (1981); Chen and Nicholson (2000)]. L'effet de la diffusion restreinte peut, par exemple, être évalué en changeant le

temps de diffusion [Cooper et al. (1974); Latour et al. (1994)]car les déplacements des molécules sont réduits lorsqu'elles atteignent les limites d'un espace clos. Le coefficient de diffusion décroît alors artificiellement avec l'augmentation du temps de diffusion. De plus, les membranes des cellules cérébrales ont tendance à entraver le processus de diffusion de l'eau (c'est la diffusion 'entravée' par opposition à la diffusion strictement 'restreinte'), et cela même si les membranes sont perméables à l'eau, que ce soit de manière passive ou par le biais de transporteurs comme les canaux spécifiques aquaporines très abondants dans le cerveau [Amiry-Moghaddam and Ottersen (2003)]. Il apparait clairement que la diffusion de l'eau dans les tissus, et particulièrement dans le cerveau, n'est pas libre et ne peut donc pas être modélisée par une simple distribution gaussienne [Cohen and Assaf (2002)]. De plus, l'ADC ne dépend pas uniquement du coefficient de diffusion de la population de molécules d'eau présente en chaque voxel mais également de paramètres techniques expérimentaux tels que la taille du voxel, le temps de diffusion ou le degré de sensibilité à la diffusion de l'image (aussi appelé b-value [Le Bihan et al. (1986)]).

Bien que l'idée de déduire les détails de la microstructure des tissus à partir du signal de l'IRMd seul ne soit réalisable qu'uniquement dans des situations très simples et spécifiques, la relation entre l'ADC et les caractéristiques microscopiques spécifiques du tissu est actuellement l'objet de recherches intensives. Certains groupes ont essayé de clarifier la manière dont les caractéristiques du tissu peut affecter le signal de l'IRMd [Beaulieu (2002); Kroenke and Neil (2004); Schwarcz et al. (2004); Miller et al. (2007); Peled (2007); Wheeler-Kingshott and Cercignani (2009)]. Il a été proposé plusieurs modèles théoriques [Stanisz et al. (1997)] dont un, par exemple, basé sur la combinaison d'un compartiment extra-axonal pour lequel la diffusion serait entravée et d'un compartiment intra-axonal pour lequel la diffusion serait restreinte [Assaf et al. (2004)]. Plusieurs groupes ont également souligné l'importance du rôle de paramètres dynamiques, tels que la perméabilité de la membrane, les échanges aqueux [Kärger et al. (1988); Novikov et al. (1998); Chin et al. (2004)] et les caractéristiques géométriques, tels que la distribution de la taille des cellules ou la distribution des directions axonales/dendritiques [Novikov et al. (1998); van der Weerd et al. (2002); Yablonskiy et al. (2003); Chin et al. (2004)]. Il faut cependant garder à l'esprit que tous ces modèles distincts nécessitent de forts *a priori* sur la structure du tissu qui ne peuvent pas toujours correspondre à une réalité biologique connue ou inconnue.

Simulations Monte Carlo de l'IRM de Diffusion

Pour déduire la relation entre la microstructure des tissus et le signal de l'IRMd, une autre approche consiste à s'appuyer sur des simulations de type Monte-Carlo (MC) qui se sont révélées être un

outil puissant et flexible pour simuler les processus de diffusion dans un vaste panel de systèmes, en particulier lorsque des solutions analytiques ne peuvent être obtenues facilement, en raison de la complexité du système [Lipinski (1990); Ford et al. (1998); Peled (2007); Alexander (2008); Fieremans et al. (2008b); Balls and Frank (2009); Hall and Alexander (2009); Harkins et al. (2009); Imae et al. (2009); Koch and Finsterbusch (2009); Alexander et al. (2010); Budde and Frank (2010); Landman et al. (2010); Nilsson et al. (2010)]. Les approches analytiques qui prédisent le signal de l'IRMd en utilisant l'équation de Bloch-Torrey, par exemple [Barzykin (1998)], doivent s'appuyer sur des modèles de tissus biologiques et une séquence d'impulsions IRM simples (par exemple, un gradient de diffusion avec une forme d'onde rectangulaire). Cependant, dans un cas réaliste, la géométrie des tissus peut être très compliquée, de telle sorte qu'il n'existe pas une description analytique adéquate. Parallèlement, la difficulté pour dériver la solution du signal synthétique de l'IRMd peut augmenter avec la complexité des séquences d'impulsions IRM et les formes du gradient. L'avantage de l'approche MC est sa capacité à suivre les événements dynamiques dans l'espace et le temps. Elle offre des possibilités pour étudier non seulement le mouvement Brownien dans un environnement arbitraire, mais aussi n'importe quel modèle d'interactions entre les spins et les membranes. Ainsi, des données synthétiques d'IRMd générées en utilisant l'approche MC peuvent être appliquées à l'étude des propriétés biologiques (par exemple, la taille des cellules, la densité, la perméabilité des membranes, etc.), ainsi qu'à des mécanismes de diffusion de base dans différents compartiments (par exemple, la présence d'attracteurs, la viscosité locale, les interactions membranaires, etc.). Plus précisément, il peut être adapté à l'examen des hypothèses mécanistiques de divers scénarios dynamiques et modèles de tissus, tels que les attaques vasculaires cérébrales ischémiques aigues ou l'activation neuronale et le gonflement des cellules, le cancer et la prolifération cellulaire, l'ADC et l'anisotropie des fibres axonales dans les faisceaux de fibres complexes ou le cortex [Le Bihan (2003)].

Modélisation des Tissus Biologiques

En principe, l'approche par simulation MC permet de simuler n'importe quel tissu avec beaucoup de détails, pour tenir compte des différents types de processus de diffusion élémentaires et d'en dériver le signal d'IRMd correspondant, à condition que la puissance de calcul nécessaire soit disponible. Comme la géométrie et l'organisation des microstructures biologiques sont extrêmement compliquées au niveau cellulaire (par exemple, la substance grise dans les tissus du CNS), la difficulté se trouve dans la manière de représenter les structures des tissus dans l'environnement de simulation MC. Différents modèles géométriques ont été proposés pour simuler les structures des

tissus dans des conditions physiologiques différentes: Hall et Alexander ont optimisé les paramètres pour la simulation MC de l'IRMd de faisceaux de fibres compactes et en état de gonflement [Hall and Alexander (2009)]. Landman *et al*. ont développé un modèle de l'axone fondé sur des maillages dans le but d'étudier l'impact des fibres axonales endommagées [Landman et al. (2010)]. Budde et Frank ont développé un modèle *beading* des neurites permettant de valider l'importance de la morphologie de la membrane cellulaire sur l'ADC [Budde and Frank (2010)]. Les simulations MC décrites ci-dessus ont utilisé des cylindres pour simuler les faisceaux de fibres de la substance blanche. Cependant, il a été démontré que l'IRMd a une haute sensibilité à la variation de la cytoarchitecture des tissus [Flint et al. (2009)], il est donc également intéressant d'étudier le comportement de la diffusion de l'eau dans le cortex cérébral et les noyaux gris centraux. Lipinski a réalisé la première simulation de MC de la substance grise dans un environnement 2D simplifié composé de géométries de tissus créées à partir des images numériques moyennées de préparations histologiques [Lipinski (1990)]. Il est important de noter que pour des raisons techniques liées à la complexité des calculs, la plupart des simulations MC ont été réalisées en 2D, bien que des simulations 3D seraient plus réalistes pour les systèmes biologiques. Balles *et al*. ont développé un système de simulation 3D efficace qui a la capacité d'effectuer des simulations à grande échelle de la diffusion de l'eau dans des microstructures et une physiologie tissulaire complexes, mais cela uniquement pour simuler des séquences PGSE d'IRMd conventionnelles [Balls and Frank (2009)].

L'Objectif

Cette thèse se consacre au développement et à l'application d'un simulateur de Monte-Carlo (MC) de l'IRMd intégré et généralisé, 'Diffusion Microscopist Simulator' (DMS), et vise à (i) combler l'écart entre les processus de diffusion élémentaires qui se produisent à une échelle *micrométrique* et le signal de diffusion résultant mesuré à l'échelle *millimétrique*, en offrant un meilleur aperçu des caractéristiques observées dans l'IRMd (par exemple, la variation de l'ADC et de l'anisotropie de diffusion avec la distribution des tailles des cellules), et (ii) offrir des informations vérité terrain pour l'optimisation et la validation des séquences d'acquisition de l'IRMd pour différentes applications (par exemple les techniques de tractographie, la modélisation biophysique locale du processus de diffusion, et la microscopique par IRM de diffusion).

Alors que le développement d'un nouveau logiciel de simulation serait une tâche énorme, une question générale se pose naturellement - pourquoi ne pas travailler simplement sur un logiciel de simulation existant? Ce qui suit est un résumé global de mon point de vue sur cette question:

Le premier problème à souligner est que la simulation MC de l'IRMd est une technique large-

ment répandue, adoptée par des scientifiques de domaines très différents (par exemple les physiciens de l'IRM, les biophysiciens, les biochimistes, les biologistes, etc.). Les spécificités propres à chaque domaine d'application se retrouvent fortement au niveau des codes de calcul, et peuvent malheureusement restreindre un code à l'application pour laquelle il avait été développé, ce qui rend souvent compliqué l'adaptation d'un code existant pour d'autres études que celles prévues à l'origine. Par conséquent, il nous a semblé intéressant de développer un cadre de simulation générique qui puisse être utilisé quel que soit le domaine d'application. Pour remplir cet objectif, le simulateur doit être facilement adaptable aux besoins spécifiques des utilisateurs. La réalisation d'une telle plateforme de simulation MC de l'IRMd fut l'un des principaux objectifs de cette thèse. Il doit être également rapide pour ne pas affecter la productivité des scientifiques. Atteindre des calculs de haute performance implique un soin particulier au niveau des codes qui doivent être optimisés et parallélisé pour s'exécuter sur une grille de calcul qui permette d'atteindre les performances requises. Enfin, l'ergonomie du simulateur doit être pensée et le pipeline de simulation doit être tel que tout utilisateur puisse très rapidement en comprendre son utilisation et s'approprier l'outil pour ses propres besoins. Les points évoqués ci-dessus ont très largement motivé cette thèse et conduit au développement d'un nouvel outil de simulation du processus de diffusion, appelé DMS (pour Diffusion Microscopist Simulator), dédié à l'étude et à la compréhension des mécanismes d'encodage du phénomène biophysique sur le signal d'IRMd.

Organisation de cette thèse

Cette thèse est organisée en quatre parties et sept chapitres. La partie *Introduction* (chapitre 2) décrit les principes fondamentaux de l'IRM de diffusion (IRMd) et les techniques modernes d'IRMd. Puis, la partie *Méthodes* (chapitres 3 et 4) développe la structure du simulateur DMS, contribution méthodologique majeure de la thèse. Enfin, la partie *Applications* (chapitres 5 et 6) présente les apports du simulateur dans le cadre d'applications spécifiques en IRMd. Le contenu et les contributions de chaque chapitre sont décrits de manière plus détaillée ci-dessous:

Part I. INTRODUCTION

Chapter 2: RMN et IRM de diffusion. Le chapitre 2 commence par un résumé de l'histoire de la résonance magnétique nucléaire (RMN) en mettant l'accent sur l'IRM de diffusion, puis se poursuit par les principes de base qui fondent la physique de l'IRMd nécessaires à la compréhension de cette thèse. Ensuite, ce chapitre offre un résumé des méthodologies existantes en IRMd et introduit les dernières avancées méthodologiques de l'IRMd qui permettent désormais de sonder la microstructure des tissus cérébraux et d'en mesurer les caractéristiques.

Enfin, le chapitre 2 introduit l'IRM de diffusion fonctionnelle (IRMdf) qui repose sur l'observation des modifications structurelles intervenant au cours de l'activité cérébrale et qui permettrait de détecter plus précocément cette activité que ne le permet l'imagerie BOLD conventionnelle.

Part II. METHODES

Chapter 3: Simulateur du processus de diffusion "Microscopist" Le chapitre 3 décrit de manière détaillée l'élaboration et le développement méthodologique du *Diffusion Microscopist Simulator* (DMS), outil intégré et générique dédié aux simulations Monte-Carlo du processus de diffusion et à la compréhension de l'IRMd. Le simulateur DMS est doté de deux composants: un *Simulateur Monte-Carlo* et un *Synthétiseur de données d'IRM*. Le premier composant est capable de générer des modèles de tissus tridimensionnels dotés de formes et de propriétés variées, tandis que le deuxième composant permet de synthétiser les signaux d'IRM de diffusion qui seraient obtenus à partir des modèles géométriques précédents pour un large panel de méthodes d'imagerie de diffusion, de types de séquence et de paramètres de séquence. Le chapitre expose la conception détaillée de l'outil et le rôle de ses divers composants, ainsi que les méthodes mises en oeuvre pour obtenir un code efficace en termes computationnels dans la perspective de simulations d'IRMd à grande échelle. Un organigramme d'utilisation type est présenté pour illustrer la préparation et l'exécution d'une simulation par l'outil DMS. Ce chapitre se conclut par une discussion sur les avantages et inconvénients du simulateur. La Fig. 1 illustre l'architecture et l'interface graphique du DMS proposée à l'utilisateur.

Chapter 4: Expériences fondamentales. Avant d'appliquer le DMS à l'étude de thèmes de recherche spécifiques, le chapitre 4 présente certaines expériences de simulation basiques d'IRMd afin de tester la robustesse et la performance du DMS. Quatre différents types d'expériences ont été menés comme suit: (i) *Multiple scattering diffusion imaging* (MSDI). Pour des valeurs de q ou b suffisamment élevées, la taille et la forme des compartiments se traduisent par la présence de pics de diffraction lorsque le signal de diffusion est mesuré en fonction du temps de diffusion à l'aide d'une séquence de type *Pulse Gradient Spin Echo* (PGSE) (Fig. 2a). Nous avons utilisé le DMS pour simuler le processus de diffusion de tissus virtuels doté des paramètres structurels prédéfinis (diamètres des cylindres), puis nous avons synthétisé le signal d'IRMd correspondant au cas d'utilisation de séquences PGSE simple et double afin d'estimer en aveugle les paramètres des tissus dont la valeur a été fixée précédemment. (ii) *Spectroscopie de diffusion temporelle.* Les méthodes d'*Oscillating Gradient Spin Echo* (OGSE) permettent d'explorer le processus de diffusion de l'eau à des échelles de temps de diffusion variées. A

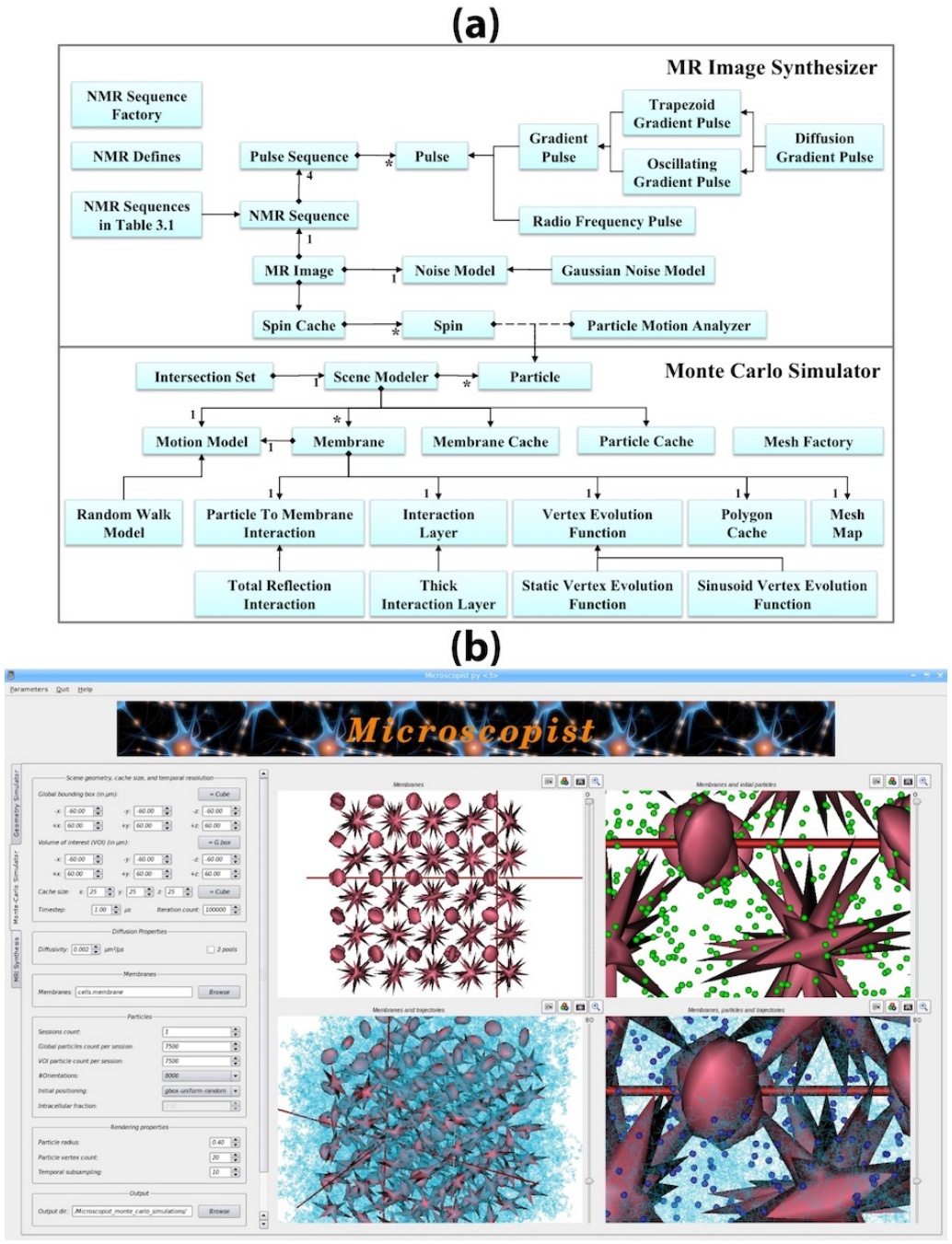

Figure 1: "Diffusion Microscopist Simulator". - (a) Le diagramme complet de modélisation (b) Ergonomie de l'interface graphique.

haute fréquence, l'appoche OGSE devient sensible à des mouvements de très faible amplitude, à l'instar des déplacements s'opérant au sein des structures intracellulaires. Dans cette expérience, le DMS a été utilisé pour étudier la dépendance de l'attenuation du signal pondéré en diffusion en fonction de la forme des oscillations et de leur fréquence. (iii) *Modèle tissulaire.* Le gonflement cellulaire a été proposé comme facteur principalement responsable de la chute

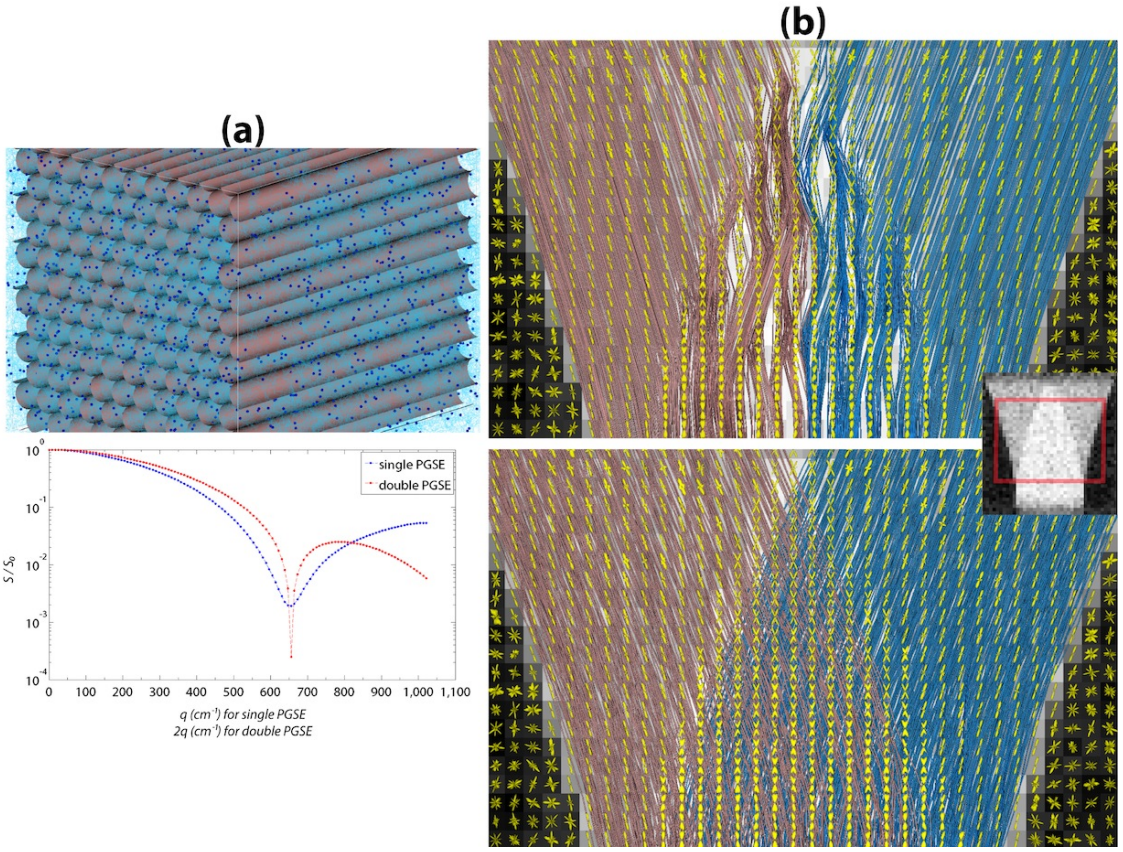

Figure 2: Expériences fondamentales menées avec le simulateur DMS. - (a) Expérience révélant le phénomène de diffusion-diffraction à travers l'utilisation de séquence PGSE et dPGSE. (b) Simulation d'embranchements de fibres faite avec le DMS servant de référence à l'évaluation des algorithmes de tractographie streamline déterministe (haut) et probabiliste (bas).

de l'ADC pour les accidents vasculaires cérébraux. Au cours de l'activation neuronale, il se pourrait que les variations d'ADC résultent d'une combinaison entre effets du gonflement cellulaire et modification de la perméabilité membranaire. Des simulations avec le DMS ont été menées pour investiguer les variations de l'ADC en fonction de la taille des cellules et de leur perméabilité. (iv) *Modèles de diffusion locaux et applications au suivi (tracking) de fibres.* Nous avons utilisé le DMS pour créer des faisceaux virtuels de fibres de la substance blanche présentant des configurations complexes comportant des croisements, des embranchements et des configurations de fibres en éventail. Les données synthétiques d'IRMd correspondant à ces diverses configurations ont été générées pour différentes valeurs de rapport signal à bruit (SNR), et nous avons démontré que ces jeux de données synthétiques se révèlent très utiles pour évaluer les performances des algorithmes de reconstruction de diffusion et de tracking de fibres (Fig. 2b).

Part III. APPLICATIONS

Chapitre 5: Impact d'une impulsion de gradient de diffusion finie sur l'estimation de l'orientation de fibres. Le chapitre 5 décrit la première seconde contribution majeure de cette thèse et utilise à la fois le simulateur DMS poyr y répondre ainsi qu'un fantôme de diffusion physique pour corroborer les résultats - l'impulsion de gradient très brève étant un prérequis dans la théorie de l'espace q, *Quel est l'impact d'une impulsion de gradient de diffusion de durée finie sur les modèles locaux de diffusion utilisés pour la cartographie des orientations des fibres nerveuses en IRM de diffusion*?

L'estimation précise des orientations des fibres nerveuses en chaque voxel est une étape essentielle de la tractographie et un grand nombre de méthodes ont été proposées pour reconstruire la fonction de distribution d'orientation à partir de l'échantillonnage en 3 dimensions de l'espace q. Dans le formalisme de l'espace q, de très courtes impulsions de gradient (infinitésimales) sont nécessaires pour reconstruire la véritable fonction de densité de probabilité (PDF) des déplacements des spins. Cependant, sur les systèmes d'imagerie par résonance magnétique cliniques actuels, la durée de l'impulsion (δ) est inévitablement finie du fait des limitations de l'intensité des gradients atteignables. L'impossibilité de satisfaire la condition d'impulsion de gradient courte (SGP) a souvent été source de critiques de l'approche basée sur l'espace q pour l'estimation des fonctions d'orientation des fibres. Cependant, l'effet d'un long δ sur le signal d'IRMd et sur la précision angulaire de l'orientation estimée n'a pas encore été pleinement caractérisé.

Sous l'approximation SGP, le codage en phase des spins est supposé se faire instantanément. Le déplacement mesuré dans l'espace q correspond alors à la distance entre la position initiale du spin lors de la première impulsion de gradient de diffusion et sa position finale au moment de la seconde impulsion (Fig. 3(a) - gauche). Cependant, avec une durée d'impulsion δ finie, la particule est marquée avec une position donnée par le centre de masse de son trajet durant l'application de l'impulsion de gradient [Mitra and Halperin (1995)]. Ainsi, le déplacement effectif réellement estimé correspond à la distance entre la position moyenne du spin pendant la première impulsion de diffusion et sa position moyenne pendant la seconde impulsion (Fig. 3(a) - droite). Pour des géométries restreintes, la position moyenne du spin pendant chaque impulsion va avoir tendance à converger vers le centroïde du compartiment restreint (Fig. 3(a) - droite). Le déplacement estimé décroit donc lorsque δ augmente, et par conséquent l'atténuation du signal d'IRMd mesuré est réduite. A l'échelle de temps d'une expérience d'IRMd, la diffusion dans les fibres myélinisées de la substance blanche peut être approximée

comme restreinte dans les directions perpendiculaires à l'axe de la fibre (i.e. la direction radiale), et libre le long de l'axe de la fibre (i.e. la direction axiale) [Assaf et al. (2004); Assaf and Basser (2005)]. Dans ce cas, l'augmentation de δ devrait mener à une atténuation réduite du signal de diffusion radial, sans changement dans le signal de diffusion axial. Ceci devrait donc améliorer le contraste entre les directions des gradients de diffusion, et aussi augmenter le rapport signal sur bruit pour toutes les images de diffusion, ces deux aspects étant utiles pour estimer les orientations des fibres.

Dans ce chapitre, l'influence de la largeur finie des gradients de diffusion δ sur le signal d'IRMd mesuré comme fonction de la direction du gradient est décrite théoriquement et démontrée à l'aide de simulations faites à partir du simulateur DMS, mais également à partir de fantômes matériels de diffusion expérimentaux, et un modèle de tissu biologique. Les résultats suggèrent que la pratique habituelle, due aux limitations de la machine, d'utiliser une longue durée δ pour l'imagerie de diffusion sur les scanners IRM humains cliniques, pourrait être en fait bénéfique dans l'estimation des orientations de fibres. Nous concluons donc que pour une b-valeur donnée, l'allongement de δ est avantageux pour estimer les orientations de fibres pour deux raisons : premièrement, cela conduit à une augmentation du signal de diffusion dans le plan transverse à la fibre; deuxièmement, cela allonge la forme du profil de diffusion mesuré, ce qui améliore le contraste du signal pour les différentes orientations de diffusion. Ce contraste étant essentiel pour discriminer différentes directions de fibres, ceci est spécialement bénéfique pour la détection des croisements de fibres. (Figs. 3(b)&(c)).

Chapter 6: Évaluation de la cartographie des rayons des fibres en utilisant l'IRM de diffusion clinique. Le chapitre 6 concerne l'étude de la deuxième application du Simulateur de Diffusion Microscopist (DMS) et se penche sur cette question en termes de microscopie par IRM de diffusion - *Est t'il possible d'estimer le calibre des fibres en utilisant un système d'IRM clinique*?

Les méthodes émergentes en microscopie par IRMd commencent à fournir des informations quantitatives sur la taille des cellules, à l'échelle microscopique; ces nouvelles techniques ont d'abord vu le jour sur des systèmes IRM précliniques (méthodes 'AxCaliber' [Assaf et al. (2004, 2008)] et QSI [Callaghan (1993); Cory and Garroway (1990)]) parce que nécessitant de puissants gradients pour satisfaire l'exigence stricte d'une impulsion de gradient étroite, et se sont focalisées sur la matière blanche parce que les faisceaux de fibres présentent une géomtrie cylindrique reposant sur peu de paramètres et s'avérait donc facile à modéliser. Il en est de même s'agissant des techniques reposant sur les séquences de type OGSE [Stepisnik

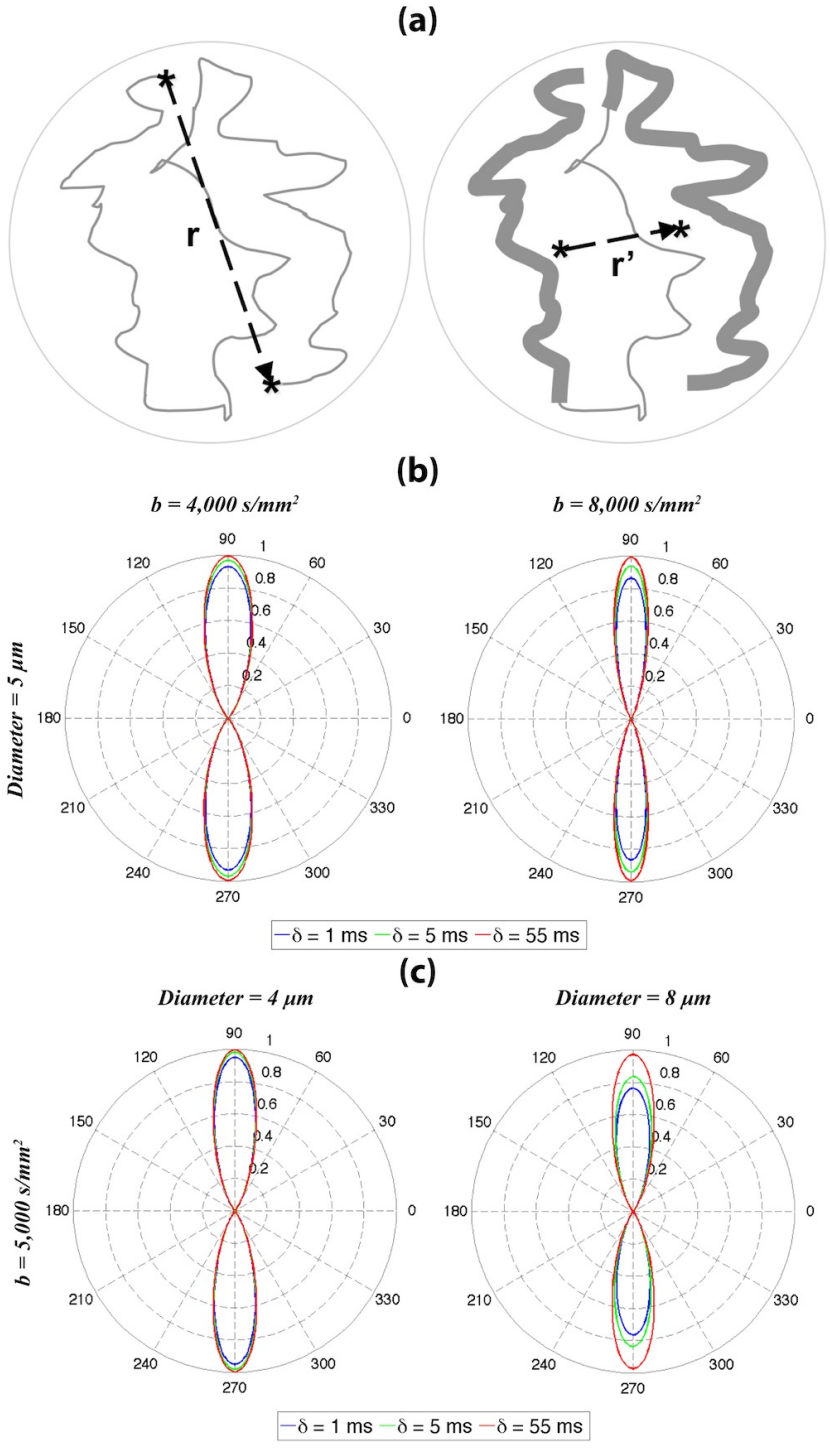

Figure 3: Dépendance du signal d'IRMd à la durée d'impulsion de gradient de diffusion. - (a) Nous suggérons que le déplacement moyen de diffusion de l'eau dans un environnement restreint va décroitre lorsqu'on utilise une durée d'impulsion longue (gauche: δ court; droite: δ long). (b) Représentation polaire du signal d'IRMd montrant l'effet de δ et sa dépendance à la b valeur. (c) Représentation polaire du signal d'IRMd montrant l'effet de δ et sa dépendance vis-à-vis de la taille de la géométrie.

(1993); Xu et al. (2009a,b)] nécessitant quant à elle un gradient puissant pour augmenter la sensibilité et la résolution des measures en IRMd. A cause de ces conditions de sécurité et de ces limites matérielles, un système à fort gradient ne peut pas être installé sur une IRM clinique. Quant à la méthode MSDI [Ozarslan and Basser (2008); Ozarslan et al. (2009); Ozarslan (2009); Shemesh and Cohen (2008); Shemesh et al. (2009a,b, 2010a,b)], bien qu'elle ait la possibilité de fournir des informations microscopiques à travers une séquence double PGSE avec des gradients de plus faible puissance, cette méthode reste encore cantonnée au stade de descriptions théoriques, de simulations, et d'études expérimentales sur des systèmes d'IRM précliniques. De plus, l'approche MSDI basée sur une séquence de type double PGSE repose sur la connaissance a priori de l'orientation des fibres, ce qui reste possible s'agissant de très gros faisceaux tels que le corps calleux dont l'orientation est facilement détectable, mais devient beaucoup plus difficile s'agissant par exemple de la connectivité sous corticale encore peu connue et peu décrite dans la littérature. Une alternative à la méthode MSDI utilise une séquence dotée d'un champ de gradients bipolaires à double impulsion, permettant d'obtenir une estimation précise de la géométrie des pores (espaces intra et extra cellulaires) au sein desquels s'opère le processus de diffusion [Shemesh et al. (2010a)]. Cependant, cette séquence à multiple impulsions augmente considérablement le nombre de mesures requises pour compenser le faible rapport signal sur bruit dû à un temps d'écho très long. Ainsi, elle n'est pas applicable dans le cadre d'une application clinique où le temps d'acquisition joue un rôle important. De plus, les séquences à impulsion MSDI ne sont pas disponibles sur les scanners IRM actuels car leurs versions logicielles ne sont pas encore commercialisées.

Plus récemment, Daniel Alexander a développé un cadre mathématique permettant d'optimiser les paramètres d'acquisition d'une séquence PGSE standard et qui permet d'estimer in vivo le diamètre et la densité des fibres sans connaissances préalables sur l'orientation de celles-ci [Alexander (2008); Alexander et al. (2010)]. Bien que cette méthode soit capable de créer de façon efficace un protocole d'imagerie de diffusion afin de mesurer la taille des cellules ou encore le rayon des fibres du cerveau humain, des difficultés persistent quant à son utilisation pour des examens cliniques pour deux raisons. Premièrement, la stratégie d'optimisation est limitée à un rayon de fibre spécifique, alors que la substance blanche du cerveau humain comporte un large éventail de fibres différentes avec des rayons allant de 1 à 10 μm; deuxièmement, une forte valeur d'intensité de gradient (au minimuim 70 mT/m) est indispensable pour garantir une estimation précise des fibres ayant un petit rayon alors que d'un autre côté les scanners IRM cliniques ne sont équipés qu'avec des systèmes de gradient standard dôtés

d'une amplitude maximale de 40 mT/m.

Ce chapitre, basé sur des simulations réalisées à partir de l'outil DMS, a pour but à la fois d'analyser la faisabilité d'une cartographie des rayons de fibres de la substance blanche en utilisant des scanners IRM cliniques standards, et également de déterminer l'influence des paramètres de la séquence de diffusion sur l'estimation du rayon de ces fibres. Nous avons utilisé le simulateur DMS afin de réaliser des simulations de parcours aléatoires (méthode de Monte-Carlo) issues de la diffusion des molécules d'eau dans un environnement doté de fibres de différents rayons (Fig. 4(a)), et nous avons généré des données synthétiques de diffusion en utilisant un jeu de protocoles PGSE standard connu pour être comparable aux capacités des systèmes de gradient présents en clinique. (Fig. 4(b)). Les rayons des fibres sont estimés grâce à la méthode MCMC (Markov Chain Monte Carlo) dont l'algorithme réalise un échantillonnage optimal de la distribution des paramètres du modèle (Fig. 4(c)). Les simulations laissent à penser que le facteur de pondération en diffusion (c'est-à-dire dans notre cas la b-value) et la sélection de l'échantillonnage dans l'espace q ont une influence importante dans la cartographie des rayons des fibres. Nos résultats fournissent une règle générale permettant de paramètrer les protocoles cliniques afin d'obtenir des informations sur la microstructure du cerveau. Pour un temps d'acquisition acceptable de 30 minutes, nous pouvons conlure que l'utilisation de trois ou quatre sphères échantillonnées dans l'espace q avec des valeurs de b-value modérées à hautes rend tout à fait possible l'identification des rayons des fibres supérieurs à 2 μm.

Part IV. CONCLUSION

Chapter 7: Synthèse et conclusion. Le chapitre résume les résultats présentés dans cette thèse et énumère les objectifs atteints. Les contributions apportées sont à nouveau listées et enfin des recommandations et des futures directions sont examinées.

Contributions

La principale contribution méthodologique de cette thèse est le développement d'un outil générique et puissant de simulation de Monte-Carlo du processus de diffusion dans le tissu cérébral: 'Diffusion Microscopist Simulator' (DMS) qui a la capacité d'une part de créer des modèles de tissus biologiques tridimensionnels de formes et propiétés différentes, et aussi de synthétiser des données d'IRM de diffusion issues d'un large éventail de méthodes en IRM et de design de séquences paramètrables. le simulateur DMS a pour but de combler le fossé entre les processus de diffusion élémentaires qui apparaissent à une échelle micrométrique et le résultat du signal de diffusion mesuré à une échelle

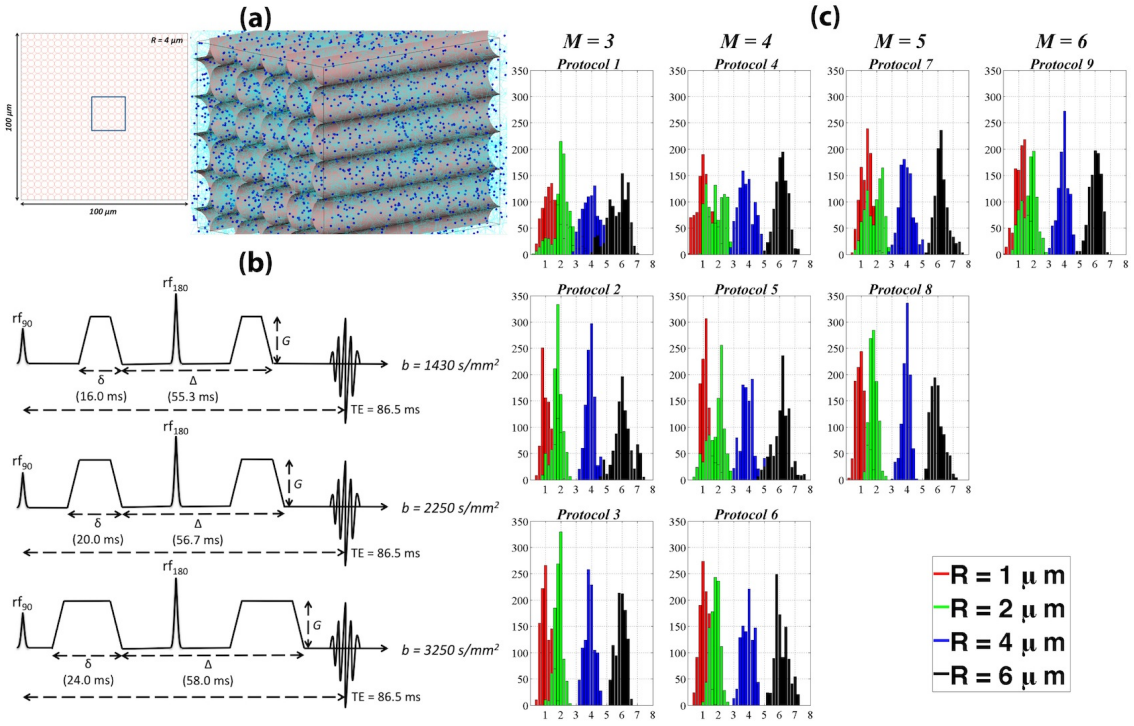

Figure 4: Estimation des rayons de fibres à partir de données cliniques d'IRM de diffusion. - (a) Simulation Monte-Carlo conduite à l'aide du simulateur DMS. (b) Séquences de gradient spin echo (PGSE) conçues pour les synthèses d'IRMd. (c) Les rayons des fibres ont été estimés grâce à la méthode Markov-Chain Monte-Carlo qui échantillonne la distribution des paramètres du modèle.

millimètrique, donnant ainsi un meilleur aperçu des caractéristiques observées en IRMd, tout en offrant une réelle information pratique utilisable pour l'optimisation et la validation de protocoles d'IRMd pour de nombreuses applications.

Nous avons vérifié la performance et la validité du simulateur DMS à travers de nombreux tests et expérimentations, et nous l'avons aussi utilisé dans des cas concrets de recherche en IRM de diffusion. Deux contributions majeures ont été réalisées dans cette thèse à partir du simulateur DMS. La première a consisté à l'investigation de l'impacte d'un gradient de diffusion de durée définie (δ) sur l'estimation de l'orientation des fibres en IRMd. Nous pensons que l'utilisation actuelle d'un long δ, qui est renforcé par la limitation matérielle sur les scanners cliniques, est actuellement bénéfique pour la cartographie des orientations des fibres, bien que cela contredise l'hypothèse sous-jacente faîte par la théorie de l'espace q. La deuxième contribution concerne l'utilisation du simulateur afin d'analyser la faisabilité de l'estimation du rayon des axones dans le cadre d'IRM clinique. Les résultats suggèrent que l'algorithme qui cartographie les microstructures directes est tout à fait applicable aux données issues d'IRM cliniques standards.

Ainsi, l'extension des simulations par ordinateur à des expérimentations réelles sur scanner a été

le but des développeurs logiciels dans la communauté qui attendaient une situation où l'interaction entre les expérimentations et les simulations pouvait se réaliser en IRMd. Nous espérons que le simulateur DMS s'avérera un outil puissant et utile à la compréhension des relations qui existent entre les mécanismes de bases de l'IRMd aux niveaux des tissus du cerveau et également que cet outil permettra d'améliorer de façon sensible la méthodologie des futures applications en IRM de diffusion.

Part I

INTRODUCTION

Chapter 1

Introduction

Contents

1.1 Preface

Water appears stationary to the naked eye of human beings, whereas at a microscopic scale water molecules are in a status of dynamic fluctuations. Such random translational motion of molecules is a phenomenon termed Brownian motion, which was observed in 1827 by the well-known botanist, Robert Brown, from the jiggling pollen granules suspended in water [Brown (1828)]. It was not until 1905 that Albert Einstein revisited this phenomenon and published a theoretical analysis of Brownian motion, it became clear that molecular diffusion in liquid or gas results from the thermal energy carried by the molecules [Einstein (1905)].

Imagine for an instant if we could give a label to a water molecule in a brain tissue and keep track of its diffusion-driven movement, we would find that the path is shaped by the tissue microstructures of the brain. This establishes the basic idea of diffusion magnetic resonance imaging (dMRI) that utilizes the microscopic natural displacements of water molecules that occur in brain tissues as part of physical diffusion process to produce the MRI-based quantitative maps. In dMRI, water molecules are thus utilized as a an endogenous tracer that can non-invasively reveal microscopic details about tissue architecture, either normal or in a diseased state.

Diffusion MRI came into existence in the mid-1980s [Le Bihan et al. (1986); Wesbey et al. (1984a,b)], and during the last 25 years, dMRI has been extraordinarily successful, particularly in MRI of the central nervous system (CNS). Its major clinical domain of application has been neurological disorders, especially for the management of patients with acute ischemic stroke. It is also rapidly becoming a standard for white matter (WM) disorders, as diffusion tensor imaging (DTI) can reveal abnormalities in WM fiber structure and provide outstanding maps of brain connectivity [Basser et al. (1994a,b); Conturo et al. (1999); Mori et al. (1999); Basser et al. (2000); Poupon et al. (2000)]. The ability to visualize anatomical connections between different parts of the brain, non-invasively and on an individual basis, has emerged as a major breakthrough for neurosciences. More recently, it has been shown that dMRI could also be used to deliver direct features of tissue microstructures [Alexander (2008); Assaf et al. (2008)], as well as to detect changes in brain tissue structure associated with neuronal activation [Le Bihan et al. (2006)].

1.2 Motivation

Molecular diffusion is a multi-scale integrated process by which fluctuations in molecular random motion at a microscopic scale can be inferred from observations at a larger scale using statistical physical models, even though the individual molecular structure and pathway are fully ignored [Le Bihan (2007)]. Owing to the microscopic length scale of diffusion in biological

tissues, dMRI is an exquisitely sensitive tool to reveal tissue architecture unrecognizable through the conventional MRI methods. However, it is important to keep in mind that the driving force of dMRI is to monitor the diffusion-driven displacements of water molecules at a microscopic level that is well beyond the usual MRI resolution. In other words, the overall signal observed in dMRI images at a millimetric resolution, results from the integration, on a statistical basis, of all the microscopic displacement distributions of the water molecules present in this voxel. In consequence, the complex diffusion processes that occur in a biological tissue on a voxel scale are often described with a global, statistical parameter, the 'apparent diffusion coefficient' (ADC) [Le Bihan et al. (1986)]. This parameterization of the diffusion process by a global ADC is intended to represent those physical processes that occur at scales smaller than the scales resolved by the method: the large scale is imposed by technical limitations (e.g., hardware), while the actual scale of the biophysical elementary processes is determined by physical phenomena at molecular scale. The averaging and smoothing effect resulting from this scaling presumes some homogeneity in the voxel and makes a direct physical interpretation out of the global parameter somewhat difficult, unless some assumptions can be made.

This thesis dedicates to the development and application of an integrated and generalized dMRI Monte Carlo (MC) simulation system, 'Diffusion Microscopist Simulator' (DMS), and aims at (i) bridging the gap between elementary diffusion processes occurring at a micrometer scale and the resulting diffusion signal measured at millimeter scale, providing better insights into the features observed in dMRI (e.g. variation of ADC and diffusion anisotropy with cell size distribution); and (ii) offering ground-truth information for optimization and validation of dMRI acquisition schemes for different applications (e.g. fibre-tracking algorithm, diffusion local modeling, and diffusion microscopy imaging).

While managing a new simulation software is an enormous task, a general question naturally arises - why not straightforwardly work on an existing simulation program? The following is a global summary of my viewpoint to this question:

The first issue to note is that dMRI MC simulation is a widespread technique adopted by scientists of diverging fields (e.g. MR physicists, biophysicists, biochemists, biologists, etc.). Usually, the differing concerns and techniques of scientists are reflected in their code bases which are tailored to specific methods and problems in origin. For now, it is sufficient to mention that the bias of some individual codes means it will be complicated to extend them with new algorithms for other studies. Hence, it is evidence that it would be certainly beneficial to have a generic simulation system for all scientists to use. To accomplish this purpose, it requires a platform that allows the scientists in different fields to customize for certain research topics. Furthermore, importantly, the

new platform should enables the software developers to rapidly implement the new algorithms for extensions. The realization of such a dMRI MC simulation platform is one of the major goals of this thesis. Secondly, computation efficiency is required as it may affect the productivity of the scientists who need to use the software. Reaching high performance computing involves the procedure of codes profiling, optimization, and parallelization of the platform. Thirdly, practical factors like workflow and data management need to be optimized to prevent scientists not only from running replicated calculations but also from wasting an inordinate amount of efforts on tasks like organizing data. And last, the command-line of the program is required to be clear and simple for scientists to understand. Mysterious commands may actively discourage the scientists their uses as well as restrict a powerful tool to a narrow subset of the community. In my opinion, the reasons above has already substantially motivated this thesis to create a novel framework for dMRI simulations.

1.3 Outline

The thesis is organized in four parts and seven chapters. The Introduction part (Chapter 2) describes the basic principles of dMRI and modern dMRI techniques. Then, the Methods part (Chapter 3 & 4) describes the framework of DMS, the major methodological contribution of the thesis. Finally, the Application part (Chapter 5 & 6) describes the contributions of DMS for specific dMRI applications. An overview of the contents and contributions in each chapter is described as follows:

Part I. INTRODUCTION

Chapter 2: Diffusion NMR and MRI. Chapter 2 begins with the reviews of the history and evolution of diffusion NMR and MRI, followed by the background and basic principles of dMRI physics needed to understand thesis. Then, this chapter gives a summary of current dMRI methodologies and an introduction to the modern dMRI techniques aiming at imaging microstructural features of brain tissues. Finally, the chapter introduces the hypothesis of mapping neuronal activation using diffusion functional MRI (dfMRI).

Part II. METHODS

Chapter 3: Diffusion Microscopist Simulator. Chapter 3 describe the detail framework design and the methodological development of *Diffusion Microscopist Simulator* (DMS), which has been put efforts to make it an integrated and generic tool for dMRI MC simulations. DMS is composed of a *Monte Carlo Simulator* and a *MR Image Synthesizer*. The former is

able to generate 3D tissue models of various shapes and properties, while the latter is able to synthesize diffusion MRI signals for a large variety of MRI methods, pulse sequence design and parameters. The chapter describes the concept and function for the key components of DMS, as well as the methods to achieve high computing efficiency for large-scale dMRI simulations. After that, the working diagram is depicted to illustrate how to prepare and execute a DMS simulation. The chapter ends with a discussion regarding to the pros and cons of DMS framework.

Chapter 4: Benchmark Experiments. Before applying DMS to study specific research topics, Chapter 4 demonstrates the basic dMRI simulation experiments in order to examine the performance and validity of DMS. Five different kinds of experiments were performed as follows: (i) *Multiple scattering diffusion imaging.* At sufficiently high q- or b-values, the size and shape of tissue compartments will be reflected by the diffraction peaks in diffusion signal decay obtained from the pulsed gradient spin echo (PGSE) experiments. We employed DMS to run MC simulations in virtual tissues with predefined structural parameters, and then generated synthetic diffusion signal decay based on a simulated single- and double-PGSE pulse sequences to estimate the ground-truth tissue parameters. (ii) *Temporal diffusion spectroscopy.* The oscillating gradient spin echo (OGSE) methods have the capacity to probe the water diffusion over various time scales. At high frequencies, for instance, the OGSE approach has the potential to detect changes over much smaller lengths, such as the intracellular structures. In this experiment, DMS was utilized to investigate the dependency of diffusion signal decay using OGSE sequences with different oscillating waveforms and frequencies. (iii) *Tissue characteristics and models.* Cell swelling has been proposed to be a major factor responsible for the drop of ADC in acute ischemic stroke. During neuronal activation, it has been proposed that the variation of ADC rather results from the integrated effect of cell swelling and cell membrane properties. DMS simulations were performed to investigate the variations of ADC induced by cell sizes and membrane characteristics in this section. (iv) *Diffusion reconstruction model.* We showed that DMS can be utilized to assess the performance of diffusion models for the purpose of fibre orientation mapping. We analyzed the synthetic dMRI data of crossing fibres that were generated via different fibre distributions (e.g. 90 and 60-degree crossing fibres) and pulse sequence parameters (e.g. b-value and signal-to-noise ratio (SNR)). (v) *Fibre-tracking application.* We used DMS to create 3D virtual WM fibre bundles with complex configurations including crossing, kissing, and branching fibres, which were served as ground-truth information for evaluating the validity of fibre tractography.

The experiments (iv) and (v) demonstrated that these synthetic datasets were practical for assessing the performance of diffusion reconstruction and fibre-tracking algorithms.

Part III. APPLICATIONS

Chapter 5: The Effect of Finite Diffusion Gradient Pulse on Fibre Orientation Estimation. Chapter 5 describes the first particular application of DMS to address an important question - as the narrow pulse is a prerequisite in q-space theory, what is the impact of finite diffusion gradient pulse duration on local diffusion models aiming at mapping neural fibre orientations in dMRI?

An essential step for fibre-tracking is the accurate estimation of neuronal fibre orientations within each imaging voxel, and a number of methods have been proposed to reconstruct the orientation distribution function based on sampling 3D q-space. In the q-space formalism, very short (infinitesimal) gradient pulses are the basic requirement to reconstruct the true probability density function (PDF) of spin displacements. On current clinical MR systems, however, the diffusion gradient pulse duration (δ) is inevitably finite due to the limit on the achievable gradient intensity. The failure to satisfy the short gradient pulse (SGP) requirement has been a recurrent criticism for fibre orientation estimation based on the q-space approach.

In this chapter, the influence of a finite δ on the dMRI signal measured as a function of gradient direction is described theoretically and demonstrated through DMS simulations, experimental diffusion phantoms, and a biological tissue model. The results suggest that the current practice of using long δ for DW imaging on human clinical MRI scanners, which is enforced by hardware limitations, might in fact be beneficial for estimating fibre orientations. For a given b-value, the prolongation of δ is advantageous for estimating fibre orientations for two reasons: First, it leads to a boost in DW signal in the transverse plane of the fibre. Second, it stretches out the shape of the measured diffusion profile, which improves the contrast between DW orientations. This is especially beneficial for resolving crossing fibres, as this contrast is essential to discriminate between different fibre directions.

Chapter 6: Evaluation of Fibre Radius Mapping Using Clinical Diffusion MRI. Chapter 6 is the second application study of DMS to look into the question in terms of microscopic dMRI - is it possible to estimate the fibre calibers using clinical dMRI?

This chapter, based on DMS simulations, aims to assess the feasibility of mapping WM fibre radii using the clinical MR scanners, as well as to investigate the influence of DW pulse se-

quence parameters on the fibre radius estimation. We used DMS to perform random walk MC simulations of water diffusion in virtual WM fibres with various radii, and generate synthetic dMRI data using a set of conventional PGSE imaging protocols devised to be compatible with the capabilities of the standard clinical gradient system. Fibre radii are estimated via the procedure of Markov Chain Monte Carlo (MCMC) algorithm that samples the posterior distribution of model parameters. Simulations suggest that the diffusion-sensitizing factor (i.e. b-value) and the selection of the q-space sampling shell are important for fibre radius mapping. Our results provide a general rule to set up clinical protocols for the purpose of delivering microstructural information. Within a clinical acceptable acquisition time of 30 minutes, we conclude that using three to four q-space sampling shells with moderate to high b-values is potentially feasible to identify fibre radii greater than 2 μm.

Part IV. CONCLUSION

Chapter 7: Summary and Conclusion. The chapter delineates the final summary of the results presented in this thesis and the objective achieved. The original contributions of this thesis are reiterated, and recommendations for future directions are discussed.

1.4 Original Contributions

The most significant original contribution of this thesis are (i) the development of *Diffusion Microscopist Simulator*, a novel dMRI MC simulation framework (Chapter 3); and (ii) the demonstration (Chapter 4) and application (Chapter 5 & 6) that DMS has the potential to address a wide class of issues in dMRI. Indeed the expanding of computer simulations to MR experimentalists has been a goal of software developers in the community who have expected a situation where the interplay between experiments and simulations will be an integral part of dMRI. I hope that DMS will be considered as a reliable tool that help to advance the knowledge on the relationship between the underpinning diffusion mechanism and dMRI in brain tissues, as well as to substantially improve the dMRI methodology for further applications.

Chapter 2

Diffusion NMR and MRI

Contents

2.1 Timeline of Diffusion MRI History

This section introduces a brief summary of the important events associated with the evolution of dMRI.

1828 - Robert Brown, the Scottish botanist, is regarded as the first person who discovered that the pollen grains suspended in water exhibited a rapid jitter motion under a microscope [Brown (1828)].

1855 - Adolf Fick introduced the famous Fick's law of molecular diffusion, which describes the relationship between the diffusive flux and the concentration [Fick (1855)].

1905 - Albert Einstein inferred the random thermal motion of molecules from the kinetic-molecular theory in the early 20th century, which was a period that a coherent description of molecular diffusion emerged. Einstein derived an explicit relationship between the root-mean-square (RMS) displacement of a diffusing particle in Brownian motion and the classical diffusion coefficient formulated in Fick's law [Einstein (1905)] (English translation in [Einstein (1956)]).

1946 - Felix Bloch and Edward Purcell were awarded the 1952 Nobel Prize in Physics for their development of new ways and methods for nuclear magnetic precision measurements. Felix proposed the Bloch equations which determine the time evolution of nuclear magnetization [Bloch (1946)]. Edward is credited for his independent discovery of nuclear magnetic resonance in liquids and in solids [Purcell et al. (1946)].

1950 - Erwin Hahn proposed the concept of spin echo sequence which is found to be sensitive to the diffusion effect. He reported that the signal attenuation of the spin echo was caused by the dephasing of diffusing spins subjected to local magnetic field gradients arisen from the inhomogeneous magnetic field [Hahn (1950)].

1954 - Herman Carr and Edward Purcell demonstrated that NMR spin echo could be sensitized to diffusion according to Hahn's observations and proposed the first diffusion-sensitizing spin echo sequence. They extended Hahn's spin echo sequence by applying a constant gradient thorough the sequence and developed a mathematical framework to estimate the diffusion coefficient [Carr and Purcell (1954)].

1956 - H.C. Torrey mathematically integrated the effect of molecular diffusion and flow into the original Bloch equation for magnetization using the magnetic flow approach. The Bloch

equation that includes diffusion as a relaxation process is know as the Bloch-Torrey equation [Torrey (1956)].

1965 - Edward Stejskal and John Tanner developed the theory and methodology of the pulsed gradient spin echo (PGSE) sequence, which established the classical method in diffusion NMR and MRI. They also provided a solution to the Bloch-Torrey equations showing how the magnitude and phase of the NMR signal is related to diffusivity, Stejskal and Tanner also solved the Bloch-Torrey equation for the case of free, anisotropic diffusion in the principal frame of reference [Stejskal and Tanner (1965)].

1973 - Paul Lauterbur is credited for the idea of adding extra magnetic fields gradients to the static magnetic field, by which different parts of object will have different resonance frequency according to the Larmor precession theory. This spatial information makes MR imaging possible [Lauterbur (1973)].

1977 - Peter Mansfield is credited for the invention of a magnetic field gradient scheme termed echo-planar imaging (EPI). This fast imaging technique greatly reduces the imaging time to tens of milliseconds, and facilitates the development of dMRI that is inherently sensitive to subject motion [Mansfield (1977)].

1984 - George Wesbey, together with Michael Moseley and Richard Ehman, initiated the field of diffusion imaging by inserting the Stejskal-Tanner pulsed gradient into an imaging sequence to measure the diffusion coefficient in structures seen in an MR image [Wesbey et al. (1984a,b)].

1985 - Denis Le Bihan published the first diffusion-weighted image using a whole-body MRI system, showing that the intra-voxel incoherent motion of water molecules can be utilized as a new contrast mechanism in MRI, particularly for the neurological applications [Le Bihan and Breton (1985); Le Bihan et al. (1986)].

1990 - Michael Moseley demonstrated the first successful clinical application of dMRI in imaging the ADC of the brain following ischemic strokes [Moseley et al. (1990a)].

1990 - David Cory and Allen Garroway developed the methodology of q-space analysis to extract microstructural information. They demonstrated that the q-space method is possible to estimate the pore size of the tissue sample [Cory and Garroway (1990)].

1991 - Paul Callaghan, a major contributor in the field of NMR microscopy, experimentally demonstrated and provided an elegant theoretical interpretation of the diffusion-diffraction

phenomenon. Callaghan also provides an outstanding review of NMR microscopy from introductory theory to the newest developments in techniques and instrumentation [Callaghan (1993)].

1994 - Peter Basser, together with Denis Le Bihan, introduced the diffusion tensor imaging, which provided a means to quantify the isotropic and anisotropic components of the diffusion tensor and is the basis for dMRI fiber mapping and tractography [Basser et al. (1994a,b)].

2.2 Diffusion Physics - Brownian Motion and Fick's Law

This section reviews how the probability density function and Einstein's RMS distance of molecular diffusion [Einstein (1956)] can be derived from the Fick's law of diffusion proposed by Adolf Fick in 1855. *Fick's first law*, which relates the diffusion flux to the concentration difference of the substance, in one-dimension is as following:

$$J = -D\frac{\partial C}{\partial r} \tag{2.1}$$

where J is the diffusion flux, a measure of amount of substance flowing into a unit area during a time interval; ∇C is the concentration gradient; r is the position; and D is the diffusion coefficient. According to Einstein relation, D explained by kinetic-theory relies on the temperature, viscosity of the fluid, and the size of the diffusing particles:

$$D = \frac{k_B T}{6\pi\nu r_p} \tag{2.2}$$

where k_B is the Boltzmann's contant; T is the absolute temperature; ν is the viscosity of the medium; and r_p is the radius of the spherical particle. *Fick's second law*, which is derived from *Fick's first law* and the conservation of mass, describes how the concentration changes with time due to molecular diffusion as following:

$$\frac{\partial C}{\partial t} = -\frac{J}{\partial r} = \frac{\partial}{\partial r}\left(D\frac{\partial C}{\partial r}\right) \tag{2.3}$$

Assuming that the diffusion coefficient D to be a constant in the space (i.e. D is independent of the coordinate or concentration), Eq. 2.3 can be formulated as below:

$$\frac{\partial C}{\partial t} = \frac{\partial}{\partial r}\left(D\frac{\partial C}{\partial r}\right) = D\frac{\partial^2 C}{\partial r^2} \tag{2.4}$$

To solve Eq. 2.4, we assume that a total amount of diffusing particles, N_p, is located at the origin

$(r = 0)$ at the beginning of diffusion $(t = 0)$. According to the principle of mass conservation, the total amount of particles (N_p) in the space surrounding the source position (r) at any time is a constant:

$$\int_0^\infty C(r,t)4\pi r^2 dr = N_p \tag{2.5}$$

where $C(r,t)$ indicates the concentration field. The solution to the above equation is,

$$C(r,t) = N_p \frac{exp\left(-r^2/4Dt\right)}{(4\pi Dt)^{3/2}} \tag{2.6}$$

The diffusion response for an instantaneous point source can be generalized to an arbitrary staring position r_0, staring time t_0, and N_p Therefore, the generalized solution to Eq. 2.5 can be expressed as below:

$$C\left(|r-r_0|, t-t_0\right) = N\left(r_0, t_0\right) \frac{exp\left[-\left|r-r_0\right|^2/4D\left(t-t_0\right)\right]}{\left[4\pi D\left(t-t_0\right)\right]^{3/2}} \tag{2.7}$$

In addition, here again according to conservation of mass, the total mass (N_p in this case) is conserved all the time. Hence,

$$\int_\infty^{-\infty} \frac{C(r,t)}{N_p} dr = 1 \tag{2.8}$$

The mass conservation principle given in Eq. 2.8 suggests that the integral, $C(r,t)/N_p$, exhibits the formal properties of a probability density function. Thus, the probability density function for a generalized point source can be formulated based on Eq. 2.7 and Eq. 2.8, as following:

$$P_s\left(r \mid r_0, t \mid t_0\right) = \frac{exp\left[-\left|r-r_0\right|^2/4D\left(t-t_0\right)\right]}{\left[4\pi D\left(t-t_0\right)\right]^{3/2}} \tag{2.9}$$

where $P_s\left(r \mid r_0, t \mid t_0\right)$ termed *diffusion propagator* is the conditional probability termed of finding a single spin at position r from initial position r_0 after any diffusion time interval $\tau = t - t_0$. From Eq. 2.9, the 3D mean-squared displacement of free diffusion for a diffusing particle following Brownian motion can be derived as below

$$\left\langle r^2 \right\rangle = 6D\tau \tag{2.10}$$

Eq. 2.10 states the relationship between the molecular displacement due to diffusion and the diffusion equation, and for free diffusion, the mean-squared displacement changes linearly with time [Einstein (1905)]. Later in Chapter 3, this equation will be employed to define the RMS distant of the random walker (diffusing spin) in *diffusion microscopist simulator*.

2.3 Principles of Diffusion NMR

Edward Stejskal and John Tanner have introduced many innovations that form the basis of the modern diffusion NMR and MRI methods. Early in 1965, they have pioneered the famous pulsed gradient spin echo (PGSE) experiment, which is still the basis of the modern diffusion imaging technique nowadays. Furthermore, they also proposed the Fourier relationship between the NMR signal and the spin displacement distribution following their PGSE experiments, which has laid the foundation of q-space theory in diffusion imaging [Stejskal and Tanner (1965)].

2.3.1 Stejskal-Tanner's Pulsed Gradient Spin Echo Experiment

As excellent comprehensive reviews of the Stejskal-Tanner's pulsed gradient spin echo experiments have been done in recent years (see [Callaghan (1993)] and [Price (1997)] for more details), here only a brief description relevant to this thesis will be presented. Stejskal and Tanner developed the PGSE pulse sequence by replacing Carr and Purcell's constant diffusion gradients with short duration and equal magnitude gradient pulses. Hence, the PGSE sequence has a clear distinction between the *diffusion encoding time* (i.e. pulse duration, δ) and the *diffusion time* (Δ) [Stejskal and Tanner (1965)]. Fig. 2.1 shows the diagram of a PGSE sequence. To correlate the NMR signal with molecular diffusion, Torrey formulated the Bloch-Torrey equation by including an additional term to the Bloch equation considering the magnetization transfer by diffusion [Torrey (1956)],

$$\frac{\partial M(\mathbf{r},t)}{\partial t} = \gamma M \times B(\mathbf{r},t) - \frac{(M_z - M_0)k}{T_1} - \frac{M_x i + M_y j}{T_2} + \nabla(\mathbf{D}\nabla M) \tag{2.11}$$

where $M(\mathbf{r},t) = M_x + M_y + M_z$ represents the macroscopic nuclear magnetization; γ is the gyromagnetic ratio; $\mathbf{r}$ is the spatial position; T_1 and T_2 are the spin-lattice and spin-spin relaxation times, respectively. $\mathbf{D}$ is the diffusion tensor which is a 3×3 rank-2 matrix. Note that the original Bloch-Torrey equation considers the case of isotropic diffusion which is described by a scalar diffusion coefficient D, nevertheless it can be generalized using a tensor.

The solution for the Stejskal-Tanner's PGSE sequence in the presence of water diffusion in an anisotropic medium is given as [Stejskal and Tanner (1965)]

$$\frac{S(t)}{S_0} = exp\left(-\frac{t}{T_2}\right) exp\left[-\int_0^t \vec{k}(t')^T \mathbf{D}\vec{k}(t')dt'\right] \tag{2.12}$$

$$\vec{k}(t) = \gamma \int_0^t \vec{G}(t')dt' \tag{2.13}$$

where S_0 is the amplitude of the initial transverse magnetization right after the $\pi/2$ radiofrequency

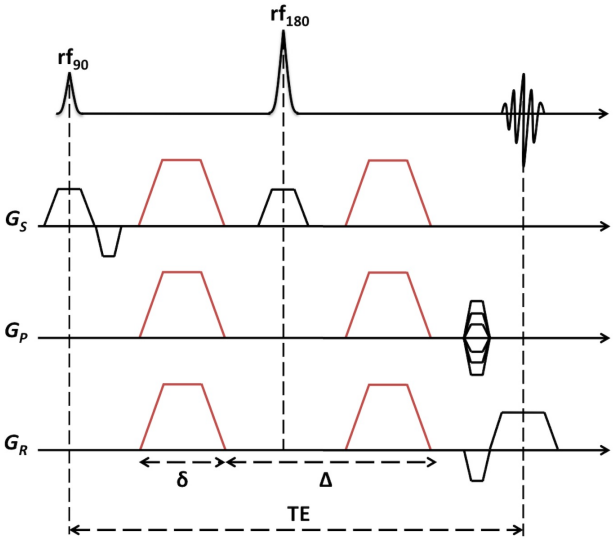

Figure 2.1: Stejskal-Tanner's PGSE sequence diagram. - After an excitation RF pulse (rf_{90}), a pair of diffusion gradients (highlighted in red) are placed before and after the refocusing RF pulse (rf_{180}). δ and Δ represent the pulse duration and separation of the two diffusion pulses. G_S, G_P, and G_R are the slice selection, phase encoding, and readout gradients respectively, and TE is the echo time of MRI signal.

pulse. For an isotropic medium, the signal at the echo time is give as

$$\begin{aligned} \frac{S(TE)}{S_0} &= exp\left[-D\int_0^{TE}\vec{k}(t')^T\vec{k}(t')dt'\right] \\ &= exp(-bD) \end{aligned} \tag{2.14}$$

where b-value is the diffusion sensitizing factor and defined as

$$b = \int_0^{TE}\vec{k}(t')^T\cdot\vec{k}(t')dt' \tag{2.15}$$

For symmetric trapezoidal diffusion gradient pulses, b-value is given as [Basser et al. (1994a)]

$$b = \gamma^2G^2\left[\delta^2\left(\Delta - \frac{\delta}{3} + \frac{\epsilon^3}{30} + \frac{\delta\epsilon^2}{6}\right)\right] \tag{2.16}$$

where ϵ is the gradient rise time, and the *effective diffusion time* (Δ_e) is usually defined as $\Delta_e = \Delta - \delta/3$ [Blees (1994); Callaghan (1993); Callaghan et al. (1999)].

2.3.2 Q-space Formalism

This section reviews the basis of the q-space imaging method, which enables us to measure the probability density function of diffusion displacement from a series of PGSE experiments without

any prior assumption on the diffusion process. The accumulative phase shift for a single spin in the present of magnetic field gradients is given as

$$\phi(t) = \gamma B_0 t + \gamma \int_0^t G(t') \cdot \mathbf{r}(t') dt' \tag{2.17}$$

where the first term represents the phase shift due to the static magnetic field B_0, and the second term is due to the effects of a magnetic field gradient. In a PGSE pulse sequence, for a diffusing spin, the degree of phase accumulation owing to the applied gradient is proportional to the spin displacement in the direction of the gradient. At the time when the spin echo is formed (i.e. the echo time, TE), the net phase shift (ϕ) of one individual spin is therefore

$$\phi = \gamma \left[\int_0^{\delta} G(t') \cdot \mathbf{r}(t') dt' - \int_{\Delta}^{\Delta+\delta} G(t') \cdot \mathbf{r}(t') dt' \right] \tag{2.18}$$

Note that the accrual spin phase depends on the its motion history during the time interval between the two magnetic field gradients. For the static spin, the phase shifts due to the gradient pulses will cancel out each other. For the diffusing spin, the spatial position $\mathbf{r}$(t) is random and the net phase shifts accumulated by individual nuclei with different Larmor frequencies will cause a reduction in the transverse magnetization.

The q-space formalism requires that the diffusion gradient pulse duration in a PGSE sequence is infinite short (i.e. $\delta \sim 0$), so that the diffusion distance under the diffusion gradient pulse duration is substantially smaller than the pore size of the medium [Wang et al. (1995)]. Under this narrow pulse approximation, the spin phase given in Eq. 2.17 is then

$$\phi = \gamma G \delta (\mathbf{r}_0 - \mathbf{r}) \tag{2.19}$$

where $\mathbf{r}_0$ and $\mathbf{r}$ are the spin's position at the first and second instantaneous gradient pulse, respectively. For a given proton density ρ, the diffusion signal taking the *diffusion propagator* (P_s in Eq. 2.9) into account is given as

$$S = S_0 \iint \rho(\mathbf{r}_0) P_s(\mathbf{r} \mid \mathbf{r}_0, \Delta) exp\left[i\gamma G \delta (\mathbf{r}_0 - \mathbf{r}) \right] d\mathbf{r}_0 d\mathbf{r} \tag{2.20}$$

Assuming that $R = \mathbf{r}_0 - \mathbf{r}$, Eq. 2.20 can be reformulated as

$$\begin{aligned} S &= S_0 \int \left[\int \rho(\mathbf{r}_0) P_s \left(\mathbf{r}_0 + R \mid \mathbf{r}_0, \Delta \right) d\mathbf{r}_0 \right] exp\left(i\gamma G \delta R \right) dR \\ &= S_0 \int P(R, \Delta) exp\left(i\gamma G \delta R \right) dR \end{aligned} \tag{2.21}$$

where $P(R, \Delta)$ expresses the average probability for a spin diffusing a distance R within a time interval Δ. It is sensible to introduce the effects of the diffusion gradient pulses into the analysis by defining the reciprocal spatial vector q given as

$$q = \frac{\gamma G \delta}{2\pi} \tag{2.22}$$

Hence, Eq. 2.21 can be rewritten as

$$\begin{aligned} S(q, \Delta) &= \int P(R, \Delta) exp\left(i 2\pi q R\right) dR \\ &= \mathcal{F}^{-1}\{P(R, \Delta)\} \end{aligned} \tag{2.23}$$

Following this Fourier relationship, a mathematical q-space analysis method was developed by Cory and Garroway [Cory and Garroway (1990)] and by Callaghan [Callaghan (1993)]. They proposed that at a sufficient Δ, the displacement probability function may relate to the size and shape (e.g. spherical, cylindrical) of the compartment where diffusion occurs. These microstructural parameters will be reflected by the diffusion-diffraction peaks in the echo signal attenuation. Therefore, the q-space imaging technique has the ability to reveal direct microstructures of the biological tissues.

2.4 Diffusion MRI in Central Nervous System

For free diffusion, the displacement probability can be described by a 3D Gaussian function, and the diffusion signal attenuation is monoexponential. In biological systems, the movements of water molecules under typical diffusion time are interfered by many tissue components, such as cell membranes, myelin sheaths, water contents and other macromolecules [Beaulieu (2002)]. In has been verified that the water diffusion is no longer Gaussian in biological tissues due to the influence of these components [Cohen and Assaf (2002)]. For neuronal fibres, water diffusion are hindered to a greater extent in a direction perpendicular to the axon axis than parallel to it because of the shape and the organization of the axonal fibres [Le Bihan et al. (1986); Le Bihan (2003)]. Therefore, with an adequate model describing water diffusion behavior, it is possible to estimate fiber directions and build the fibre connectivity map (i.e. the fibre tractography) of the brain. This sections briefly reviews the dMRI in brain tissues and begins with diffusion-weighted imaging (DWI). Then, the section describes diffusion tensor imaging (DTI), the first dMRI method to delineate fibre orientations. And next, the section summarizes the high angular resolution diffusion imaging (HARDI) techniques and different reconstruction algorithms aiming at resolving

multiple fibre orientations at the regions of complex fibre configurations. At last, the section ends with a brief summary of the fibre-tracking techniques which provide the opportunity to infer the structural connectivity of human brains.

2.4.1 Diffusion-Weighted Imaging

In 1984, Wesbey, Moseley, and Ehman initiated the diffusion imaging technique and the measurement of the diffusion coefficient by incorporated Stejskal-Tanner's PGSE sequence with imaging gradients [Wesbey et al. (1984a,b)]. In 1985, Le Bihan succeeded to acquire the first in vivo DWI of a human brain using a whole-body MRI scanner, and introduced the notion of the diffusion-sensitizing factor, b-value [Le Bihan et al. (1986)]. In 1990, Moseley discovered that DWI is highly sensitive to brain ischemia from cat brain experiments, and the following studies also suggested that the ADC drops significantly in the early stage of brain ischemia. DWI provides the chance of early detection and offers the patient to receive medical treatments while brain tissue is still salvageable. Therefore, the most important clinical discovery in DWI is Moseley's finding that DWI could detect the effect of acute stroke [Moseley et al. (1990a,b)]. According to Eq. 2.14, the scalar diffusion coefficient D can be estimated from a series of DW images with diffusion b-values by linear regression methods. As DWI is not sufficient to characterize anisotropic diffusion which naturally arises in biological tissues such as WM axons [Moseley et al. (1991)], ADC appears to be a rotational dependent quantity.

2.4.2 Diffusion Tensor Imaging

In 1994 Basser proposed the diffusion tensor model to describe the orientation dependence of diffusion signal [Basser et al. (1994b)]. Owing to water diffusion is a 3D random motion process, water molecules in biological tissue may be interfered by local tissue architecture and hence result in diffusion process which is not the same in all directions. The tensor model provides a systemic analysis approach to characterize the magnitude of *diffusion anisotropy* in the 3D space, assuming that the displacement distribution is Gaussian. The tensor model can be represented as a 3×3 matrix:

$$\mathbf{D} = \begin{bmatrix} D_{xx} & D_{xy} & D_{xz} \\ D_{yx} & D_{yy} & D_{yz} \\ D_{zx} & D_{zy} & D_{zz} \end{bmatrix} \tag{2.24}$$

As the diffusion tensor $\mathbf{D}$ is a symmetric and positive definite matrix, it has six unknown coefficients to be estimated. Hence, DTI requires at least six DW images and one reference image without

diffusion weighting to perform tensor decomposition [Basser and Pierpaoli (1998)].

$$\mathbf{D}\varepsilon_i = \lambda_i \varepsilon_i \tag{2.25}$$

where ε_i is the eigenvector of its corresponding eigenvalue λ_i ($i = 1, 2, 3$). The largest eigenvalue λ_1 gives the principal direction of the DT, ε_i, and the other two eigenvectors span the orthogonal plane to it. Several rotationally invariant scalar measures have been defined based on this eigensystem decomposition in the literature, and we will present those that have been referred to later in this thesis: the mean diffusivity (MD) and the fractional anisotropy (FA) [Basser and Pierpaoli (1996)]:

$$MD =< \lambda >= \frac{Trace(\mathbf{D})}{3} = \frac{ADC_x + ADC_y + ADC_z}{3} = \frac{\lambda_1 + \lambda_2 + \lambda_3}{3} \tag{2.26}$$

$$FA = \sqrt{\frac{3}{2}} \sqrt{\frac{\sum_i (\lambda_i - < \lambda >)^2}{\sum_i \lambda_i^2}} \tag{2.27}$$

DTI is currently the most widespread framework for characterizing dMRI data and has been used in a broad range of applications. The principle eigenvector ε_1 has been validated to be consistent well with the directions of the major white matter fibre tracts. Based on this premise, numerous fibre-tracking algorithms have been developed that rely on the DT model to deliver a reliable estimate of the WM fibre orientations. The DT model delivers a good depiction of the fibre orientation in regions where there is only one fiber population, whereas it fails in areas containing multiple distinct fibre orientations (e.g. crossing and branching fibre tracts) [Wiegell et al. (2000)]. There are two main reasons for this: (i) The DT model assumes that diffusion is purely Gaussian (i.e. free diffusion), which is apparently not the case in biological tissues. (ii) the DT model can only have a single orientation maximum, and is therefore unable to characterize a multiple orientation system. However in practice, there are many brain regions containing multiple fibre orientations, and many tracts will be affected by this problem at some point along their path. This problem may have a considerable impact on the reliability of fibre tractography. Given that the orientations provided by the tenor model are inadequate in such areas, it is necessary to implement the imaging techniques that provide higher angular resolution.

2.4.3 High Angular Resolution Diffusion Imaging

Between the years 2000 and 2011, numerous methods have been proposed to map the orientations of intravoxel incoherent fibres configurations, such as the crossing fibres. Since the main subject of this thesis does not focus on the HARDI techniques, in this section we only give a brief summary

Table 2.1: The HARDI techniques. (Abbreviations - DSI: diffusion spectrum imaging; QBI: q-ball imaging; PAS-MRI: persistant angular structure MRI; DOT: diffusion orientation transform; DPI: diffusion propagator imaging.)

Technique	Sampling strategy	Gradient orientations	b-value (s/mm^2)	Scan time (min)
DSI	Cartesian grid	≥ 200	≥ 6000	20-50
QBI	Single q-shell	≥ 60	≥ 1000 (≥ 3000 preferable)	10-20
PAS-MRI				
DOT				
CHARMED	Multiple q-shells	≥ 200	≥ 6000	20-50
DPI				
Mixture model	Single q-shell	≥ 60	≥ 1000 (≥ 3000 preferable)	10-20
Spherical deconvolution	Single q-shell	≥ 60	≥ 1000 (≥ 3000 preferable)	10-20

instead of covering all different approaches. Excellent reviews of the HARDI techniques can be found in [Seunarine and Alexander (2009); Tournier et al. (2011)].

The HARDI method successfully deals with the issue and produces more reasonable results of orientation estimation than DTI. These methods, which are different in their acquisition strategies and reconstruction algorithms, can be broadly categorized into three main groups: those based on the q-space principle [Assaf and Basser (2005); Jansons and Alexander (2003); Ozarslan (2009); Tuch (2004); Wedeen et al. (2005); Descoteaux et al. (2011)], those relying on mixture models [Hosey et al. (2005)], and those established from empirical observations [Tournier et al. (2004)]. Table 2.1 includes HARDI techniques commonly adopted to reconstruct complex fibre orientations. Typically, there are three q-space sampling strategies in HARDI: (i) sampling the whole 3D q-space Cartesian grid; (ii) sampling a single shell in the q-space; (iii) sampling multiple shells in the q-space.

Multiple fibre orientation are usually estimated and visualized using the orientation distribution function (ODF) or fibre orientation distribution (FOD), depending on the diffusion reconstruction algorithm. The ODF of diffusion spectrum imaging (DSI), for instance, is defined as the integral of PDF over the radial dimension [Lin et al. (2003); Wedeen et al. (2005); Yeh et al. (2008)]:

$$ODF(u) = \int_0^{\infty} P(r\mathbf{u})r^2 dr \sim \int_0^{r_{max}} P(r\mathbf{u})r^2 dr \tag{2.28}$$

where r_{max}, the upper limit of the integration, defined as the linear field-of-view of diffusion PDF, which is equal to the reciprocal of the minimum q-value (q_{min}), i.e., $r_{max} = q_{max}^{-1}$. ODF measures the quantity of water molecules diffused along the unit vector, $\mathbf{u}$. Fig. 2.2 illustrates an example of in vivo DSI of a human brain (see Appendix A in Chapter 2.8 for the imaging parameters).

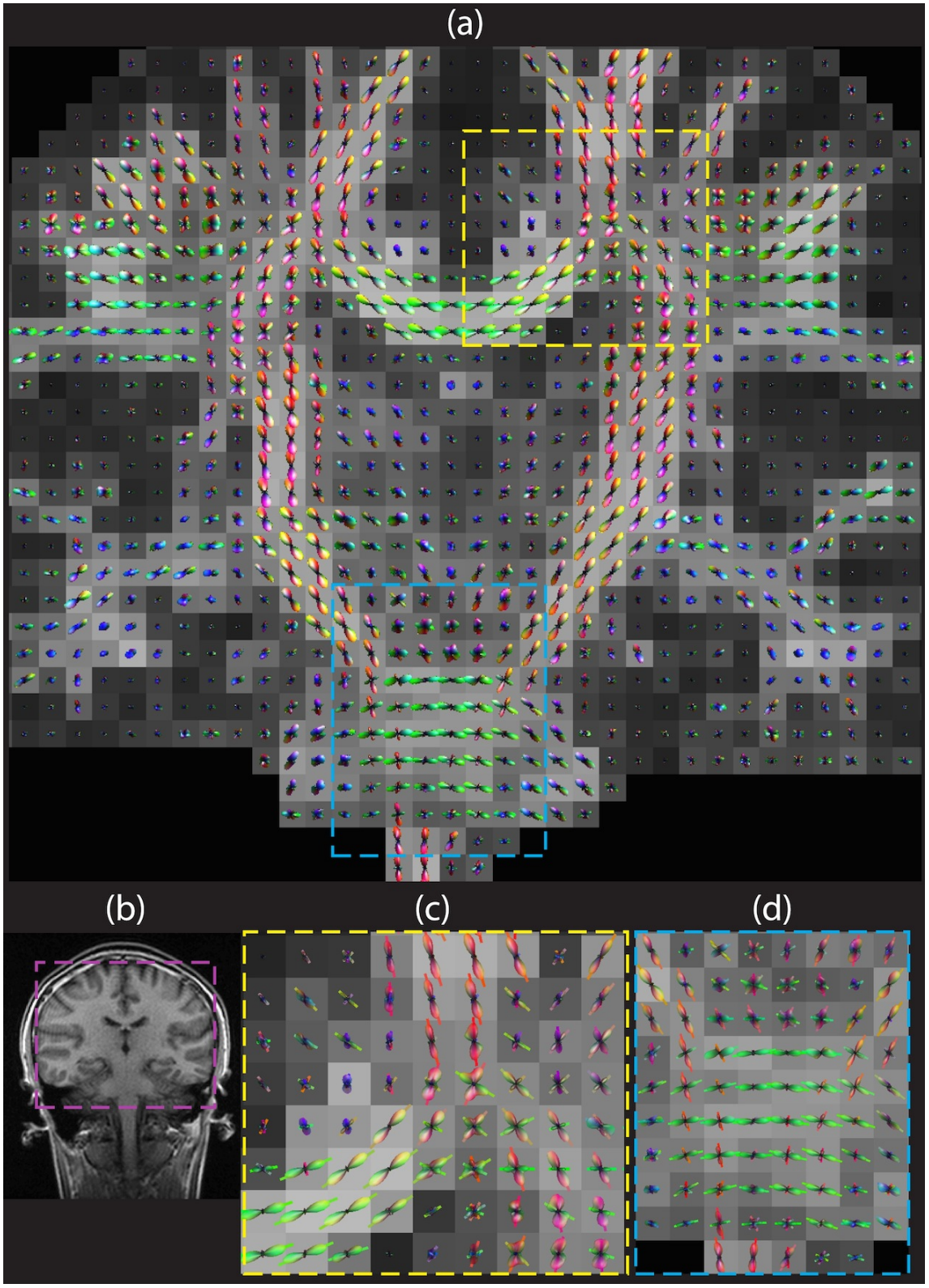

Figure 2.2: DSI of a human brain. - The figure originates from [Yeh et al. (2008)]. (a) DSI-ODF were color-coded according to their orientations (red: superior-inferior; green: medial-lateral; blue: anterior-posterior). (b) The T_1-weighted image showing the corresponding slice location of (a). (c) DSI at the centrum semiovale. (d) DSI at brain stem.

Table 2.2: A summary of fibre tracking algorithms.

	Advantages	Limitations
Deterministic	• Simple and intuitive • Computationally efficient • Producing Streamline	• Susceptible to the initialization of the seeds • Susceptible to the principal directions in the presence of noise • Less resistance to the false positive fibres
Probabilistic	• Accounting for the uncertainty in the principal direction • Handling partial volume effect and better dealing with crossing fibres • Efficient for probabilistic streamlines • Producing the quantitative connectivity score between regions	• High computations required for modeling approaches (Bayesian or others) • Requiring a large number of seeds • A large number of fibres to be handled in the post-processing step
Geodesic	• Symmetric tracking output • Theoretically elegant and potential for new connectivity metrics	• Numerically challenging to robustly implement • Hard to interpret the geodesic tracking output
Global optimization	• Global reconstruction of the structural connectivity • Better fibre detection • Better resolution to crossing fibres	• High computations required • Numerically challenging to implement and to avoid local minima

In Fig. 2.2(c), DSI-ODF resolves the crossing fibers at the centrum semiovale, where has a clear intersection between the corpus callosum and the corticospinal tract. In Fig. 2.2(d), DSI-ODF differentiated the orientations of the corticospinal tract and the middle cerebellar peduncle.

2.4.4 Fibre Tracking Techniques

The diffusion reconstruction models provide local orientation information of fibres, the integration of these information using so-called dMRI fibre tracking or tractography enables us to infer global information about the WM connections [Mori and van Zijl (2002); Behrens et al. (2007)]. At the present time, fibre tracking is the only non-invasive tool able to obtain information on the anatomical connectivity in vivo of the brain WM. Fibre tracking is most commonly implemented using the principal diffusion direction of the diffusion tensor. Many clinical MRI systems now include a fibre tracking module available for radiologists and medical experts. However, as mentioned previously in this chapter, an important limitation of the DT model is the Gaussian diffusion assumption, which implies that there can only be a single fibre population per voxel. At the resolution of DTI acquisitions, this is an important problem since it is known that many voxels have low anisotropy index due to non-Gaussian diffusion coming from multiple fibres crossing, branching, fanning or in a bottleneck. These are locations where we know that the DT model is unreliable. Thus, fibre tracking algorithms based on the DT can follow false tracts due to DT profiles that are prolate or can prematurely stop in regions of isotropic tensors. Hence, the existing DT-based tractography

algorithms have been extended to HARDI-based techniques that better deal with fibre crossings. Several fibre-tracking techniques based on HARDI data have been developed to infer the connectivity of human brain structures [Hagmann et al. (2006); Behrens et al. (2007); Hagmann et al. (2007, 2008); Wedeen et al. (2008); Chao et al. (2009); Descoteaux et al. (2009)]. While reviewing each of those methods is beyond the scope of this thesis, a summary is given in Table 2.2 which includes the pros and cons of four categories of tracking methods: deterministic, probabilistic, geodesic, and global optimization algorithms. Detail descriptions of the algorithms can be found in [Ciccarelli et al. (2008); Johansen-Berg and Behrens (2009); Hagmann et al. (2010); Lazar (2010)].

2.5 Microscopic Diffusion MRI

Recent significant advances in direct measures of tissue microstructure based on dMRI data are greatly encouraging, and importantly, dMRI is currently the only non-invasive approach that has the ability to estimate microstructure features, such as cell size, density, and membrane permeability. These direct measures of tissue characteristics can be utilized as biomarkers to monitor tissue status. This section gives a summary of microscopic dMRI.

2.5.1 AxCaliber Diffusion MRI

Assaf developed AxCaliber to estimate the diameter distribution of fibre bundles using PGSE dMRI [Assaf et al. (2008)]. The method employs a model of cylindrical axons to extract microstructure parameters through fitting dMRI data. The WM axon model, also proposed by Assaf, is a composite of hindered and restricted models (CHARMED) of water diffusion [Assaf et al. (2004)]. The hindered part is regarded as extra-axonal diffusion modeled by a diffusion tensor, and the restricted part is considered as intra-axonal diffusion characterized using q-space formalism. The general form of CHARMED is expressed as

$$S(q,\Delta) = f_h \cdot S_h(q,\Delta) + f_r \cdot S_r(q,\Delta) \tag{2.29}$$

where f_h and f_r denote the fraction of hindered and restricted compartments ($f_h + f_r = 1$); S_h and S_r are the normalized MR signal contributed from the hindered and restricted compartments.

The hindered compartment assumes that diffusion taking place in the extra-axonal space where contains numerous neural cells has a 3D Gaussian distribution. Therefore, diffusion is characterized by a diffusion tensor and, the hindered part of diffusion signal in Eq. 2.29 can be formulated as

$$S_h(q,\Delta) = exp(-4\pi^2(\Delta - 3/\delta))q^T\mathbf{D}q \tag{2.30}$$

The restricted part of diffusion signal employes the Fourier relationship between echo signal and the diffusion probability density function, as described in Eq. 2.23, and therefore

$$S_r(q,\Delta) = \iiint P(R,\Delta) exp\,(i2\pi qR)\,dR \tag{2.31}$$

In *AxCaliber* method, S_r is further decoupled into the axial and transverse signal that correspond to the diffusion signal parallel and perpendicular to the fibre axis [Assaf et al. (2008)]. The transverse diffusion signal, as described in the q-space analysis by Callaghan [Callaghan (1993)], is fitted by the analytical solution to estimate the radius of cylindrical fibres.

Note that the CHARMD model inherently assumes there is no exchange between the extra- and intra-axonal compartments. The model of diffusion within axons as restricted appears to be a valid approximation since the residence time of *intracellular* water has been estimated to be greater than 500 ms [Quirk et al. (2003)], which is much longer than a typical diffusion time of 50-100 ms typically used for human studies. However, the *extracellular* residence time is about 100 ms, which means that the water molecules in the extra-axonal space might enter into the axons during a dMRI experiment. Such effect on the MR signal of the two compartment (i.e. S_h and S_r) remains future investigations.

The possible limitation of AxCaliber for clinical MRI application is that it is rooted in the q-space formalism using a PGSE sequence. It means that a prior knowledge about the axon orientation is needed in order to acquire the axial and transverse dMRI signal for the restricted diffusion compartment. It has been shown that the dMRI signal attenuation pattern may vary significantly while the applied diffusion gradient is slightly deviated from the direction perpendicular to the fibre axis [Avram et al. (2004)]. Even though it is possible to estimate fibre orientations by HARDI, it is still difficult to apply AxCaliber to those axon fibres with more complex configurations, such as curving or branching fibres.

2.5.2 Multiple Scattering Diffusion Imaging

Multiple scattering diffusion imaging (MSDI), as first introduced in 90's by Cory [Cory and Garroway (1990)], Callaghan [Callaghan (1993)], and Mitra [Mitra (1995)], is one of the most promising methods that is feasible to extract microstructural information. More recently, MSDI has been revisited theoretically and experimentally by Ozarslan and Basser [Ozarslan and Basser (2007, 2008); Ozarslan et al. (2009); Ozarslan (2009)], Shemesh [Shemesh et al. (2009a,b)], Komlosh [Komlosh et al. (2007)], Koch and Finsterbusch [Finsterbusch and Koch (2008); Finsterbusch (2009, 2010); Koch and Finsterbusch (2008, 2009)]. MSDI employs a generalized PGSE sequence which enables

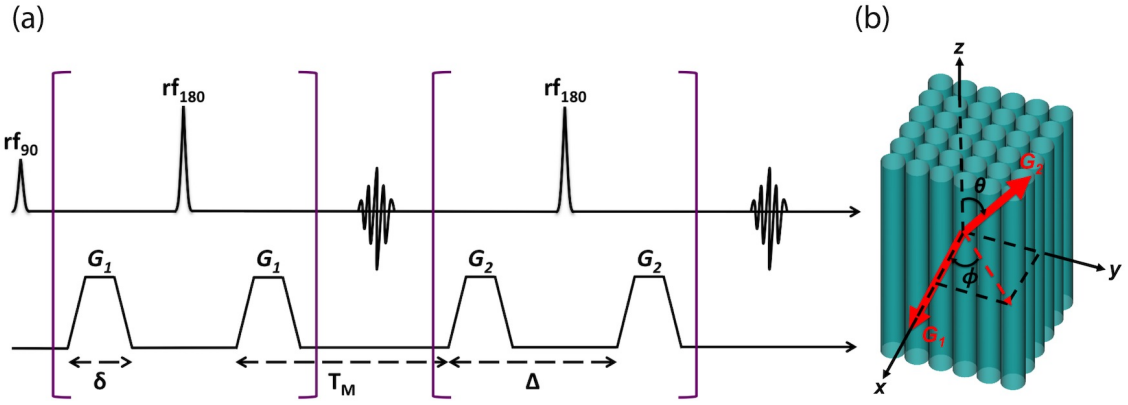

Figure 2.3: A double PGSE pulse sequence diagram. - (a) A standard double PGSE pulse sequence for the MSDI experiments considered. The diffusion mixing time (T_M) is defined as the beginning of the second and third DW gradients. Theoretically, the pair of DW gradients (shown in the purple parentheses) can be extended with multiple concatenations (i.e. multiple scattering). (b) ϕ and θ are the azimuthal and polar angles respectively. The orientations of G_1 and G_2 in (b) are varied for the angular double-PGSE experiment.

to characterize the microscopic anisotropy. Fig. 2.3 illustrates a typical double PGSE pulse sequence. MSDI can be employed to detect microscopic anisotropy based on diffusion-diffraction pattern, which has been shown to be more sensitive to microstructures than the conventional single PGSE approach. It has been verified that the q-value required to measure axon diameters from the diffusion-diffraction patterns is lower using a double PGESE than a single PGSE pulse sequence. Moreover, an angular double PGSE technique has been shown that microstructures can be extracted at a low q-value, which considerably increases its potential application on clinical MRI system in the future.

2.5.3 Temporal Diffusion Spectroscopy

The convectional PGSE methods measure at a relatively long time scale, where diffusing spins usually experience multiple interactions with the substrate, resulting variations of spatial distance to the typical cell dimensions. The oscillating gradient spin echo (OGSE) method, in which the effective diffusion is linked to the oscillating frequency of the applied gradients, has the potential to characterize the restriction effect from the cellular structures at much shorter diffusion time and length scales. High frequency gradients are beneficial to distinguish the mechanism responsible for the ADC measured in restricted systems, as they minimize effective diffusion times. The principle of temporal diffusion spectroscopy stems from the analysis of spin diffusion in the frequency domain, as proposed by Stepisnik and Callaghan [Stepisnik (1993); Callaghan and Stepisnik (1995)]. The

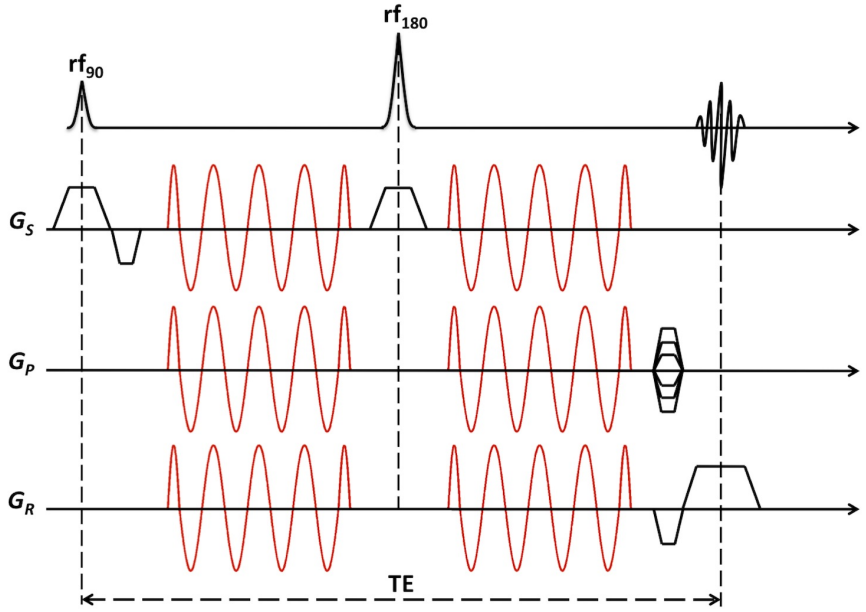

Figure 2.4: An oscillating gradient spin echo sequence diagram. - An example OGSE pulse sequence with cosine-modulated gradient waveform (highlighted in red) [Parsons et al. (2003)] used for the temporal diffusion spectroscopy imaging.

relationship between the diffusion signal and the applied oscillating gradients is formulated as

$$S = S_0 exp\left(-\frac{1}{\pi}\int_0^\infty \vec{F}(\omega)\vec{D}(\omega)\vec{F}(\omega)d\omega\right) \tag{2.32}$$

$$\vec{F}(\omega) = \int_0^\infty \left[\int_0^t \gamma\vec{G}(t')dt'\right] exp\,(i\omega t)\,dt \tag{2.33}$$

where $D(\omega)$ is the diffusion spectrum and $F(\omega)$ is the Fourier transform of the time integral of gradient. Since the OGSE method enables to selectively probe the cellular geometry over several length scales, it has the advantage over the conventional PGSE method that is relatively limited to the time and length scale. It has been suggested in the literature that the OGSE method at a sufficient oscillating frequencies has the potential to discriminate tissues that are merely different in cell nuclear sizes [Xu et al. (2009b)]. This additional sensitivity suggests that the temporal diffusion Spectroscopy technique may be significantly advantageous for characterizing tumors [Colvin et al. (2008)].

2.5.4 Active Imaging

An active imaging algorithm in dMRI refers to the method that aims to optimize a dMRI protocol for certain tissue microstructure parameters, such as cell size and density [Alexander (2008)]. As proposed by Alexander, the active imaging paradigm constitutes four key procedures:

Modeling - The first stage is to construct an adequate biological tissue model (e.g. CHARMED model of WM axons) containing the features that may affect the dMRI measurements.

Sampling - The second stage is to determine and optimize the dMRI experimental protocol and strategy (e.g. gradient sampling scheme and b-value) which can deliver the most information on the tissue microstructures given the constraints on the capability of MRI system (e.g. the maximum gradient intensity) and the acceptable scan time.

Fitting - The third stage is to fit the dMRI data, acquired using the imaging parameters optimized in the second stage, with the tissue modeling created in the first stage to extract the model parameters of tissue.

Validation - The last stage is to confirm the model parameters with the realistic biological data, which may come from the histology or other imaging modality (e.g. optical imaging).

Note that the active imaging method, importantly, does not need a prior knowledge about the fibre orientation for the purpose of fibre diameter mapping [Alexander et al. (2010); Zhang et al. (2011)]. Hence, it is more practical for actual dMRI of human brains where fibre orientations are generally unknown. Interestingly, recent studies based on the active imaging method suggests that the optimal diffusion gradient waveform for microstructures diffusion imaging is rather an oscillating gradient shape [Drobnjak et al. (2010)], which appears the link to the OGSE technique that tends to increase the sensitivity to tissue microstructures by reducing the effective diffusion time (i.e. higher oscillating frequencies).

2.6 Diffusion Functional MRI

Precise localization of neuronal activity has been reported using diffusion functional MRI (dfMRI) in recent years [Darquié et al. (2001); Le Bihan et al. (2006); Le Bihan (2007); Flint et al. (2009)], which has been demonstrated to response more directly to the neural activation than the classical hemodynamic imaging method based on BOLD (Blood-Oxygen Level Dependent) MRI signal [Ogawa et al. (1990)]. Recently advances in MRI hardware and signal-to-noise performance of scanners have led to the observation that dMRI may be used to measure functional activation. The general principle of dfMRI is rooted in the hypothesis that the variation of ADC following brain activation is originated from the expansion of the polar membrane layer during activation-induced cell swelling [Le Bihan (2007)]. As BOLD fMRI is an indirect measure of signal changes due to the blood-oxygen level, there is usually a time delay between neuronal activation and blood flow. On the contrary, dfMRI, which measures water diffusion changes in early biophysical events

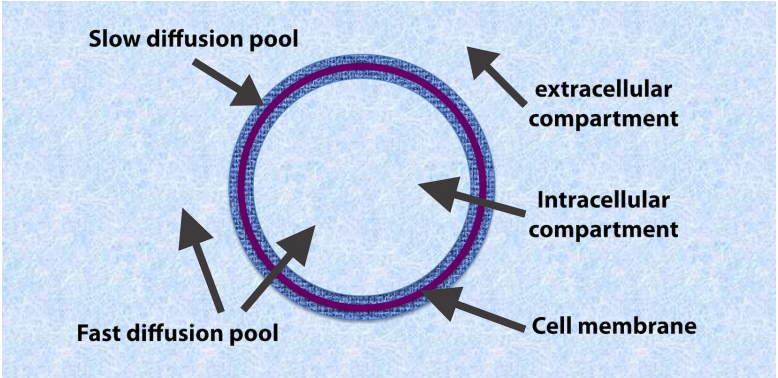

Figure 2.5: Conceptual biphasic water diffusion model. - The model proposed by Le Bihan [Le Bihan (2007)] considers that the slow diffusion pool is made of a membrane-bound layer where water molecules are trapped by the electrostatic forces of the cell membranes and the associated cytoskeleton. The water molecules in the intra- and the extracellular compartments forms the fast diffusion pool.

that occur in the activated neuronal cells, seems to be a method directly associated with the brain activation process. The time resolution and spatial localization of dfMRI appears to be advantageous. However, owing to the fact that the dMRI contrast comes from signal attenuation, dfMRI signal typically required more measurements to increase the statistical reliability, especially higher b-values are preferential to increase the sensitivity.

The principle of dfMRI is explained using a biexponential model by Le Bihan [Le Bihan (2007)]. The biexponential model, also termed two-compartment or biphasic model, ascribes the contribution of MR signal attenuation to the weighted sum of fast and slow water diffusion pool [Niendorf et al. (1996); Peled et al. (1999); Clark and Bihan (2000); Maier et al. (2004)]. Assuming that there is no or slow exchange between the two compartments, the formula is shown as follows:

$$\frac{S(b)}{S_0} = F_f exp(-bD_f) + F_s exp(-bD_s) \tag{2.34}$$

where $F_f + F_s = 1$. F and D were the model parameters that represented the volume fraction and diffusion coefficient associated with the fast and slow diffusion phases. Le Bihan proposed that as the nature of the cell membrane is structured by the charged proteins, water molecules may be trapped by those hydration layers [Le Bihan (2007)]. Thus in this model, the slow diffusion pool refers to a water layer trapped by the electrostatic forces of the protein membranes and associated cytoskeleton. The polarity of the cell membrane and the cytoskeleton limit the movement of water molecules in this layer, resulting in a lower diffusion coefficient around cell membranes. For the remaining water molecules, whether in the intra- or the extracellular compartment, constitutes the fast diffusion pool. Fig. 2.5 depicts the biphasic model of water diffusion described above.

This model also explains that water mobility (or ADC) would be reduced through an increase in the volume proportion of the slow diffusion pool due to the membrane expansion, such as during activation-induced cell swelling [Le Bihan et al. (2006)] or cell proliferation [Le Bihan (2003)].

2.7 Discussion

This chapter reviews the progression of dMRI from the diffusion physics, PGSE method, and q-space theory to modern dMRI methodologies. Thanks to the efforts that have been made by the researchers for many years, dMRI has indeed become a helpful tool for clinical diagnosis and for studying neuroanatomy and brain function. However, knowledge about the underlying biophysics that governs diffusion signal and relevant quantities remains debatable, as dMRI techniques delineate tissue features through modeling a macroscopic ensemble-averaged diffusion process. It is difficult to make inference on the characteristics of biological tissues from a MRI experiment due to the limitation of the MRI resolution. This reflects the need to have a tool which enables us to investigate the detail mechanism that governs diffusion signal and relevant quantities, as well as to validate various algorithms (i.e. diffusion reconstruction and fibre-tracking algorithms) implemented in dMRI.

2.8 Appendix

A. DSI of a human brain. DSI data of a healthy subject was obtained using a 1.5 T GE Signa EXCITE MRI scanner (GE Healthcare). Three oblique slices were acquired via a spin echo diffusion EPI pulse sequence using a 3D cartesian grid of 515 q-space sampling points with the following parameters: matrix size = 64×64; voxel dimension = 3.6×3.6×3.6 mm^3; repetition time (TR) = 3,000 ms; TE = 139.2 ms; δ/Δ = 47.8/56.0 ms. The maximum b and q-values were 10,000 s/mm^2 and 79.5 mm^{-1} respectively. The scan time was around 26 min.

Part II

METHODS

Chapter 3

Diffusion Microscopist Simulator

Contents

3.1 Introduction

3.1.1 Diffusion MRI and Tissue Microstructures - A Scaling Issue

The driving force of diffusion MRI (dMRI) is to monitor microscopic, natural displacements of water molecules that occur in brain tissues as part of the physical diffusion process. Water molecules are thus used as a probe that can reveal microscopic details about tissue architecture, either normal or in a diseased state. One has to keep in mind, however, that the overall signal observed in dMRI images at a *millimetric* resolution, results from the integration, on a statistical basis, of all the *microscopic* displacement distributions of the water molecules present in this voxel. The complex diffusion processes that occur in a biological tissue on a voxel scale are often described with a global, statistical parameter, the Apparent Diffusion Coefficient (ADC) [Le Bihan et al. (1986)]. This parameterization of the diffusion process by a global ADC is intended to represent those physical processes that occur at scales smaller than the scales resolved by the method: the large scale is imposed by technical limitations (e.g. MRI hardware), while the actual 'theatre' scale of the biophysical elementary processes is determined by physical phenomena at molecular scale. The averaging, smoothing effect resulting from this scaling presumes some homogeneity in the voxel and makes a direct physical interpretation out of the global parameter somewhat difficult, unless some assumptions can be made. The ADC in the brain is 2 to 10 times smaller than free water diffusion in an aqueous solution [Le Bihan (2003)]. High viscosity, macromolecular crowding and restriction effects have been proposed to explain the water diffusion reduction in the intracellular space [Hazlewood et al. (1991)], and tortuosity effects for water diffusion in the extracellular space [Nicholson and Phillips (1981); Chen and Nicholson (2000)]. Restricted diffusion effects, for instance, may be evaluated by changing the diffusion time [Cooper et al. (1974); Latour et al. (1994)]: the displacements of the molecules become limited when they reach the boundaries of closed spaces and the diffusion coefficient artificially goes down with longer diffusion times. Furthermore cell membranes in the brain likely hinder the water diffusion process ('hindered' diffusion, as opposed to strictly 'restricted' diffusion), even if the membranes are permeable to water, either passively or through transporters, such as the specific aquaporin channels which have been found abundant in the brain [Amiry-Moghaddam and Ottersen (2003)]. Clearly water diffusion in tissues, especially the brain, is not free and cannot be modeled by a single Gaussian distribution [Cohen and Assaf (2002)]. Moreover, the ADC depends not only on the actual diffusion coefficients of the water molecular populations present in the voxel, but also on experimental,

technical parameters, such as the voxel size, the diffusion time or the degree of sensitization of the images to diffusion (so-called b-value [Le Bihan et al. (1986)]).

Although the idea to infer tissue microstructure details from the dMRI signal alone is ill-posed, except in very specific and simple situations, the relationship between the ADC and specific tissue microscopic features is currently the object of intensive research. Some groups have tried to clarify how tissue characteristics affect the dMRI signal [Beaulieu (2002); Kroenke and Neil (2004); Schwarcz et al. (2004); Miller et al. (2007); Peled (2007); Wheeler-Kingshott and Cercignani (2009)]. Theoretical models have been proposed [Stanisz et al. (1997)], for instance based on a combination of extra-axonal water undergoing hindered diffusion and intra-axonal water undergoing restricted diffusion [Assaf et al. (2004)]. Several groups have also underlined the important role of dynamic parameters, such as membrane permeability and water exchange [Chin et al. (2004); Kärger et al. (1988); Novikov et al. (1998)], and geometrical features, such as cell size distribution or axons/dendrite directional distribution [Novikov et al. (1998); van der Weerd et al. (2002); Yablonskiy et al. (2003); Chin et al. (2004)]. Noticeably, however, all those distinct models require strong assumptions to be made about the tissue structure, which may not always match known or unknown biological reality.

3.1.2 Diffusion MRI Monte Carlo Simulations

To infer the relationship between tissue microstructures and dMRI signal, another approach is to rely on Monte Carlo (MC) simulations which have been shown to be a powerful and flexible tool to mimic diffusion processes in a wide class of systems, especially when analytical solutions cannot be obtained, due to the complexity of the system [Lipinski (1990); Ford et al. (1998); Peled (2007); Alexander (2008); Fieremans et al. (2008b); Balls and Frank (2009); Hall and Alexander (2009); Harkins et al. (2009); Imae et al. (2009); Koch and Finsterbusch (2009); Alexander et al. (2010); Budde and Frank (2010); Landman et al. (2010); Nilsson et al. (2010)]. Analytical approaches predicting the dMRI signal using the Bloch-Torrey equation, for instance [Barzykin (1998)], must rely on oversimplified biological tissue model and simple MRI pulse sequence (e.g. rectangular diffusion gradient waveform). However, in the realistic situation the tissue geometry can be very complicated so that an adequate analytical description does not exist; meanwhile the difficulty in deriving the solution to the synthetic dMRI signal may increase following the complexities of MR pulse sequences and gradient shapes. The advantage of the MC approach is its ability to track the dynamic events over space and time. It provides opportunities to investigate not only the Brownian motion in an arbitrary environment, but also any models of interactions between

spins and membranes. Hence, synthetic dMRI data generated using the MC approach can be applied to study biological properties (e.g. cell size, density, membrane permeability, etc.), as well as basic diffusion mechanisms in different compartments (e.g. presence of attractors, local viscosity, membrane interactions, etc.). Specifically, it can be adapted to examine mechanistic hypotheses for various dynamic scenarios and tissue models, such as acute ischemia or neuronal activation and cell swelling, cancer and cell proliferation, ADC and axonal fibre anisotropy in complex fibre bundles or cortex [Le Bihan (2003)]. Note that, importantly, the intrinsic challenge of the dMRI MC approach is that it requires sufficient samples in order to ensure that the stability and reliability of the simulation results. The computation will become more intensive when the system model is more complicated or realistic.

3.1.3 Modeling Biological Tissues

In principle, the MC simulation approach has the potential to mimic any tissue with great details, to account for different kinds of elementary diffusion processes and to derive the corresponding dMRI signal, providing the necessary computing power is available. As the geometry and organization of biological microstructures are extremely complicated at the cellular level (e.g. gray matter in the CNS tissues), the difficulty turns into how to represent tissue structures in the MC simulation environment. Various geometric models have been proposed to simulate tissue structures under different physiological conditions: Hall and Alexander optimized the parameters for the dMRI MC simulations in packed and swelling fibre bundles [Hall and Alexander (2009)]. Landman *et al.* developed a mesh-based axon model for diffusion simulations to study the impact of injured axonal fibres [Landman et al. (2010)]. Budde and Frank developed a neurite beading model to validate the importance of cell membrane morphology on ADC [Budde and Frank (2010)]. The MC simulations described above utilized cylinders to mimic WM fibre bundles, while it is also interesting to investigate the behavior of water diffusion in cerebral cortex and deep brain nuclei, as evidence has been shown that dMRI has the subtle sensitivity to the variation of tissue cytoarchitecture [Flint et al. (2009)]. Lipinski carried out the first MC simulation in gray matter in a simplified 2D environment with tissue geometries created by means of digital images captured from histological preparations [Lipinski (1990)]. Noticeably, for technical reasons linked to computational complexity most MC simulations have been performed in 2D, although 3D simulations would be more realistic to the biological systems. Balls *et al.* developed an efficient 3D simulation system that has capability of performing large-scale simulations on water diffusion in complicated microstructures and tissue physiology, but only to simulate conventional PGSE dMRI experiments [Balls and Frank (2009)].

3.1.4 The Ultimate Goal

In this chapter, we introduce a new MC simulation framework, *Diffusion Microscopist Simulator* (DMS), which has the ability to generate 3D tissue models of various shapes and properties, as well as to synthesize diffusion MRI signals for a large variety of MRI methods, pulse sequences design and parameters. DMS aims at (i) to bridging the gap between elementary diffusion processes occurring at a micrometer scale and the resulting diffusion signal measured at millimeter scale, providing better insights into the features observed in dMRI (e.g. variation of ADC and diffusion anisotropy with cell size distribution), and (ii) offering ground-truth information for optimization and validation of dMRI acquisition schemes for different applications (e.g. fibre-tracking algorithm, diffusion local modeling, and microscopic dMRI).

3.2 Programming Framework

DMS was developed in C++ using an object-oriented design, and each algorithm had been carefully profiled and optimized to achieve fast computations. Consequently, it naturally outperforms the MC implementation that used Java, Python, or Matlab. DMS supports multi-threading computations in order to perform large-scale simulations on water diffusion in complex environment simultaneously using high temporal and spatial resolution. Works are undergoing to combine with the Open Message Passing Interface library (Open MPI, http://www.open-mpi.org) , which allows distributing the computation on a grid of computers (i.e. multi-processing) using the MPI standard, to reach high complexity and performance simulations.

Fig. 3.1 illustrates the architectural blueprint of DMS, which constitutes two main parts: (i) a random walk Monte Carlo simulator capable of simulating the diffusion of water molecules in an arbitrary simulation environment; and (ii) an MR image synthesizer dedicated to create DW images among various MR pulse sequences. The concept for the principle components shown in Fig. 3.1 is described in the later sections. Fig. 3.2 illustrates the graphical user interface (GUI) programmed using Python (http://www.python.org) and Qt (http://qt.nokia.com) for DMS to facilitate its usage. The first generation of DMS will be available through a dedicated BrainVISA toolbox made to the community that will be downloadable at http://brainvisa.info.

3.3 Monte Carlo Simulator

This section introduces the main features of DMS MC simulator, as show in the lower part of Fig. 3.1.

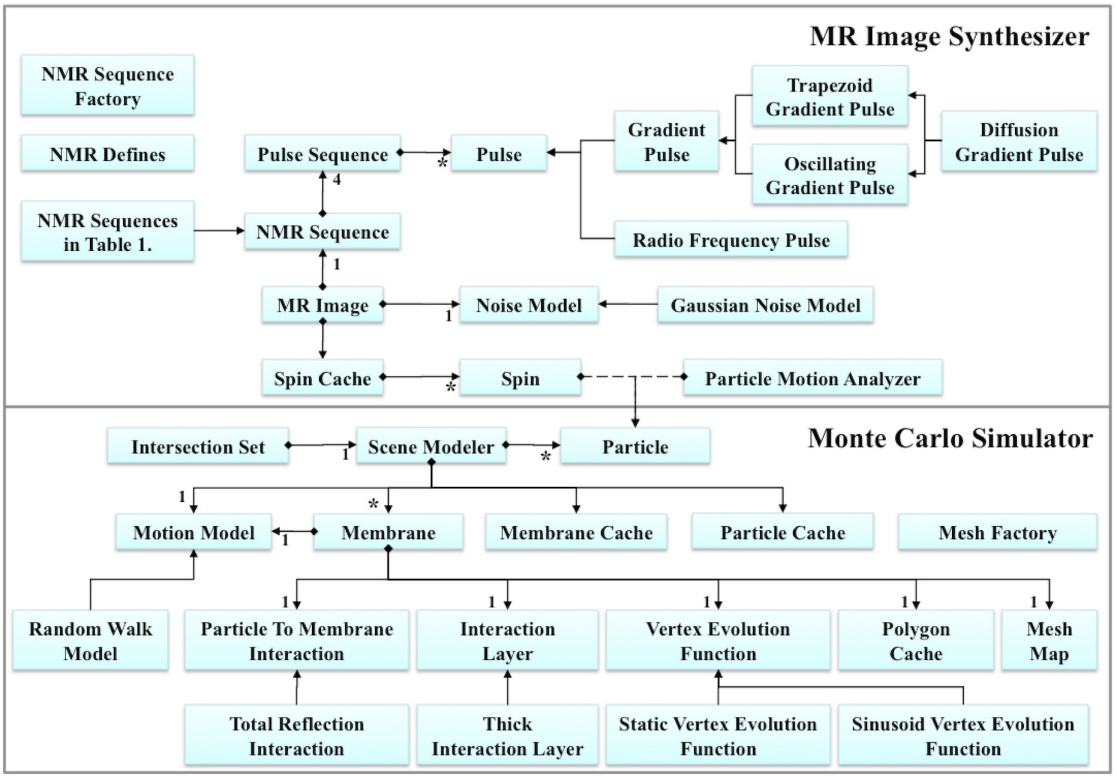

Figure 3.1: DMS: Unified modeling language (UML) diagram. - The UML diagram describes the system's framework by showing the attributes and relationships among classes. An arrow starting with a diamond represents that a class has a pointer to the objective class. The *MR Image* class, for example, needs to include one *NMR sequence*, which contains four *pulse sequences* corresponding to the RF, slice selection, phase encoding, and frequency encoding sequences while each of them may have several *pulses* (as denoted by a "*"). An arrow without a diamond indicates that the class is inherited from an objective class.

3.3.1 Scene Modeler

This class contains the essential parameters including the dimension of the spatial space, the size of spatial subvolumes (see Chapter 3.3.4), the temporal resolution (i.e. the simulation time step, t_s), the number of iteration (N_I), and the global diffusion motion model in the entire space. When the scene modeler is generated, it allows users to add cell membranes and diffusing particles into the simulation space. In addition, it contains the functions for users to visualize the 3D rendering results of dynamic cell membranes, particles and their motion trajectories.

3.3.2 Cell Membrane

Global Membrane Model

This class contains several features in order to capture the characteristics of neuronal cells. To model various cell types with heterogeneous shapes and sizes, a mesh factory was developed to

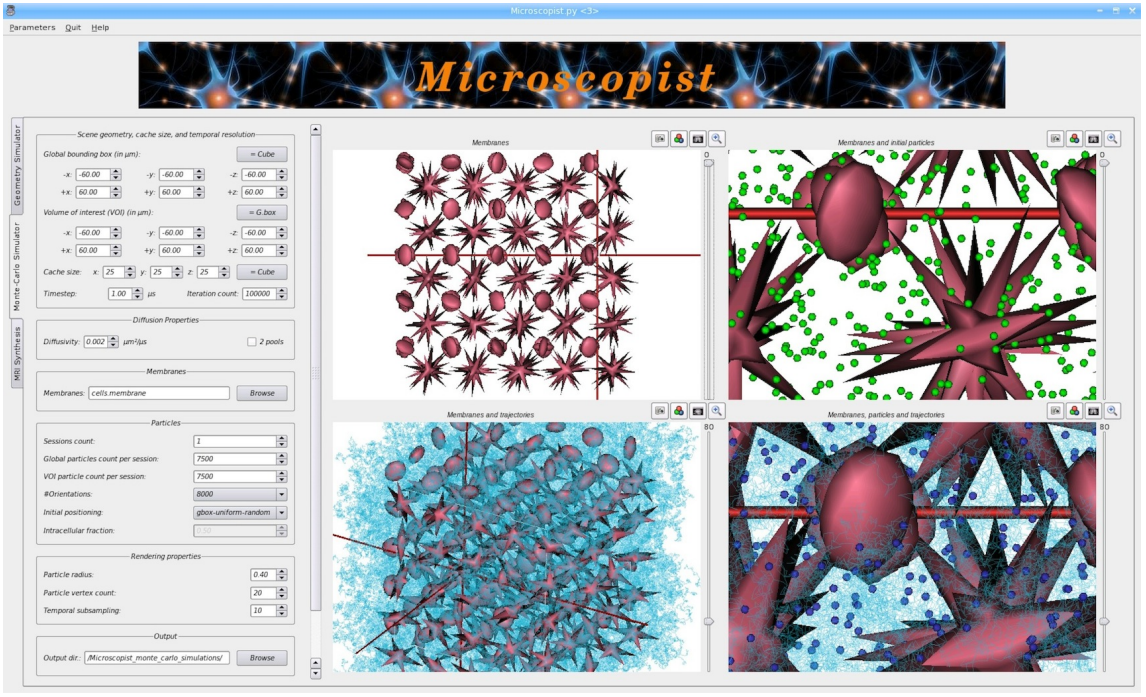

Figure 3.2: DMS: Graphical user interface. - A snapshot of the DMS GUI, which is comprised of a control panel on the left and a visualization window on the right.

generate meshes using triangles as surface elements. Mesh factory is able to produce a network of simple geometries such as ellipsoids, cylinders, and star-shape meshes in order to mimic neural architecture including neurons, glial cells, axons, and astrocytes; meanwhile, it is also feasible to construct bundles of fibres with arbitrary configurations, such as crossing, kissing, branching, and bending fibres. Fig. 3.3 & 3.4 are two examples of axon models showing that DMS has the capacity to simulate different fibre structures. Furthermore, since we incorporated a cell-membrane mesh with a dynamic morphological evolution function, each vertex can move along an averaged orientation of the normal vectors given by the adjacent polygons. The movement of the vertex follows a predefined function, for example, a sine function in our current implementation. Thus it is able to simulate sequential changes of tissue shapes including expansion, shrinkage, and deformation to simulate different tissue status. Fig. 3.5 shows an example of an environment mimicking a neural medium simulated via DMS. Movie animations of dynamic cell swelling in various views of this figure can be found in Appendix A (Section 3.8).

The basic characteristics of cell-membrane layers including the permeability and the types of particle-to-membrane interaction are fully adjustable. For the current DMS, the membrane permeability is modeled using the transmission probability, and the particle-to-membrane interaction is modeled by total reflection rule which means that the angle of incidence and reflection was identical (i.e. elastic reflection) [Balls and Frank (2009); Hall and Alexander (2009); Landman et al. (2010)].

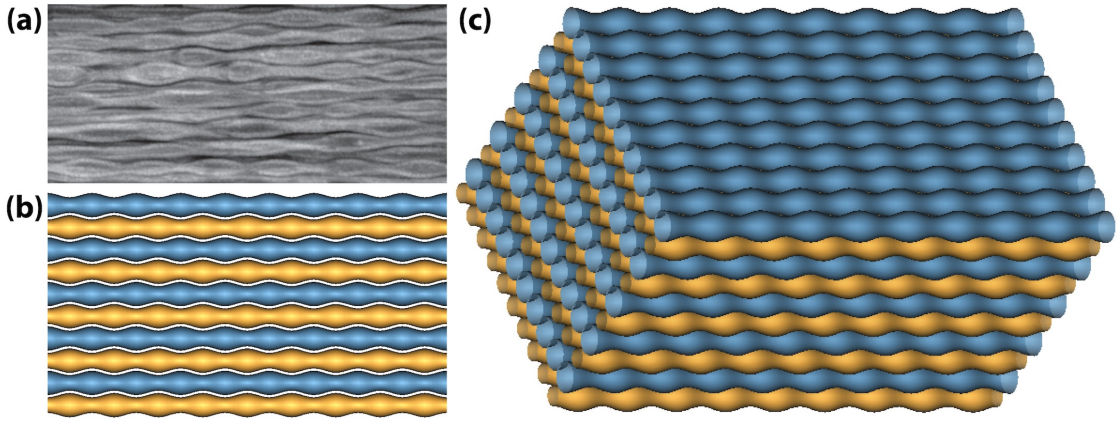

Figure 3.3: DMS: Modeling beading axons. - (a) This figure originates from Budde and Frank's article [Budde and Frank (2010)], showing the extensive beading of axonal membranes. (b) The geometric model of compact beading axons created by DMS, which contains two networks of axons (colored in blue and orange). (c) The 3D view of the beading axon model.

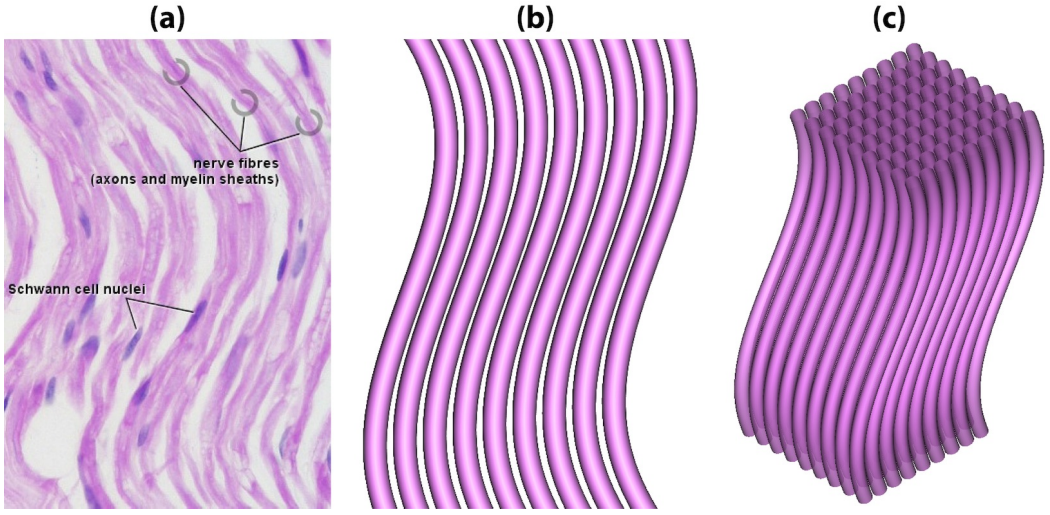

Figure 3.4: DMS: Modeling bending axons. - (a) This figure originates from the website of The University of Western Australia (http://www.lab.anhb.uwa.edu.au/mb140/), showing a longitudinal section of the peripheral nerve fibres stained by H&E (hematoxylin and eosin). (b) The geometric model of bending fibres shown in (a) modeled using DMS. (c) The 3D view of the bending axon model.

Individual Membrane Model

Models describing specific cell membrane properties can be defined to the cell-membrane layers. To simulate the hypothesis of the biphasic water diffusion model [Le Bihan (2007)], for instance, we have implemented an efficient method for a particle to discover the closest cell-membrane layer from it surroundings at each simulation iteration. While a diffusing particle (see Chapter 3.3.3 below) moves inside any of the polar membrane layer, its diffusion coefficient D is updated to that of the associated cell membrane.

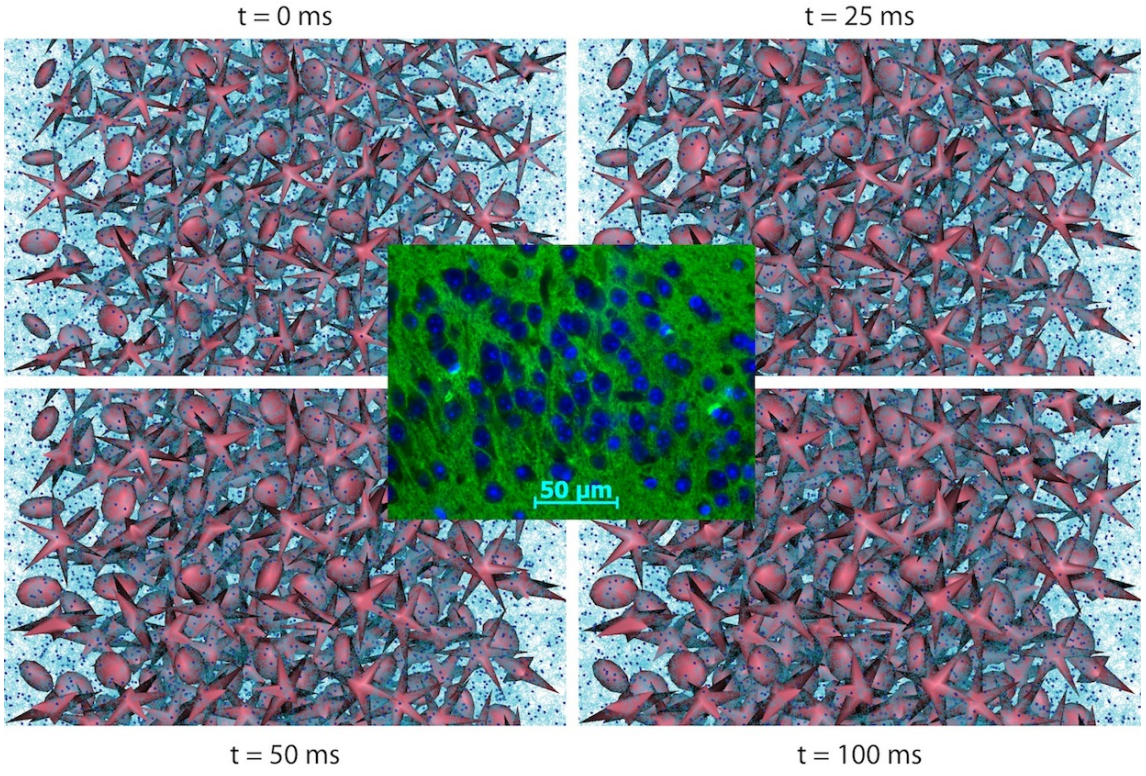

Figure 3.5: DMS: Modeling a realistic neural medium. - The figure in the middle is the result of a micrograph obtained from brain biopsy, showing an 'anaplastic astrocytoma' where neoplastic glial cells are dyed using anti-GFAP immunostain (blue). We utilized DMS to simulate this complex neural environment in 3D. Moreover, we incorporated each cell (colored in red) with a dynamic vertex evolution function to simulate cell swelling, thus the cell sizes were smallest at the beginning of MC simulation (t = 0 ms) and largest at the end (t = 100 ms). The diffusing particles and their motion trajectories were represented by dark blue spheres and light blue curves. Note that for the purpose of visualization, the extracellular space was exaggerated in this simulation.

3.3.3 Diffusing Particle

We modeled diffusing particles as random walkers. DMS allows for controlling the initial distribution of particles, which can be (i) regulated by the intra- (f_i) and extra-cellular ($f_e = 1 - f_i$) fractions determined by users, (ii) randomly allocated in the simulation scene (i.e. f_i is proportional to the total cellular volume), or (iii) located at a specific region or location defined by users. The particle positioning algorithm in DMS is applicable to any mesh-based geometry. Fig. 3.6 is an example of different positioning methods. The root-mean-squared (RMS) displacement ($\mathbf{r}$) of a particle's movement is scaled to its associated compartmental D and t_s based on the Einstein relation (see Eq. (2.10) in Chapter 2.2 for reference):

$$r = \sqrt{6Dt_s} \tag{3.1}$$

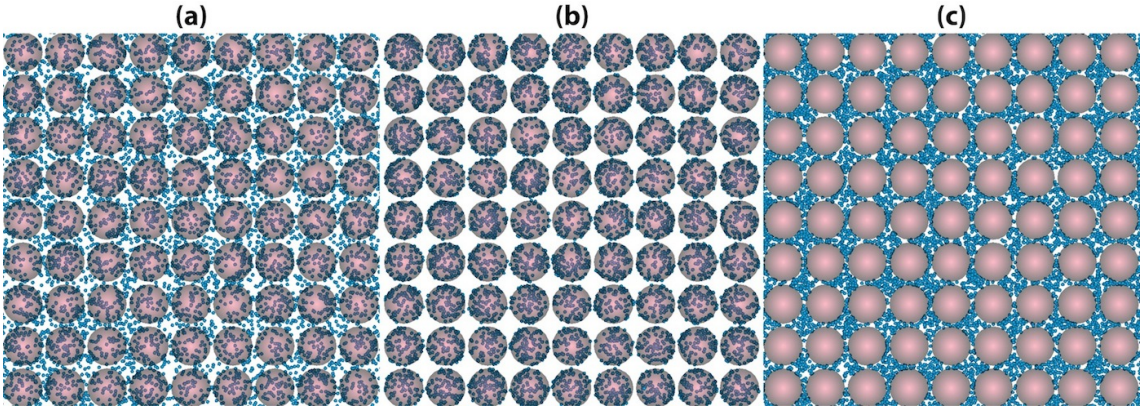

Figure 3.6: DMS: Initialization of particles' positions. - DMS allows to control the initial position of diffusing particles (colored in blue) respecting to the cell membranes (colored in pink). This figure shows a transverse view of the simulation space where cells membranes were created using cylinders and particles were placed using (a) random distribution (b) intracelluar initialization (c) extracelluar initialization.

The diffusing orientation is randomly chosen from a pre-allocated lookup table constructed with uniformly distributed orientations using electrostatic repulsion algorithm [Jones et al. (1999)]. The default orientation scheme consists of 4,000 independent directions, and the symmetric orientations are included to avoid orientation inclination (i.e. a total of 8,000 orientations). For each simulation step, the spatial positions of particles are updated subject to a series of possible interactions with cell membranes (Chapter 3.3.2): (i) In accordance with the *global membrane model*, the particle may penetrate through the interacting membrane respecting the membrane's permeability, or move following a certain particle-to-membrane interaction method. (ii) The diffusivity is updated based on the *individual membrane model*. The model of biphasic diffusion pool, for instance, will change the particle's diffusivity into the local compartmental D [Le Bihan (2007)].

3.3.4 Spatial Subvolume

For each simulation run, DMS employed the computer memory to store the 3D lookup tables that partitioned the global simulation space into a fine grid with a size of $N_x \times N_y \times N_z$, so that each local subvolume contains a subset of diffusing particles, cell membranes, and triangle meshes. Therefore, knowing a particle's position ($\vec{R}$), the time required searching and processing any potential interaction can be dramatically decreased via the direct assess to the objective cell membranes and polygons simply in the local spatial subvolume rather than the entire simulation space. Fig. 3.7 illustrates the concept of the spatial subvolume.

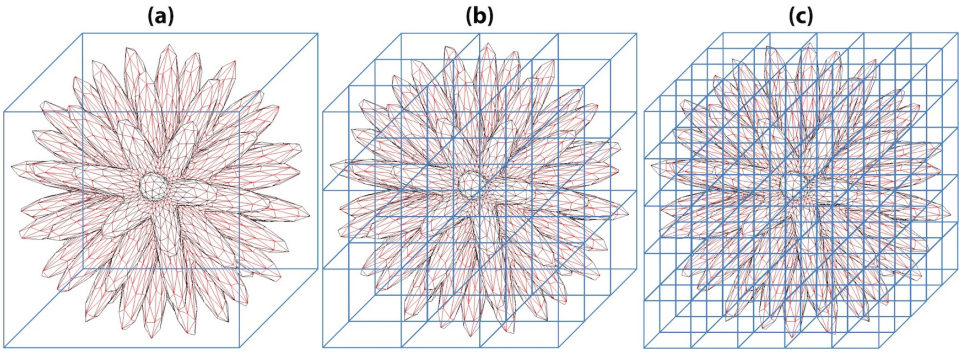

Figure 3.7: DMS: Spatial subvolumes. - To show the idea of spatial subvolume, a complex geometry created by DMS is placed inside a simulation space partitioned into $N_x \times N_y \times N_z$ = (a) $1 \times 1 \times 1$ (b) $3 \times 3 \times 3$ (c) $5 \times 5 \times 5$ subvolumes. When the size of partition increases, each subvolume contains a smaller number of mesh elements. The search for interactions between diffusing particles and mesh polygons can then be restricted to individual subvolumes, systematically increasing computing efficiency.

3.4 MR Image Synthesizer

This section introduces the main features of DMS MR image synthesizer, as show in the upper part of Fig. 3.1.

3.4.1 Spin

Global Spin System

The outputs of the *Monte Carlo simulator* are the particles' motion information, which are imported to the *MR image synthesizer* and endowed with spins, each of them storing its phase state calculated using a discrete form of Eq. (2.17) as below

$$\phi = \gamma \sum_{i=0}^{N_{TE}} (-1)^{N_{\pi RF}(t_i)} \vec{G}(t_i) \cdot \vec{R}(t_i) t_s \tag{3.2}$$

In Eq. (3.2), N_{TE} is the iteration count at TE (i.e. $N_{TE} = TE/t_s$). For a given time point t_i, where $t_i = i \times t_s$, $N_{\pi RF}(t_i)$ is the accumulated count of refocusing RF pulses; $\vec{G}(t_i)$ is the gradient vector derived from the NMR sequence (see Chapter 3.4.2) considering the waveforms of all gradients (i.e. both DW and MR spatial encoding gradients) applied along each principle gradient axis; and $\vec{R}(t_i)$ is obtained from the particle's diffusion trajectory.

Individual Spin System

The particles' motion information provides additional statistics relating to the cell membranes. For the biphasic diffusion model [Le Bihan (2007)], we can segregate the global particles into fast and

Table 3.1: DMS: NMR pulse sequences. (Abbreviations: G, gradient magnitude; SR, gradient slew rate; T_M, mixing time; N_{GP}, number of DW gradient pairs; T, period; f (=1/T), frequency of oscillation; N_{GO}, number of gradient oscillations)

NMR Sequence	Gradient waveform	Parameters
Single PGSE (Stejskal and Tanner, 1965)	rectangle; trapezoid	G; S_R; δ; Δ; TE
Stimulated-echo (STE) (Tanner, 1970)		
Bipolar STE (Karlicek and Lowe, 1980)		
Twice-refocused spin echo (TRSE) (Reese et al., 2003)		
Multiple PGSE (Callaghan and Komlosh, 2002; Mitra, 1995)		G; S_R; δ; Δ; T_M; N_{GP}; TE
Multiple STE (Cory et al., 1990)		
Bipolar double STE (Shemesh et al., 2010a)		G; S_R; δ; Δ; T_M; TE
Oscillating gradient spin echo (OGSE) (Does et al., 2003; Stepisnik, 1993)	sine; double-sine; cosine	G; T (f); N_{GO}; TE

slow diffusing particles according to their fractions of residence time within the polar membrane layer (i.e. the slow diffusion pool). Then, the spin phase for the two groups of particles can be calculated individually using Eq. (3.2). This can decouple the dMRI signal contributions from the fast and slow diffusion pools, and thus may help to investigate the impact of the polar membrane layer.

3.4.2 NMR Sequence

DMS has potential in modeling a variety of MR pulse sequences by regulating the timings of RF and gradient pulses. Table 3.1 summarizes the pulse sequences and adjustable parameters available in DMS. Gradient shapes including rectangle, trapezoid, and oscillating waves have been implemented, and can be extended to fit any design. Imaging gradients, e.g. slice selection, phase encoding, and readout gradients, are selectable to be included in a NMR sequence. The minimum echo time (TE_{min}) is automatically calculated according to the user-specified pulse sequence and related parameters. The diffusion-sensitizing factor, i.e. b-value, is given by the discrete form of Eq. (2.15) as

$$b_n = t_s \sum_{i=0}^{N_{TE}} k_n(t_i) k_n^T(ti) \tag{3.3}$$

In Eq. (3.3), b_n represents the b-value for the nth DW gradient orientation, and k_n is formulated according to the Eq. (2.13) as following

$$k_n(t_i) = \gamma \sum_{t=0}^{t=t_i} \vec{G}(t) t_s \tag{3.4}$$

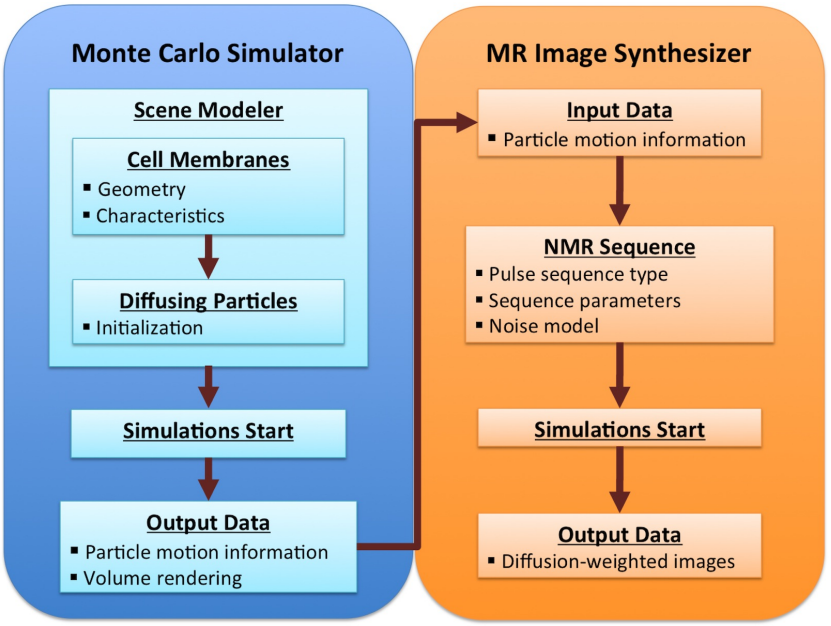

Figure 3.8: DMS: Workflow. - DMS has two main stages to generate synthetic dMRI data, (left) the random walk MC simulation of water diffusion and (right) the synthesis of dMRI dataset.

3.4.3 MR Image

This class is created to integrate spins' phases and to synthesize DW MR images. The noise model, e.g. complex Gaussian noise with zero mean and standard deviation specified by users, can be added to the synthesis data at both the real and imaginary channels. DW signal of any MR voxel, $S(v)$, is computed by performing the numerical integration using the following equation:

$$S(v) = S_0(v)\left|\sum_{\forall p, p\subset v}^{N_{p,p\subset v}} e^{j\phi_p} + \eta\right| \tag{3.5}$$

In Eq. 3.5, $S_0(v)$ is the signal intensity without diffusion-weighting for the voxel v; ϕ_p is the accumulated phase of the pth particle calculated using Eq. (3.2), and $N_{p,p\subset v}$ is the amount of particles located inside v at TE; η denotes the complex noise term.

3.5 Results and Discussion

3.5.1 DMS Workflow

Fig. 3.8 illustrates the summary of DMS workflow. DMS has integrated several features to keep the generality, nevertheless users simply need to execute two command-lines to run a complete

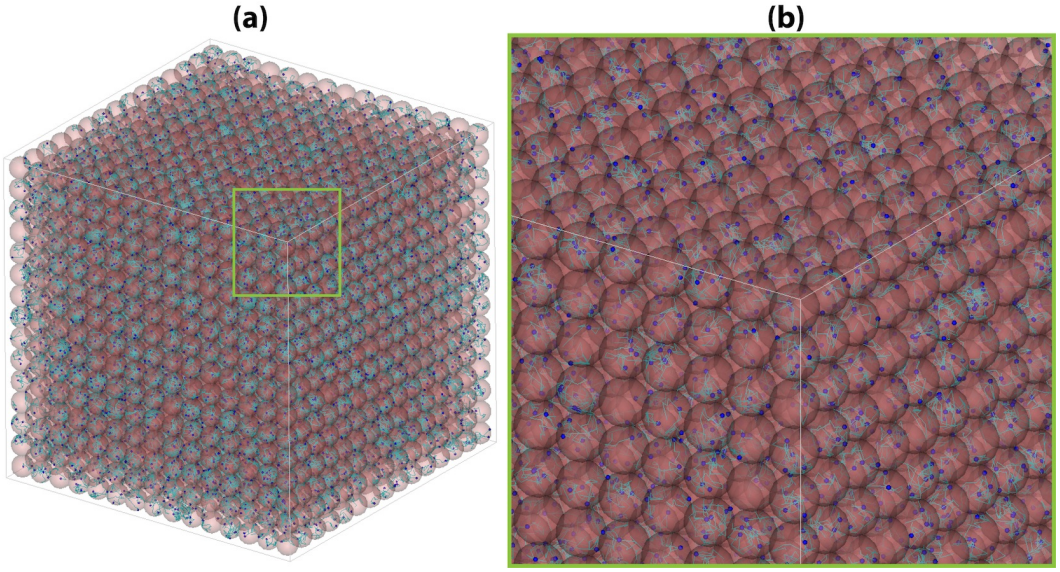

Figure 3.9: DMS: Computing performance (I). - The MC simulation scene prepared for assessing the function of spatial subvolumes. (a) The global view of the simulation environment, where a network of spheres were built on a cubic lattice with a size of 15×15×15. (b) A zoomed region showing the renderings of cells (the transparent red spheres), particles (small blues spheres) and trajectories (light blue curves).

simulation, i.e. the MC simulation and the MR image synthesis. In the first stage, users need to define the simulation parameters including the dimension of simulation space, N_p, N_I, t_s, D, $N_x \times N_y \times N_z$, cell membranes' properties, and particles' initial positions, while in the second stage, users need to determine pulse sequence to dMRI data synthesis. Furthermore, the DMS GUI shown in Fig. 3.2 is user friendly which removes the potential barrier associated with command-line programs.

3.5.2 Computing Performance (I)

To evaluate the influence of *spatial subvolume* on computing time, we performed MC simulations using different sizes of volume partitions. We placed a network of cells containing $15 \times 15 \times 15$ mesh-based spheres with a radius of 5 μm in a simulation space with a dimension of $150 \times 150 \times 150$ μm. The space was then partitioned by a grid volume with the size ranging $10 \times 10 \times 10$ to $50 \times 50 \times 50$. For each grid size, MC simulations were repeated ten times using $N_p = 10^4$, $N_I = 10^3$, $t_s = 10$ μs, and $D = 0.001$ mm^2/s. All diffusing particles were initialized inside the restricted spheres (i.e. intracellular diffusion) to ensure more particle-to-membrane interactions. The computer was equipped with a 2.66 GHz Intel Core 2 Duo processor and a 4 GB 1067 MHz DDR3 memory. For simplicity, the experiments were performed using a single thread. The results summarized in Table 3.2 showed that increasing the number of partitions effectively reduced the simulation time.

Table 3.2: DMS: Improvement of computing efficiency by the spatial subvolume method. The elapsed times were (mean ± standard deviation) recorded for the MC simulations using different dimensions of spatial subvolumes.

$N_x \times N_y \times N_z$	$10 \times 10 \times 10$	$20 \times 20 \times 20$	$30 \times 30 \times 30$	$40 \times 40 \times 40$	$50 \times 50 \times 50$
Elapsed Time (s) (mean ± std)	973.15 ± 0.19	252.91 ± 0.12	121.21 ± 0.08	114.01 ± 0.04	110.61 ± 0.07

Although we did not try to optimize the dimension of spatial volume for DMS MC simulations, we expect that the selection of the grid size relies on the resolution of the mesh element, the RMS displacement of the diffusing particle, and the available computer's memory. According to our experiences, a grid size between $50 \times 50 \times 50$ and $100 \times 100 \times 100$ can produce a more reasonable gain in time.

3.5.3 Computing Performance (II)

To evaluate the computing efficiency of DMS for a complete dMRI simulation, we performed a basic dMRI simulation experiment on WM fibres using the same computer system in the previous section (Chapter 3.5.2). We constructed a hexagonal array of 400 impermeable fibres with the diameter, center spacing, and length of 10, 10.1, and 250 μm, respectively. Each fibre was formed using a mesh-based cylinder with 40 triangles. The MC simulation parameters were: $N_p = 10^4$, N_I = 7,000, t_s = 10 μs, and D = 0.002 mm^2/s. For the dMRI signal synthesis, we used a single PGSE sequence with the following parameters: G = 40 mT/m, SR = 200 T/m/s, δ/Δ/TE = 31.7/37.7/70 ms, b-value = 2,600 s/mm^2, and a uniform DW gradient scheme of 100 orientations. The experiments were repeated ten times. The average time requirements were 396.7 ± 5.5 and 108.8 ± 2.2 seconds for the MC simulations and MR image synthesis, respectively. Accordingly, we conclude that DMS is able to complete a simulation within 10 minutes with a system complexity of $N_p \times N_I \sim 10^7$, which can be already sufficient to generate a reliable DW dataset for basic tissue configurations [Hall and Alexander (2009)]. However, it is still important to note that a high performance computing system (e.g. a workstation or computer clusters) is required for simulations at larger scales (i.e. finer resolution of tissue architecture, higher temporal resolution, larger amount of diffusing particles, and more complicated particle-to-membrane interaction models).

3.5.4 Data Management

DMS separates the Monte Carlo simulation and MR image synthesis into two steps: (i) the MC simulation stage processes particles' motion and their interactions with tissue model; and (ii) the

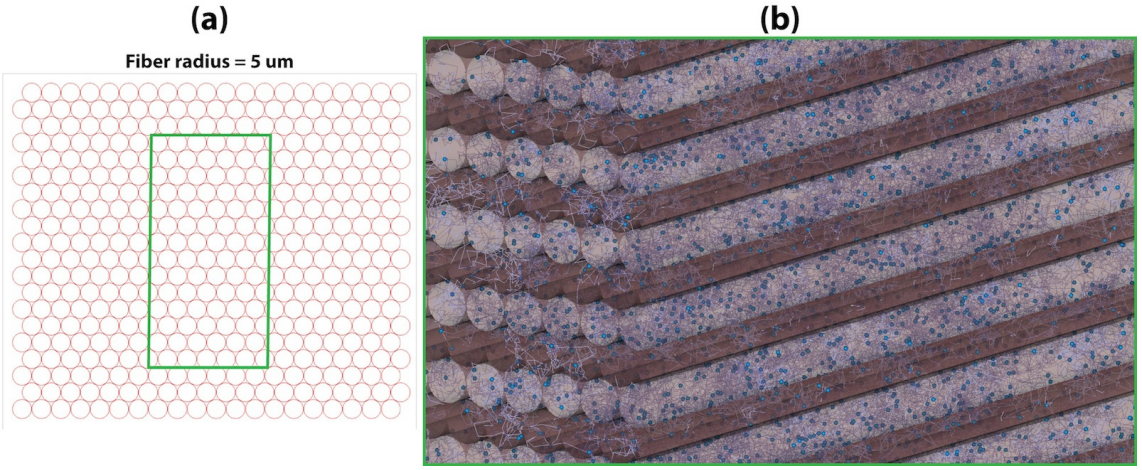

Figure 3.10: DMS: Computing performance (II). - The MC simulation scene prepared for assessing the computing time of DMS. (a) The transection view of the simulation environment, where a hexagonal network of cylinders were built. (b) A sagittal section of the fibres showing the renderings of fibres (the transparent red cylinders), particles (light blues spheres) and trajectories (purple curves).

MR image synthesis stage calculates phase information, which 'converts' diffusing particles into spins. Since the latter requires particles' motion trajectories for computing spins' phase evolution, the trajectories are stored on the hard drive at the end of the former stage. Although recording all particles' trajectories takes a considerable amount of disk space (usually tens to hundreds gigabytes, depending on N_p and N_I), it can be beneficial when the purpose is to synthesize many DW datasets with various imaging pulse sequences and acquisition schemes. In this case, it may be even inappropriate to repeat MC simulations in order to avoid variations. For example, if one is interested in studying the impact of the oscillation frequency in an OGSE sequence, DMS loads particles' trajectories once from the hard drive, from which the spin phases can be obtained with a variety of frequencies using Eq. (3.2).

The other challenge of saving the particles' trajectories is that the system memory may not be sufficient to perform a large-scale simulation using large numbers of particles (N_p) and iterations (N_I) at once. In addition, the mesh-based tissue geometries may occupy a great portion of memory when the spatial subvolumes are built at a fine resolution. To address this problem, DMS utilizes a mechanism that divides the process of Monte Carlo simulations into several sessions. Each session contains a subset of particles that does not exceed the memory limit of the computer system. The consequence drawback of this procedure is that it takes time to get access to the hard disk, nevertheless, it can effectively enables the DMS software to run basic dMRI MC simulations on a computer with limited system memory.

3.6 Summary

Diffusion MRI MC simulations have already been adopted to address several questions in the community. Many elaborate simulation tools have been proposed to generate synthetic dMRI dataset using MC simulation approach, however, they are usually designed for a particular research topic. In this chapter, we describe the structure and the main components of DMS, which is developed without prior intention to certain topics in dMRI. We believe that the generality of DMS will enable the community to perform various dMRI simulation experiments and to address different issues. To our understanding, DMS is the first integrated MC simulation software that possesses the capability of performing simulations of dMRI using various tissue characteristics and NMR pulse sequences. DMS is flexible to make extensions, and the current version is already applicable to different topics in diffusion MRI, such as tissue modeling, diffusion physics, diffusion local modeling, fibre tracking, diffusion pulse sequence optimization, and post-processing techniques. In the following chapters, we will first use DMS to run basic experiments to examine its validity and performance (Chapter 4), and then, we will apply DMS to study more specific questions (Chapter 5 & 6).

3.7 Acknowledgments

Many thanks to Benoit Schmitt for the contributions on the development of the graphical user interface of *Diffusion Microscopist Simulator* and on the processing of the histological images of tissue biopsy.

3.8 Appendix

A. Supplementary data Supplementary data associated with this chapter can be found in the online version.

Chapter 4

Benchmark Experiments

Contents

4.1 Multiple Scattering Diffusion Imaging

We used DMS to simulate single PGSE dMRI experiments on virtual WM fibre bundles as well as multiple scattering diffusion imaging (MSDI) experiments using a double PGSE sequence. The purpose was to demonstrate that DMS can produce the comparative simulation results with those well documented in the literature to validate the performance of DMS.

4.1.1 DMS Experimental Design

We employed DMS to create a simulation space (460×400×1,000 μm^3), where a bundle of straight parallel impermeable fibres with a diameter and length of 19 and 1,000 μm were placed on a 24×24 hexagonal lattice using a center spacing of 19.1 μm. The WM fibers were modeled using cylinders built by meshes using 40 polygons per cylinder. The size of the spatial subvolume ($N_x \times N_y \times N_z$) was 160×160×20. We performed random walk MC simulations using $N_p = 5\times10^5$, $N_I = 10^5$, and $t_s = 5$ μs. The compartmental D of 2×10^{-3} mm^2/s was assumed to be identical in the intra- and extra-cellular spaces. Synthetic dMRI datasets were then collected using a single (Fig. 2.1) and a variant of double PGSE sequence with $\delta = 2$ ms, $\Delta = \Delta_1 = \Delta_2 = 200$ ms, and $\mathrm{T}_M = 0$ ms for the double PGSE sequence illustrated in Fig. 4.1(b) [Shemesh et al. (2009a)]. A range of G (slew rate (SR) = 5,000 T/m/s) from 0 to 1,200 mT/m with a 10 mT/m increment were applied for the single PGSE, and $G_1 = G_2$ from 0 to 600 mT/m with a 5 mT/m increment were used for the double PGSE. The DW gradient was applied in a direction perpendicular to the fibre axis. Note that this MSDI experiment reflected the case of a preclinical MR system.

We also used the same MC simulation data to investigate the influence of N_p on the dMRI signal synthesis. Simulated data was generated using N_p varying from 10^5 to 5×10^5 for the single PGSE sequence with the same parameters described above.

4.1.2 Results

Figs. 4.2(a-b) illustrated the organization and the 3D rendering of the MC simulation, and Fig. 4.2(c) showed the results of DW signal attenuation obtained from the single and double PGSE measurements. For comparison, the normalized signal decay was plotted against $2q$ for the double PGSE. The first diffusion-diffraction trough was observed at a q-value of 655.7 cm^{-1} for both sequences, corresponding to an estimated fibre diameter of 18.6 (= 1.22×10^4 / 655.7) μm based on Callaghan theory [Callaghan (1993)]. Fig. 4.3 showed that the minimum dMRI signal (i.e. the diffraction peak) increased almost an order of magnitude (from 10^{-3} to 10^{-2}) while N_p was decreased from 5×10^5 to 10^5.

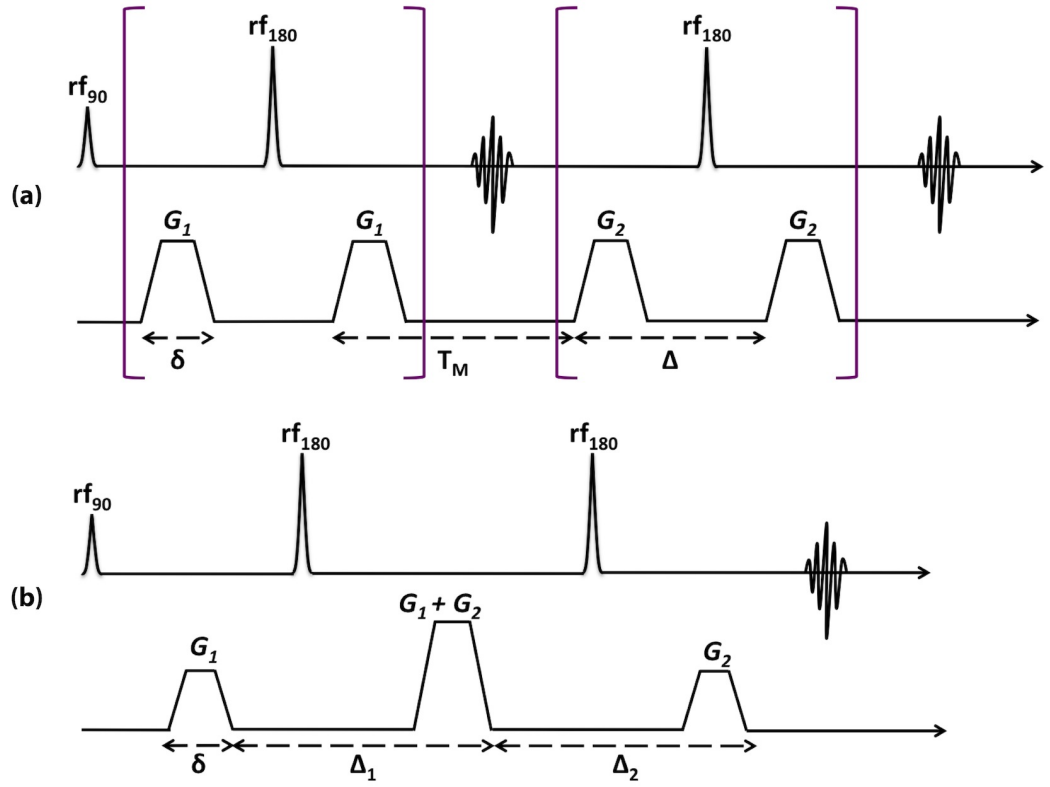

Figure 4.1: The double PGSE pulse sequence and its variant. - (a) The standard double PGSE. (b) The d-PGSE variant considered in the MSDI simulation experiments. Note that the G_1 and G_2 were superposed, resulting the mixing time effectively 0.

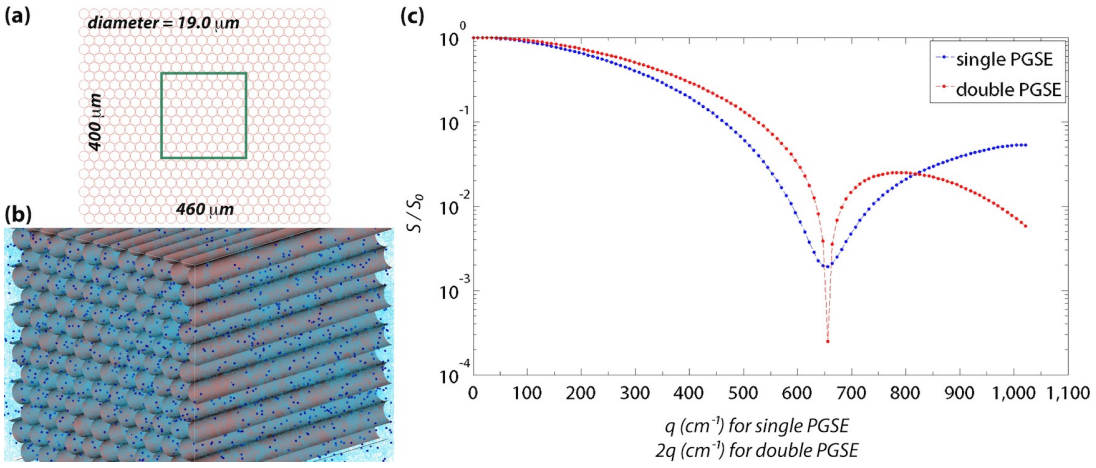

Figure 4.2: Diffusion-diffraction patterns obtained from single and double PGSE experiments. - (a) The transverse view of the hexagonal network of mesh-based cylindrical fibres, which had a diameter of 19 μm. (b) A snapshot of the MC simulation scene illustrating the zoomed area within the green square in (a), where the dark blue spheres and light blue curves are the diffusing particles and their corresponding diffusion trajectories, respectively. (c) The diffraction trough occurred at $q = 655.7$ cm^{-1}, giving an estimated pore size (i.e. fibre diameter) of 18.6 μm. The result was closed to the actual diameter of 19 μm used in the MC simulations.

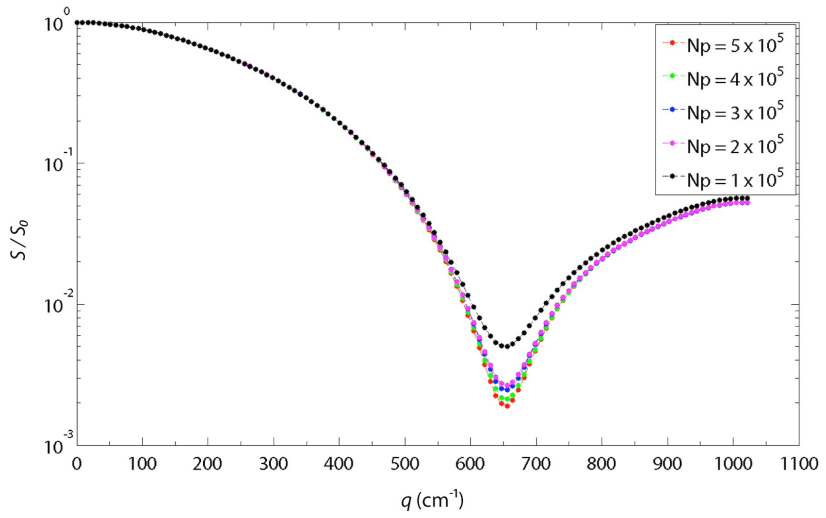

Figure 4.3: Effect of particle count on the synthetic dMRI signal. - While the number of particles (N_p) decreased, the diffusion-diffraction trough became less obvious.

4.1.3 Discussion

MSDI is a generalized PGSE technique that has the capacity to explore compartment anisotropy, pore size and shape at microscopic level via its sensitivity to small compartmental dimension [Ozarslan and Basser (2008); Shemesh et al. (2010a,b)]. Microstructural information can be estimated from the 'diffraction' pattern of DW signal attenuation [Ozarslan and Basser (2007); Shemesh et al. (2009b, 2010b)]. Ozarslan *et al.* [Ozarslan and Basser (2008)] and Shemesh *et al.* [Shemesh et al. (2010a,b)] performed MSDI experiments using a double-pulsed-field-gradient sequence to explore compartment anisotropy, pore size and shape at microscopic level. Our MSDI simulation results using a single PGSE sequence matched well to the theory proposed by Callaghan [Callaghan (1993)], and the results using a double PGSE sequence were consistent with those shown by Shemesh *et al.* [Shemesh et al. (2009a)]. These results support the validity of DMS.

As suggested by the results shown in Fig. 4.3, an adequate number of particles is necessary for high q- or b-value dMRI experiments, which is consistent with the conclusion in [Balls and Frank (2009); Hall and Alexander (2009)]. Furthermore, it is also understandable that the impact of N_p and N_I could be more evident following more complicated tissue configurations and models. In such cases, the simulation system has to be able to perform large-scale simulations using parallel computing technologies in order to generate reliable synthetic data within an acceptable simulation time. According to the results in this section as well as those presented by [Hall and Alexander (2009)], we will use an adequate combination of N_p ($\geq 10^5$) and N_I ($\geq 10^3$) to produce a reasonable simulation complexity (i.e. $N_p \times N_I$) with a minimum order of 10^8 in the following benchmark experiments.

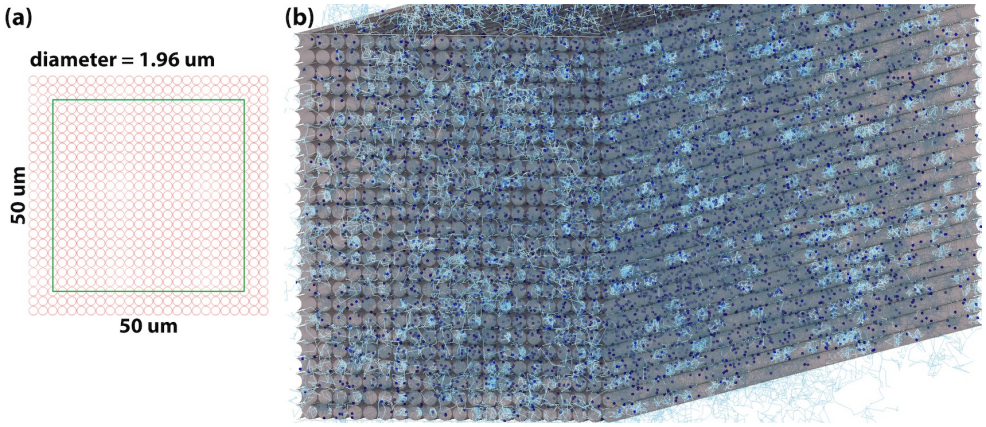

Figure 4.4: DMS simulation scene for the OGSE experiments. - (a) The transverse view of the cubic network of cylindrical fibres with a diameter of 1.96 μm. (b) The renderings of the MC simulation scene illustrating the zoomed area within the green square in (a).

4.2 Temporal Diffusion Spectroscopy

In this section, we demonstrated that DMS is able to simulate different kinds of OGSE sequences for dMRI signal synthesis. This will make DMS a helpful tool to simulate temporal diffusion spectroscopy experiments. Here we compared the results of diffusion echo signal attenuation to the data demonstrated by Xu [Xu et al. (2009a)].

4.2.1 DMS Experimental Design

We followed the simulation proposed by Xu *et al.* [Xu et al. (2009a)] and extended it using different oscillation waveforms and frequencies. We generated a simulation space ($50\times50\times200$ μm^3) where straight parallel cylinders with 200 μm in length were placed on a 25×25 cubic lattice with the spacing of 2.1 μm to simulate a bundle of axons. Impermeable axonal membranes with a diameter of 1.96 μm similar to the size of human brain were built using meshes of 40 polygons per axon. Fig. 4.4 illustrated the MC simulation environment for this section. The size of the spatial subvolume ($N_x\times N_y\times N_z$) was $50\times50\times50$. We performed large-scale random walk MC simulations using N_p = 10^6, N_I = 6×10^4, and t_s = 1 μs giving a RMS distance of 0.1 μm. The selection of N_I and t_s produced a simulation interval of 60 ms, which was considered prior to the stage of MRI signal synthesis by taking account of the typical TE used in the realistic dMRI experiments. (Note that this strategy to determine N_I and t_s was also applied to the other benchmark experiments.) The compartmental D of 2×10^{-3} mm^2/s was assumed to be identical in the intra- and extracellular space. Synthetic dMRI datasets were then collected using cosine- (Fig. 4.5), sine- (Fig. 4.6), and double-sine-modulated OGSE diffusion sequences (Fig. 4.7) [Does et al. (2003)] with a fixed waveform duration of 20 ms, which resulted in a TE of 50.5 ms. For each gradient waveform, seven

oscillating frequencies (f = 0.1/0.2/0.4/0.8/1.2/1.6/2.0 kHz) were used to study the frequency dependency, giving a range of effective diffusion times (Δ_e) from 37.5 to 0.125 ms. For each f, the transverse dMRI signal was calculated at 11 b-values ranging from 0 to 500 s/mm^2 obtained by varying the gradient amplitude G that was relevant to the gradient characteristics of the preclinical MRI systems.

4.2.2 Results

In Figs. 4.5-4.7, the left column illustrated the profile of diffusion gradient at an oscillating frequency of 0.2 kHz, and the right column showed the dMRI signal attenuation and its dependence on the waveform and frequency. For each waveform, larger signal decay was observed at higher frequencies of diffusion gradients, which implied that ADC was higher for a shorter Δ_e. The results suggested that a higher f was more sensitive to the fast diffusion compartment. These results were consistent with those shown by Does *et al*. [Does et al. (2003)] and Xu *et al*. [Xu et al. (2009a)].

4.2.3 Discussion

The temporal diffusion spectroscopy enables investigation on water diffusion behavior at various diffusion time scales (i.e. the temporal resolution) via the implementation of an OGSE sequence, by which the sensitivity to dMRI measurements to tissue microstructure can be increased [Stepisnik (1993)]. Xu *et al*. [Xu et al. (2009a)] has showed its potential to accurately provide the characteristics of the tissue cytoarchitecture (e.g. intracellular structures) and obtain structural parameters of the tissue sample, while Dose *et al*. has demonstrated the feasibility of ex vivo experiments. Our DMS experiments showed the coherent results to their studies, and thus DMS may apply to further OGSE simulations.

4.3 Tissue Characteristics and Models

We used DMS to perform large-scale simulations to study the effect of cell swelling and two-pool diffusion model [Le Bihan (2007)]. The synthetic dMRI data was analyzed using the biexponential model as well as the diffusion tensor (i.e. monoexponential) method to estimate the ADC.

4.3.1 DMS Experimental Design

We prepared ten simulation spaces with the same dimension of 100×100×100 μm^3, where each of them contained a hexagonal network of spherical cells with a total number of 9,200. For each

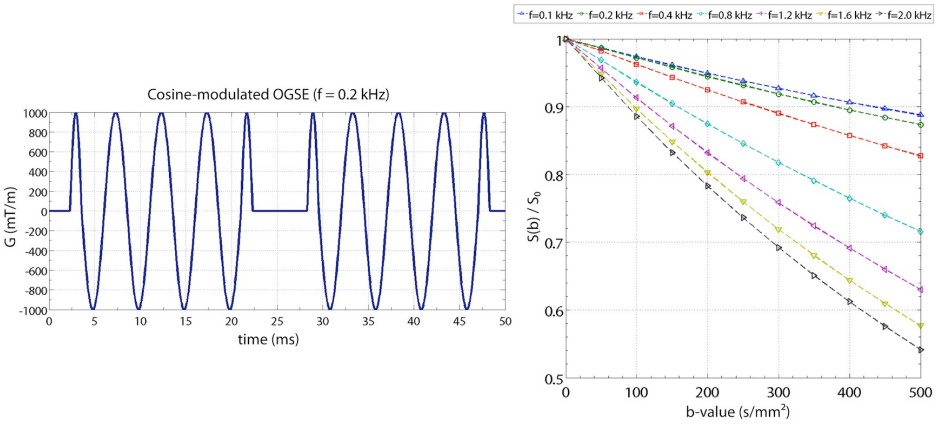

Figure 4.5: DW signal decay of a cosine-modulated OGSE sequence. - (Left) The cosine OGSE at an oscillating frequency (f) of 0.2 kHz. (Right) Plot of DW signal attenuation against b-value at various f.

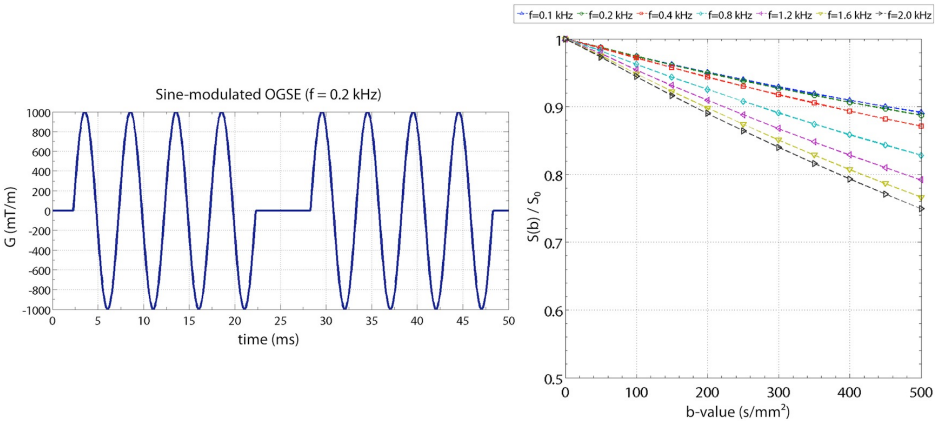

Figure 4.6: DW signal decay of a sine-modulated OGSE sequence. - (Left) The sine OGSE at an oscillating frequency (f) of 0.2 kHz. (Right) Plot of DW signal attenuation against b-value at various f.

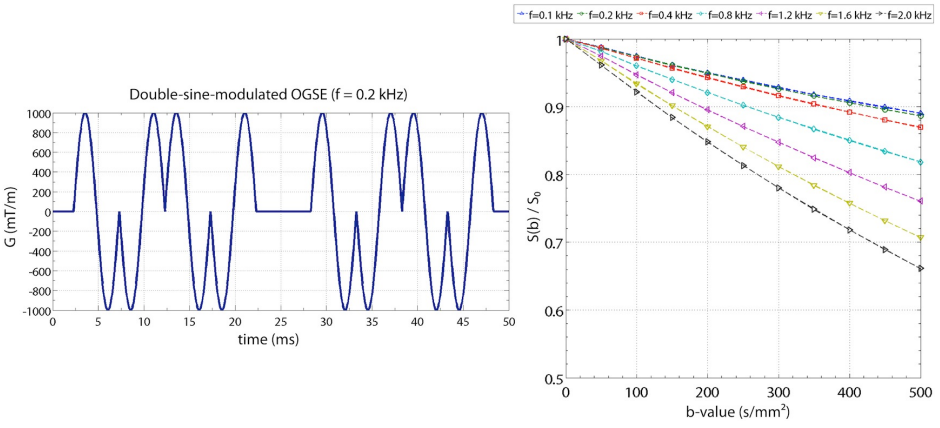

Figure 4.7: DW signal decay of a double-sine-modulated OGSE sequence. - (Left) The double-sine OGSE at an oscillating frequency (f) of 0.2 kHz. (Right) Plot of DW signal attenuation against b-value at various f.

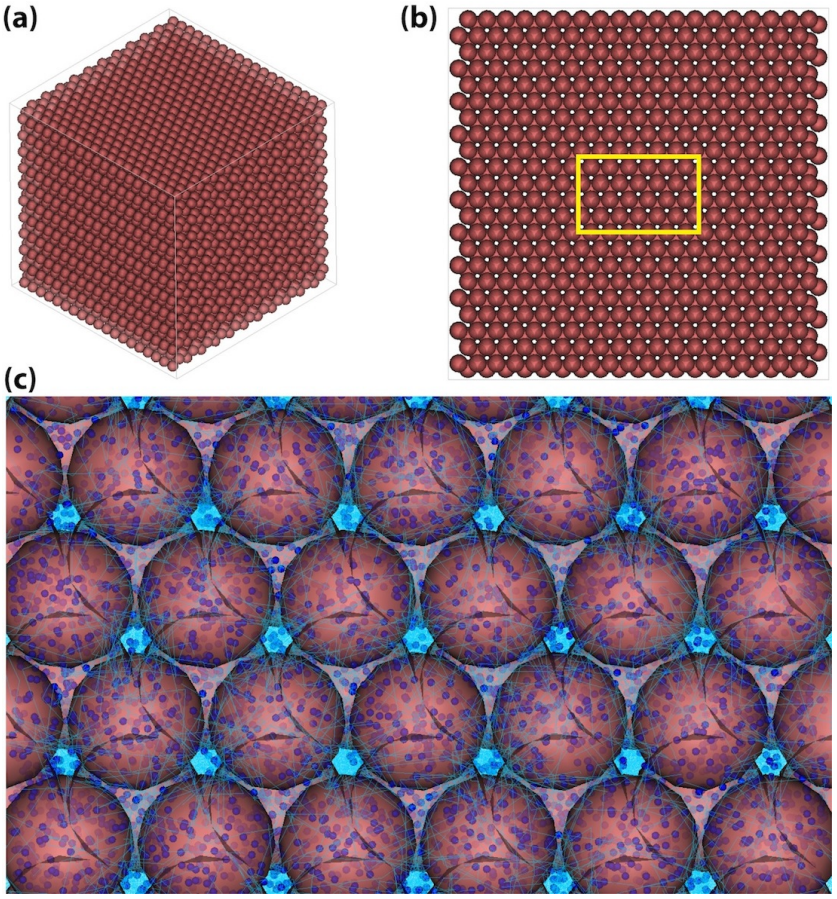

Figure 4.8: DMS simulation of water diffusion in cells. - (a) A global view of the simulation space which contains a hexagonal network of cells modeled by spheres (R = 2.58 μm). (b) A transverse section of (a) illustrating the arrangement of the cells (c) A zoomed region of (b) showing the rendering of cells (colored in pink), diffusing particles (small spheres in deep blue) and their motion trajectories (curves in light blue).

simulation, cells had a specific radius (R) ranging from 2.40 to 2.58 μm and a fixed center spacing of 5.2 μm. Thus, the simulation settings produced a range of ten intracellular volume fractions (i.e. f_i) from 53.27 % to 66.18 %. For each cell size, two separate MC simulations were performed (i.e. totally 20 MC simulations in this section). In the first part, a constant D of 1.2×10^{-3} mm^2/s was assumed for the entire simulation space. In the second part, cell membranes' properties were characterized using the biphasic water diffusion model (see Fig. 2.5) that represented the slow diffusion pool (D_{slow} = 0.4×10^{-3} mm^2/s) by a membrane-bound layer. The region outside the slow-diffusion layer was modeled as a fast diffusion pool (D_{fast} = 1.2×10^{-3} mm^2/s). The choices of the diffusivities (D, D_{slow}, D_{fast}) were based on the values proposed in [Le Bihan (2007)]. The global parameters used across the two MC simulations were: $N_p = 10^6$, N_I = 15,500, and t_s = 5 μs resulting in the RMS distances of 0.19 and 0.11 μm for the D_{fast} and D_{slow}, respectively. Here we assumed that the cells were impermeable and the thickness of the slow-diffusion membrane layer

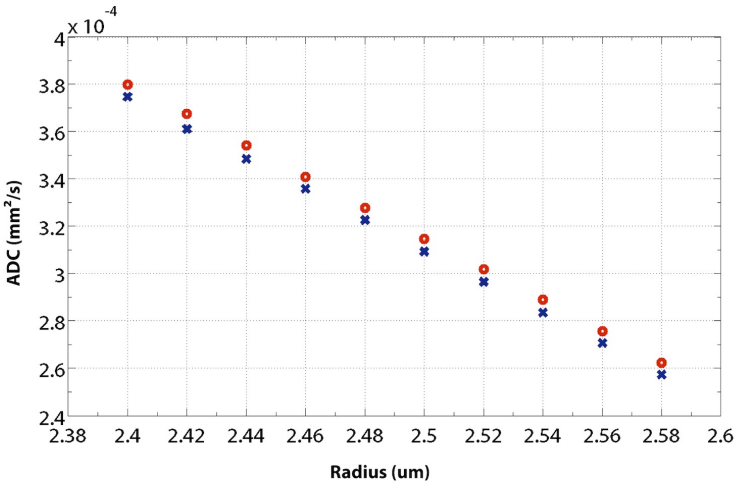

Figure 4.9: Reduction of ADC following cell swelling and polar membrane layer. - The ADC estimated from DT model for the case of constant diffusivity (red circle) and two-pool diffusion model (blue cross).

was 40 nm on each side of the cell membrane. This is because that the model of water layer was not only the bilayer membrane with phospholipids and proteins (∼10 nm), the structuring effect of cell membranes could be reinforced by the relatively thick and rigid matrix which extended a few tens of nanometres on both sides of the membrane: the glycocalyx on the outside and the cytoskeleton on the inside [Le Bihan (2007)]. Fig. 4.8 illustrated an example of the MC simulation experiment considered in this section.

For each of the experiment described above, two noise-free synthetic dMRI datasets were collected using a single PGSE sequence. First, DW signal along x-, y-, and z-axis were synthesized at 51 b-values linearly increased from 0 to 5,000 s/mm^2, which were achieved by fixing $\delta/\Delta = 2/70.5$ ms and varying G (SR = 5,000 T/m/s). The normalized diffusion signal attenuation along each axis was then fitted using a biexponential function given by Eq. 2.34 in Chapter 2.6. Then, the mean and standard deviation were calculated for the biexponential parameters derived from the three axes. Second, the HARDI datasets were synthesized using a single shell q-space sampling scheme of 80 gradient orientations at a b-value of 1,000 s/mm^2, where $\delta/\Delta = 21/27$ ms, $G = 40$ mT/m, and $SR = 200$ T/m/s. The DT reconstruction was performed to estimate the ADC.

4.3.2 Results

Fig. 4.9 showed that the ADC decreased when the cell size increased. As expected, the implementation of a two-pool diffusion model resulted in a lower ADC. Table 4.1 and 4.2 summarized the results of biexponential fitting parameters. For both cases, we found that when the cell size became larger, F_f decreased continuously. An opposite trend was observed for F_s following the

Table 4.1: Biexponential fitting parameters (mean (standard deviation)) for the case of constant diffusivity.

R (μm)	2.40	2.42	2.44	2.46	2.48	2.50	2.52	2.54	2.56	2.58
F_f	0.5196 (0.0017)	0.5054 (0.0009)	0.4929 (0.0021)	0.4805 (0.0012)	0.4653 (0.0004)	0.4537 (0.0016)	0.4383 (0.0014)	0.4243 (0.0024)	0.4094 (0.0011)	0.3960 (0.0014)
D_f	0.9333 (0.0194)	0.9304 (0.0237)	0.9195 (0.0240)	0.9097 (0.0294)	0.9053 (0.0299)	0.8933 (0.0306)	0.8901 (0.0322)	0.8809 (0.0337)	0.8697 (0.0383)	0.8594 (0.0442)
F_s	0.4810 (0.0017)	4.4952 (0.0009)	0.5076 (0.0021)	0.5201 (0.0013)	0.5353 (0.0003)	0.5468 (0.0016)	0.5623 (0.0014)	0.5763 (0.0024)	0.5913 (0.0011)	0.6047 (0.0014)
D_s	0.0083 (0.0005)	0.0089 (0.0003)	0.0090 (0.0009)	0.0092 (0.0004)	0.0100 (0.0001)	0.0096 (0.0003)	0.0102 (0.0004)	0.0105 (0.0005)	0.0109 (0.0003)	0.0109 (0.0003)

Unit for diffusivity: 10^{-3} mm^2/s

Table 4.2: Biexponential fitting parameters (mean (standard deviation)) for the case of two-pool diffusion model.

R (μm)	2.40	2.42	2.44	2.46	2.48	2.50	2.52	2.54	2.56	2.58
F_f	0.5183 (0.0008)	0.5063 (0.0010)	0.4919 (0.0022)	0.4812 (0.0011)	0.4660 (0.0013)	0.4526 (0.0005)	0.4388 (0.0024)	0.4246 (0.0022)	0.4095 (0.0009)	0.3962 (0.0019)
D_f	0.9151 (0.0209)	0.9056 (0.0227)	0.9005 (0.0242)	0.8899 (0.0285)	0.8835 (0.0261)	0.8743 (0.0314)	0.8676 (0.0313)	0.8558 (0.0321)	0.8465 (0.0391)	0.8333 (0.0427)
F_s	0.4823 (0.0008)	0.4943 (0.0009)	0.5087 (0.0021)	0.5194 (0.0011)	0.5346 (0.0013)	0.5481 (0.0006)	0.5618 (0.0023)	0.5761 (0.0022)	0.5912 (0.0009)	0.6045 (0.0018)
D_s	0.0089 (0.0003)	0.0091 (0.0004)	0.0096 (0.0008)	0.0093 (0.0003)	0.0101 (0.0003)	0.0100 (0.0002)	0.0103 (0.0005)	0.0107 (0.0005)	0.0110 (0.0004)	0.0110 (0.0005)

Unit for diffusivity: 10^{-3} mm^2/s

cell swelling. Although a decrease in D_f and an increase in D_s were observed when the cell size increased, the values did not change much.

4.3.3 Discussion

For the experiments on cell swelling and two-pool diffusion model, overall we observed and verified that cell swelling led to a drop of ADC, which was consistent with the previous findings on acute ischemic stroke [Moseley et al. (1990b)] and neuronal activation [Le Bihan et al. (2006); Le Bihan (2007); Flint et al. (2009)]. Based on the results obtained from the biexponential analysis, we found that D_f and D_s did not alter significantly following cell swelling. The results implied that the variation of volume fractions F_f and F_s mainly drove the variations of diffusion signal attenuation.

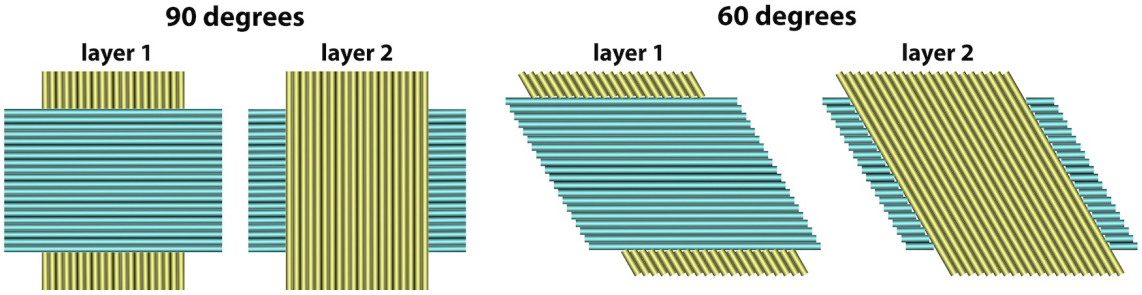

Figure 4.10: Construction of crossing fibres by DMS - Each layer was build by two fibre directions. Layer 1 and layer 2 overlapped each other to form crossing fibres, and different densities between two populations can be obtained by controlling the number of overlapping.

Note that although we could already simulate the effect of polar membrane layer, the RMS distance that we used (0.19 and 0.11 μm) was larger than the layer thickness of 0.04 μm assumed in the literature [Le Bihan (2007)]. This may affect the results, especially when the diffusing particles are closed to the cell membranes [Regan and Kuchel (2002)], and it will require a smaller t_s to clarify this issue. Works are undergoing to introduce more factors such as the membrane permeability to perform more complex and realistic simulations.

4.4 Diffusion Reconstruction Model

In this section, we demonstrated that DMS is able to provide the ground-truth virtual fibre configurations and the associated synthetic dMRI dataset for assessing the diffusion reconstruction algorithms.

4.4.1 DMS Experimental Design

We used DMS to create two fibre bundles crossing at 90 and 60 degrees. Fig. 4.10 showed the basic 'layers' to construct crossing fibres. For each case, we controlled the number of layers to make the proportion between the two fibre directions equal to 1:1 and 1:2. The parameters for MC simulations were: simulation space = 300×300×200 μm^3 for 90-degree crossing and 350×240×200 μm^3 for 60-degree crossing; the fibre diameter was fixed at 8 μm; $N_x \times N_y \times N_z$ = 100×100×100; $N_p = 2 \times 10^6$; N_I = 8,000; t_s = 10 μs; $D = 2/3 \times 10^{-4}$ mm^2/s (i.e. the value closed to the axial diffusivity of WM fibre). HARDI datasets were synthesized using a grid volume that produced a single slice image with an inplane resolution of 10×10 μm^2. A PGSE sequence was used with G = 40 mT/m and SR = 200 T/m/s, and two b-values at 1,500 and 2,500 s/mm^2 were obtained by tuning δ/Δ to 24.5/30.5 ms and 29.4/35.4 ms, respectively. A single shell q-space sampling scheme containing 65 gradient orientations was used. Rician noise was added to the synthetic DWIs to

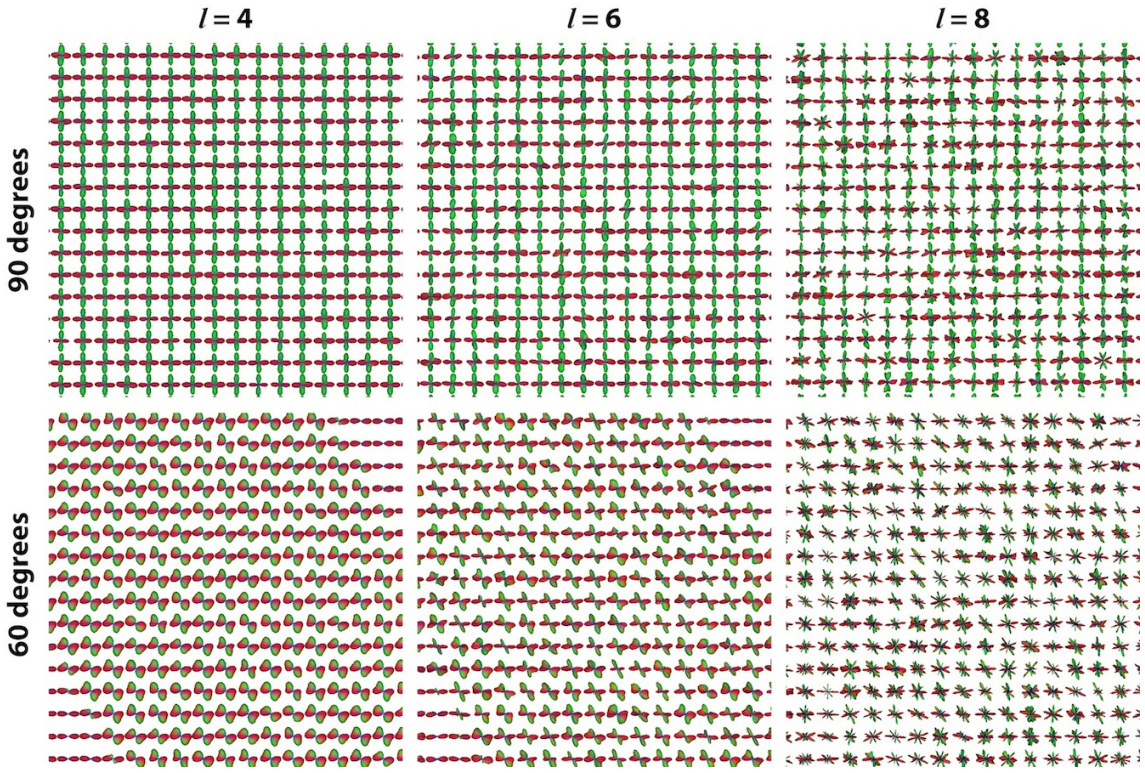

Figure 4.11: Effect of spherical harmonic order on SDT-fODF. - SDT-fODF were reconstructed for 90 and 60-degree crossing fibres using the harmonic order l of 4, 6, and 8 (at b = 2,500 s/mm^2 and SNR = 20).

produce three SNRs of 10, 20, and 40 measured on the non-diffusion-weighted image. Therefore, in total 12 synthetic dMRI datasets were generated (2 crossing angles × 2 b-values × 3 SNRs). Note that the simulations described above reflected what can be achieved on a clinical MRI system.

Synthetic dMRI data was analyzed using (i) the DT model to reconstruct the FA map [Basser et al. (1994b)] and (ii) the sharpening deconvolution transform (SDT) to reconstruct the fibre orientation distribution function (fODF) [Descoteaux et al. (2009)]. For the SDT analyses, first we used the spherical harmonic order (l) of 4, 6, and 8 with the regularization factor being fixed at 0.006 to assess the results of fODF. After that, we applied the optimal l to study the effect of b-value, SNR, and fibre density distribution. The results of fODF fields were color-coded according to their orientations (red: left-right; green: anterior-posterior; green: inferior-superior).

4.4.2 Results

Fig. 4.11 showed that at b-value of 2,500 s/mm^2 and SNR of 20, using $l = 4$ was able to resolve 90-degree crossing but became ambiguous for the 60-degree case. Using $l = 6$ successfully differentiated both 90 and 60-degree crossing fibres. Using $l = 8$ produced many false positive peaks of fODF

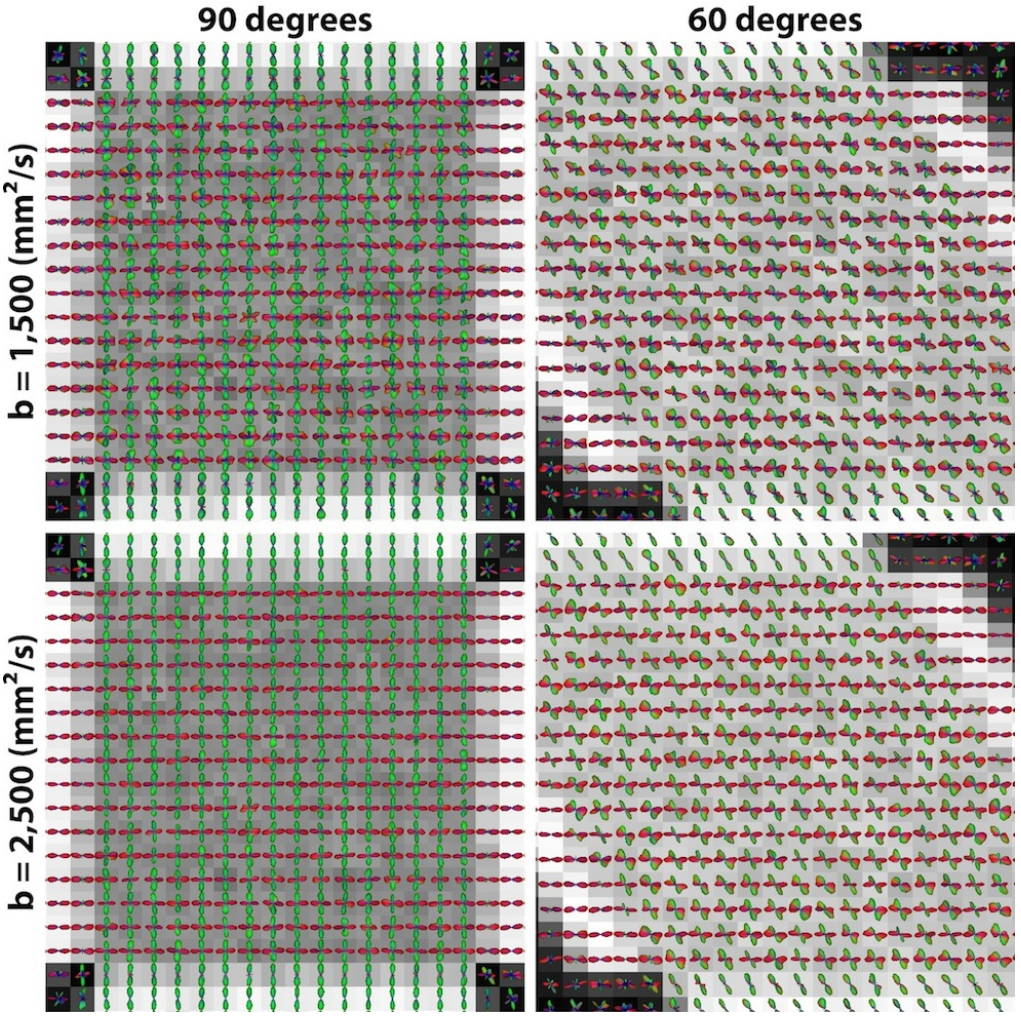

Figure 4.12: Effect of b-value on fODF estimation. - The fODFs were reconstructed using SDT for the 90- and 60-degree crossing fibres at b-values of 1,500 and 2,500 s/mm^2 (SNR = 20 on the null image).

for both cases, which was not suitable for fibre orientation estimation. The results suggested that $l = 6$ was the optimal setting for the SDT method at b-value = 2,500 s/mm^2 for our crossing fibre data. Hence, the remaining data were all analyzed using $l = 6$.

Fig. 4.12 showed the dependence of fODF estimation on b-value for the 90- and 60-degree crossing fibres. The SNR was 20 on the null image for both datasets. At a b-value of 1,500 s/mm^2, the two distinct fibre orientations were clearly resolved by SDT for the 90-degree crossing but were less evident for the 60-degree crossing in some voxels. At a b-value of 2,500 s/mm^2, the SDT-fODF became sharp enough to distinguish both 90- and 60-degree crossing fibres.

Fig. 4.13 demonstrated the impact of noise level on fODF estimation, showing the results at a b-value of 1,500 s/mm^2. As expected, the results of fODFs were more homogenous at a higher SNR. At a SNR of 10, although the two directions were still differentiated by SDT-fODF in some

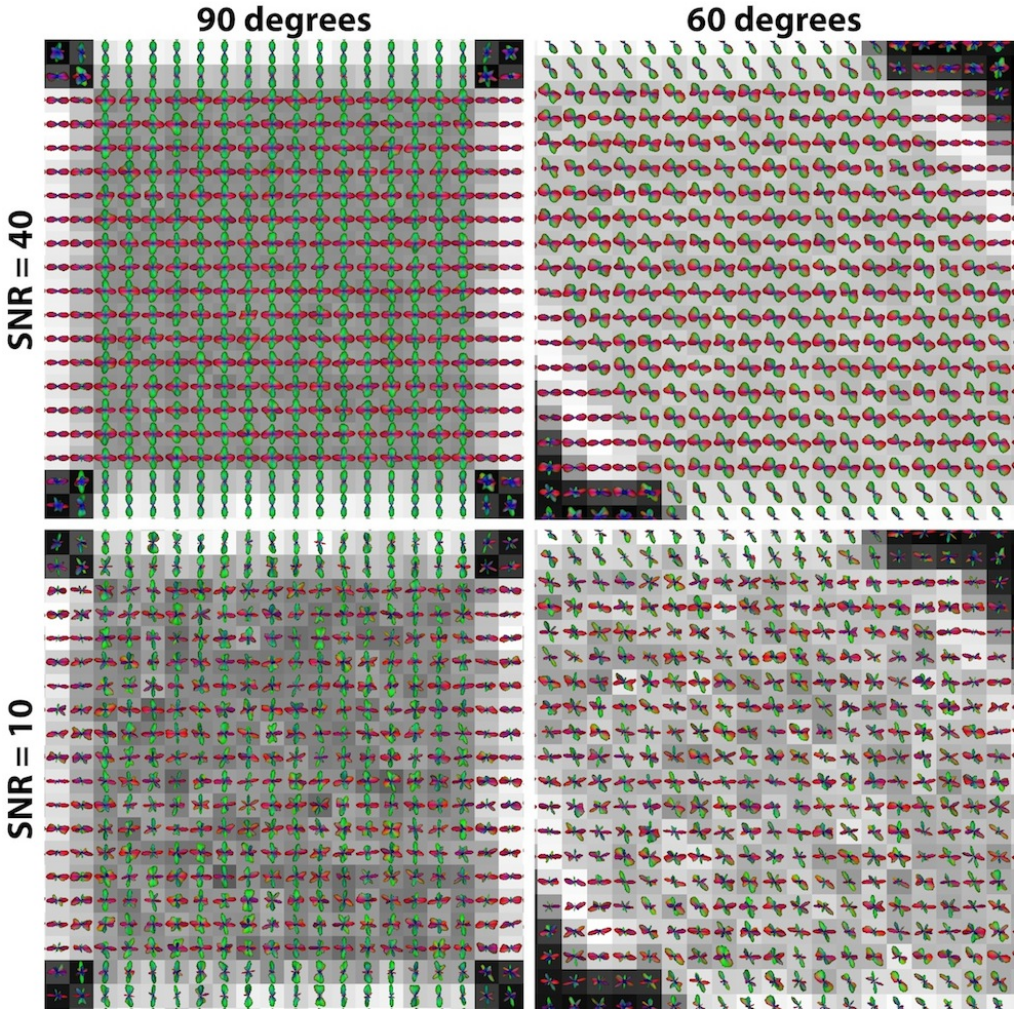

Figure 4.13: Effect of SNR on fODF estimation. - The fODFs were reconstructed using SDT for the 90- and 60-degree crossing fibres at SNRs of 40 and 10 (b-value = 1,500 s/mm^2).

voxels for both cases, they were deviated from the ground-truth directions.

Fig. 4.14 showed the results of fibre orientations mapping where the density ratio of the two fibre bundles was 2:1 and SNR was 20. For both cases, the magnitude of fODFs along the direction of fewer fibre number were lower than those in the other direction. For the 90-degree crossing, the two distinct directions were still resolvable using SDT, at both 1,500 and 2,500 s/mm^2. For the 60-degree crossing, the direction of the fewer fibres were not identifiable in most voxels, and only the horizontal direction (colored in red) was clearly observed.

4.4.3 Discussion

We demonstrated how DMS could provide the ground-truth datasets and apply to assess the diffusion reconstruction algorithms. The example datasets of 90- and 60-degree fibre crossing were

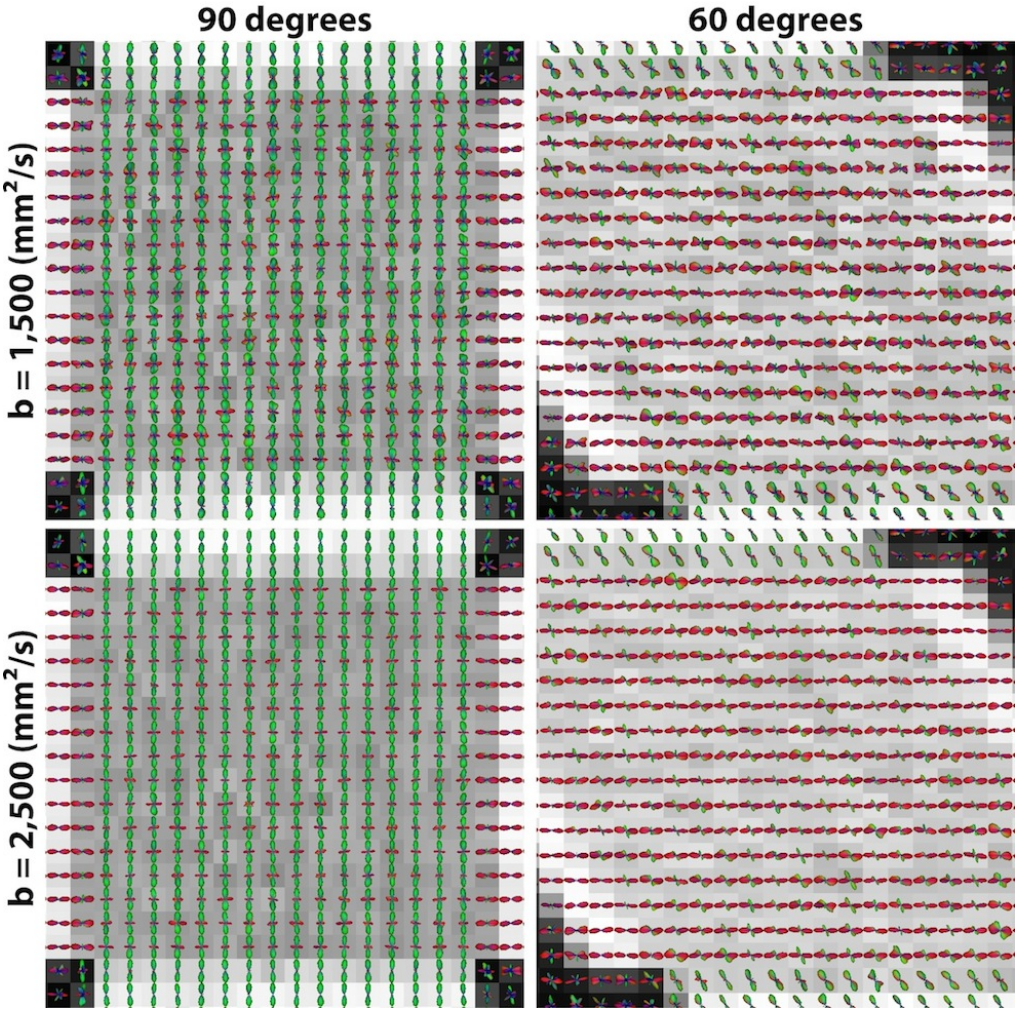

Figure 4.14: Effect of fibre density on fODF estimation. - The fODFs were reconstructed using SDT for the 90- and 60-degree crossing fibres where the proportion between the two fiber orientations were 2 to 1 (SNR = 20).

applicable to study the dependency of b-value (Fig. 4.12), SNR (Fig. 4.13), and fibre populations (Fig. 4.14). They can be further utilized to optimize the HARDI acquisition protocol and pulse sequence for the purpose of fibre orientation estimation. Although the crossing fibres were only created at two crossing angles and densities, DMS can be used to generate any other fibre configurations (e.g. curving fibres). The dataset is also suitable for comparing and optimizing the diffusion reconstruction models.

It is already well-known that the selection of b-value is crucial as it produces the diffusion orientational contrast that is essential for mapping fibre directions [Cho et al. (2008)]. Although we only evaluated two b-values, it is simple for DMS to synthesize dMRI data at several b-values. Thus, this part will be extended to study the optimal q-space sampling scheme (e.g. a single shell or multiple shells) and b-values for dMRI data acquisition in order to improve the accuracy of fibre

orientation estimation.

The SNR issue is important since the image contrast of dMRI comes from signal attenuation. In addition, a higher b-value is usually preferable due to the sensitivity to diffusion will increase, however, it will also result in a worse SNR. Several noise removal techniques have been proposed to improve the quality of DWIs and the related measures. DMS can be employed to generate DWIs at various SNR levels to assess the performance of the noise correction as well as to help develop novel denoising methods.

4.5 Fibre Tracking Application

In this section, we employed DMS to generate crossing, kissing, and branching WM fibre bundles and then applied to evaluate the performance of fibre-tracking algorithms.

4.5.1 DMS Experimental Design

DMS was utilized to simulate three WM fibre configurations, namely crossing, kissing, and branching fibres, in separate simulation spaces with dimensions of 110×190×150, 110×190×150, and 200×210×185 μm^3, respectively (see Fig. 4.15). Each fibre had a diameter of 5 μm and no permeability. The parameters for the MC simulations were: $N_p = 10^6$, N_I = 8,000, t_s = 10 μs, and D = 2×10^{-3} mm^2/s. We utilized a conventional single PGSE pulse sequence to synthesize HARDI data with the following sequence parameters: G = 40 mT/m, SR = 200 T/m/s, δ = 34.75 ms, Δ = 40.75 ms, TE = 80 ms, and b-value = 4,000 s/mm^2. The parameters were chosen to comply with a clinical MRI system. For each fibre configuration, dMRI images were synthesized using a grid volume that produced a single slice image with an inplane resolution of 5×5 μm^2. A uniform HARDI sampling scheme consisted of 200 unique orientations created by an electrostatic repulsion model [Jones et al. (1999)]. For each fibre configuration, we reconstructed the fODF using the SDT with a spherical harmonic order of 6 and a regularization factor of 0.006 [Descoteaux et al. (2009)]. In addition, DT analysis was performed to obtain the FA map, which was utilized to create mask images for fibre tracking. Both deterministic and probabilistic fibre tractography were obtained via a streamline fibre-tracking algorithm, with a forward step increment of 1.25 μm (i.e. one-fourth of the inplane resolution), an aperture angle of 30°, and 10 seeds per voxel [Basser et al. (2000); Poupon et al. (2000); Perrin et al. (2005a)]. Note that although the anisotropic voxel dimension was used for fibre tracking, it did not have any severe side effect on the results of fibre tractography presented in this section. This was due to that the organization of the fibre geometries were all placed on the plane of isotropic resolution, and thus the fibre-tracking evolution should not

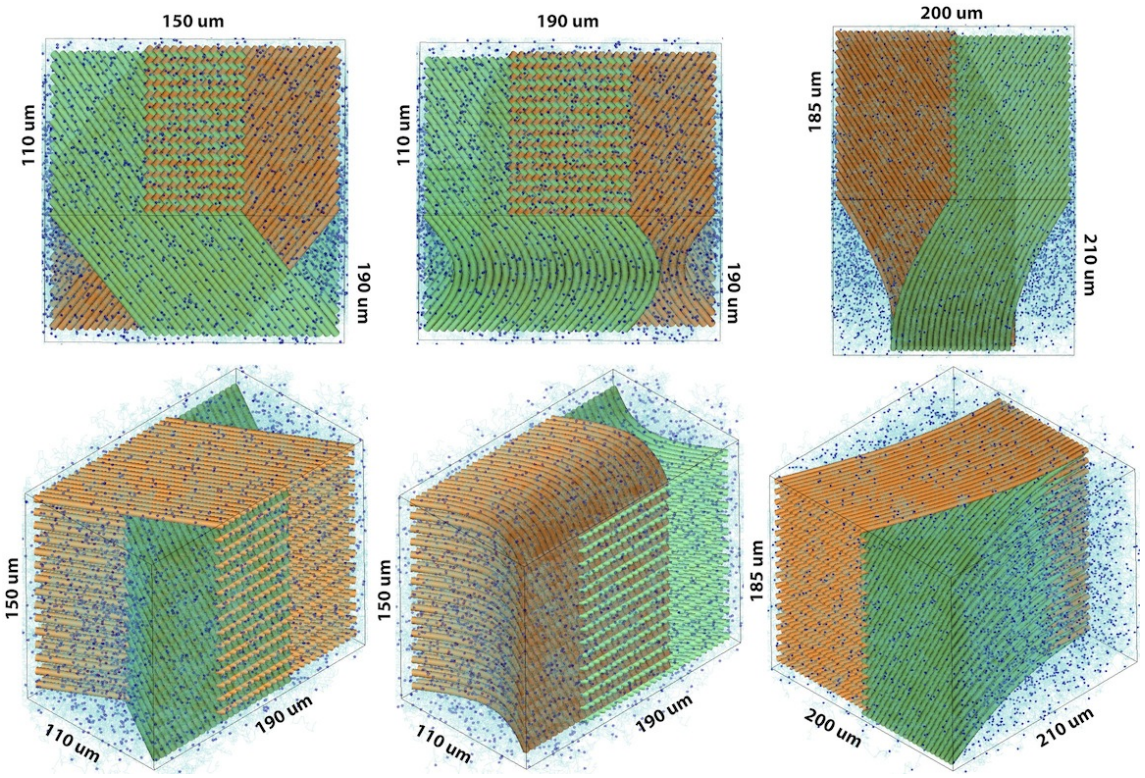

Figure 4.15: Simulated fibre configurations: crossing, kissing, and branching fibres - DMS was utilized to create three fibre configurations typically observed in human brains. Left column: crossing fibres; middle column: kissing fibres; right column: branching fibres. For each case, two networks of fibres, colored in green and orange, were arranged in an interleaved fashion. A subset of diffusing particles and their motion trajectories were illustrated by dark blue spheres and light blue curves.

be affected by the anisotropic scale along the direction perpendicular to the plane containing the fibres. Likewise, this was also the same case for the diffusion local reconstruction described in the previous section.

4.5.2 Results

Fig. 4.16 showed the results of fODF and probabilistic tractography for crossing and kissing fibre tracts. SDT gave different fODF patterns in the crossing and kissing fibres, and the streamline probabilistic fibre tractography generated based on SDF-fODF can successfully differentiate fibres pathways. Fig. 4.17 illustrated the results of fibre tracking using deterministic and probabilistic methods. The deterministic fibre tractography resulted in ambiguous fibre tracts in the region where the fibre tracts diverted into two different directions. The probabilistic fibre tractography showed better correspondence with the simulated fibre configuration (i.e. the ground truth).

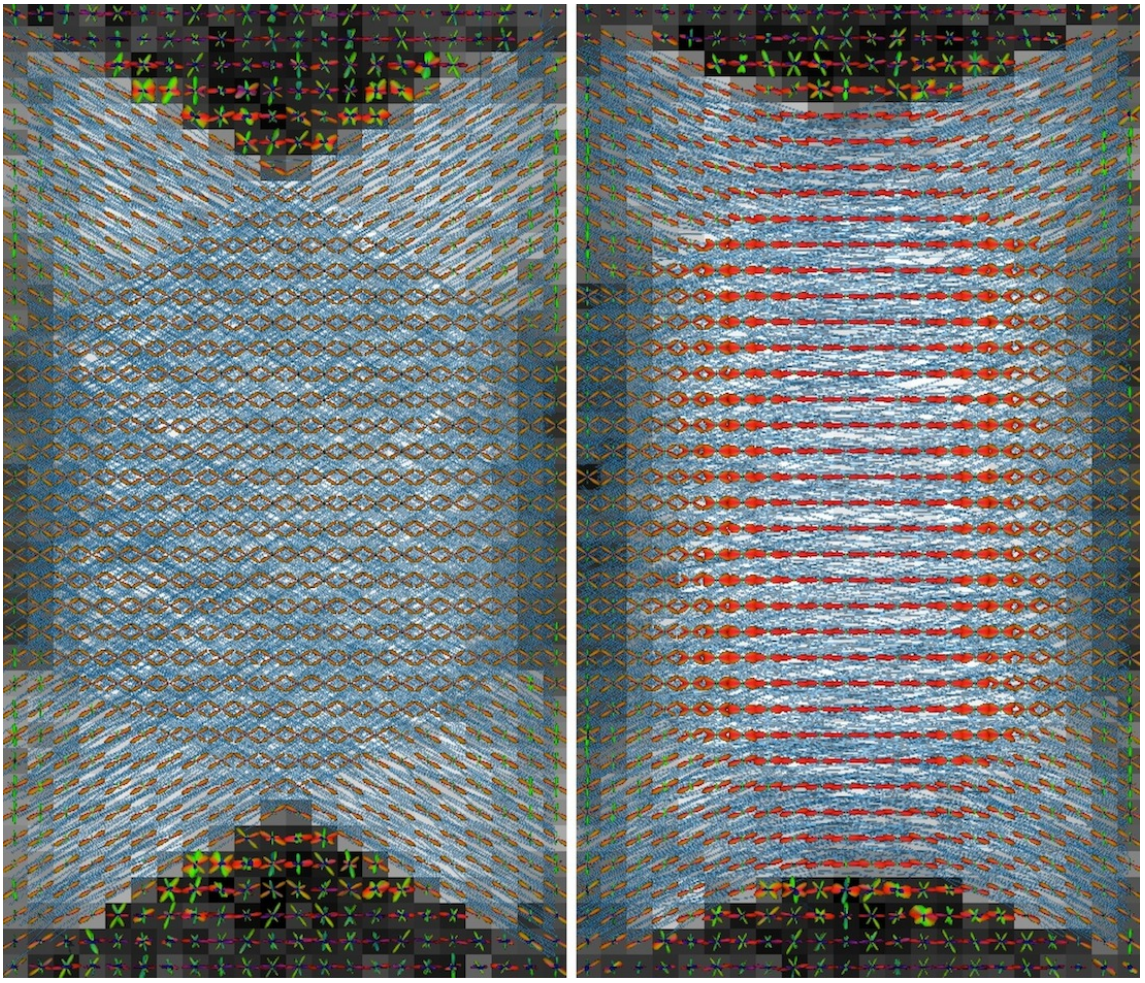

Figure 4.16: The SDT-fODF and probabilistic fibre tractography. - The sharpening deconvolution transform and the streamline probabilistic fibre-tracking algorithm were performed on the synthetic dMRI datasets of crossing (left) and kissing (right) fibres. The fODF were color-coded depending on orientations (red: left-right, green: top-down, blue: inferior-superior). Fibre tractography was represented by cylinders colored in blue. Both of the fODF and tractography were overlapped on the FA images.

4.5.3 Discussion

The ability of dMRI in noninvasively mapping fibre directions of human brain provides opportunities to study anatomical brain connectivity. To produce a reliable fibre tractography, there are two essential steps. The first step is to accurately estimate local fibre orientations using an adequate diffusion reconstruction algorithm, and the second step is to implement a robust fibre tracking algorithm. Thus, assessment and validation of diffusion local modeling and fibre tracking algorithms are important, and these evaluations require an appropriate model to serve as a 'gold standard.'

A biological tissue model that utilizes neuronal tracers, such as manganese-enhanced MRI,

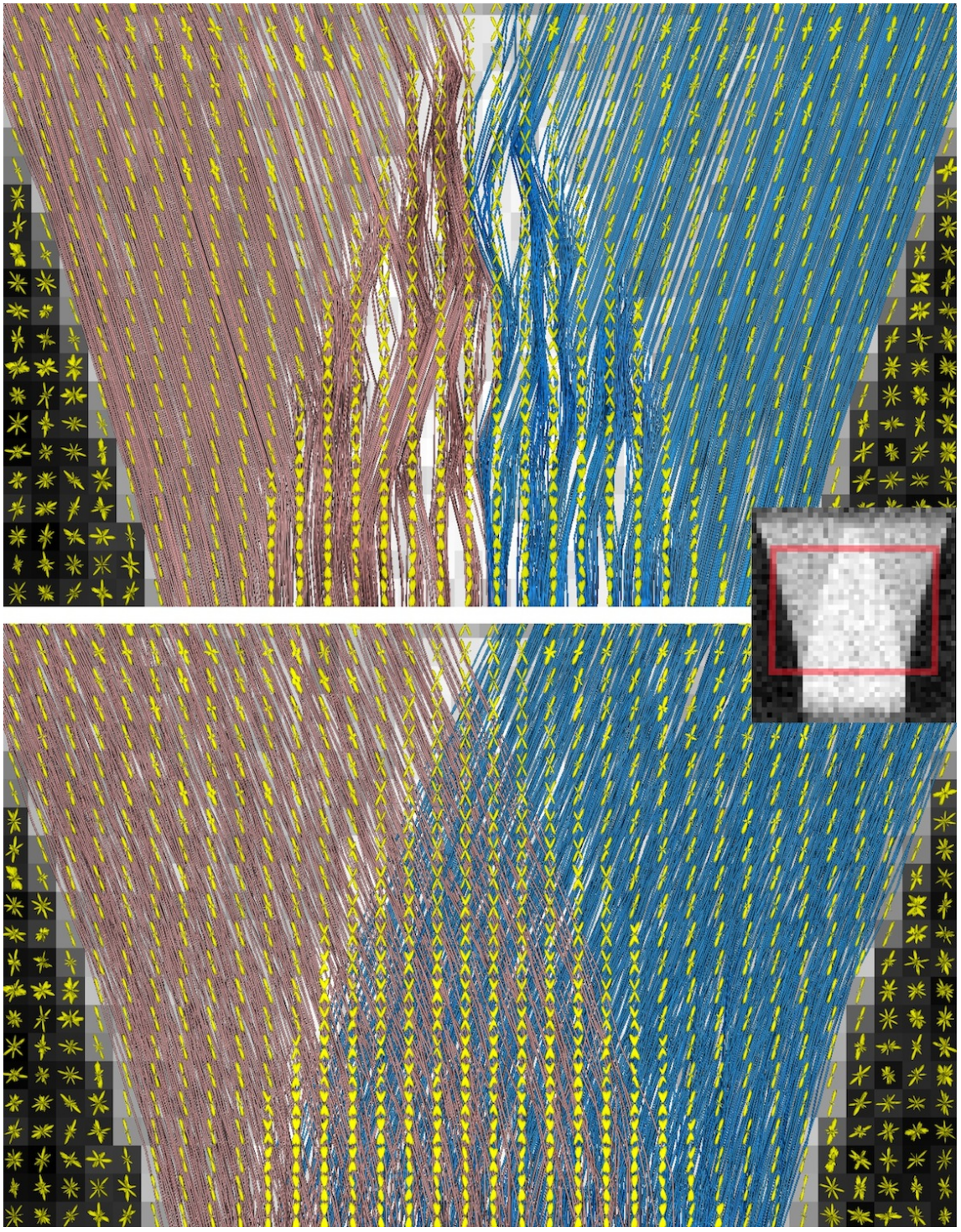

Figure 4.17: Differences between deterministic and probabilistic fibre tratography. - Top row: fibre tracking using a deterministic approach. Bottom row: fibre tracking using a probabilistic approach. fODF were colored in yellow. Center: the location of fibre tractography on FA map.

has been adopted to assess the validity of diffusion reconstruction model and fibre tractography [Lin et al. (2001, 2003)]. The advantage of this technique is that it provides a realistic tissue environment, however, it is less feasible to tune the structural or geometric parameters (e.g. fibre curvature). Furthermore, WM structures are less complex in animal models, which cannot capture all of the fibre configurations that exist in human brains, and thus it may not be sufficient to evaluate the inherent limits of diffusion local models and fibre-tracking algorithms.

A physical phantom is able to provide ground-truth dMRI datasets acquired with a practical MR experimental setting, meanwhile, it is more flexible than a biological tissue model in terms of geometry design. However, it loses the characteristics of biological tissues, such as membrane permeability and local viscosity. Several elaborate physical phantoms have been developed in the community and can be broadly categorized into two types: the hollow capillary [Cho et al. (2008); Lin et al. (2001, 2003); Shemesh et al. (2009a); Tournier et al. (2008)] and the synthetic fibre [Fillard et al. (2011); Fieremans et al. (2008b,a); Perrin et al. (2005b); Poupon et al. (2008)]. The advantage of the former is that it has a diameter closed to the scale of axonal fibres (10 μm) and is able to capture the nature of intra- and extra-axonl diffusion, however, it is much less feasible to manufacture complex configurations (e.g. bending fibres). On the contrary, the latter is highly flexible to construct curving structures similar to WM fibres, whereas it has a greater size in diameter ($\sim$20 μm) and is limited to simulate the extra-axonal compartment.

Numerical simulation have been typically chosen to generate synthetic DW datasets for the assessment of diffusion local models and fibre-tracking algorithms [Tuch (2004); Hess et al. (2006); Close et al. (2009); Descoteaux et al. (2009)], however, most of the numerical simulations typically rely on a number of assumptions on tissue models and pulse sequences. The Gaussian mixture model, for example, is commonly utilized to generate the DW signal for each compartment. Although the tensor model provides a good approximation, the Gaussian assumption for the free diffusion is not sufficient to model diffusion anisotropy observed in vivo tissues, which is generally acknowledged to result from restrictions and hindrances to the free movements of water molecules [Assaf et al. (2004)]. Furthermore, the underpinning mechanism of water diffusion in neural tissues is actually even more complicated when the cell-membrane properties are considered [Le Bihan (2007)].

A MC simulation system has the capacity to simulate biological characteristics, and thus it is feasible to evaluate diffusion models and fibre-tracking algorithms at different level of complexity (e.g. mixture fibre radii or cell membrane permeability). In addition, it removes most of the assumptions inherently required by the numerical simulations. Although there are still several parts to improve (e.g. modeling typical imaging artifacts such as cross-terms and eddy current),

DMS is already applicable to simulate various configurations that can be found in WM structures of human brains according to our simulation results.

4.6 Conclusion

DMS is general and flexible to synthesize MR data for arbitrary imaging environment and conditions. The simulation tool is already applicable to address several issues in dMRI. DMS provides a platform for the development, validation, and optimization of diffusion MRI modeling and methodology, and we believe that it can be an essential tool for understanding of diffusion mechanism.

4.7 Acknowledgments

Many thanks to Pamela Guevara for the helpful suggestions on the fibre tractography.

Part III

APPLICATIONS

Chapter 5

The Effect of Finite Diffusion Gradient Pulse Duration on Fibre Orientation Estimation in Diffusion MRI

Contents

5.1 Introduction

In Chapter 2.3.2, we have reviewed that in the q-space formalism [Callaghan (1993)], the probability density function (PDF) of the displacement of water molecules can be obtained by performing the Fourier transform (FT) of the DW signal acquired as a function of the wave vector q (Eq. (2.22) & (2.23)). The displacement PDF can be utilized to estimate the dimensions of microstructures and interpret tissue states [Cohen and Assaf (2002)], and recent studies have demonstrated the potential of q-space diffusion MRI in measuring axonal diameters [Alexander et al. (2010); Assaf et al. (2008); Ong et al. (2008)]. However, the essential principle of the q-space technique is only valid under the short gradient pulse (SGP) condition [Callaghan (1993)], which means that a very strong gradient system is demanded in order to achieve sufficient resolution of the spin displacement, i.e. to obtain a sufficiently high q-value. On current clinical MR systems, high q or b-value requirement can be only achieved by the prolongation of δ due to gradient intensity constraints. Usually, δ is close to Δ in order to minimize T_2-decay and to get better SNR in the DW images. However this practice is detrimental for obtaining quantitative q-space measurements, resulting in an underestimation of the actual compartment size [Bar-Shir et al. (2008); Caprihan et al. (1996); Mitra and Halperin (1995); King et al. (1997)]. The effects of finite gradient pulse widths on the estimated displacement PDF have been well described in literature using small animal systems with dedicated gradient hardware to attain the essential requirement of the SGP approximation [Bar-Shir et al. (2008); Mitra and Halperin (1995); King et al. (1997); Lätt et al. (2007); Lori et al. (2003)].

During the last 25 year, dMRI has become a valuable tool for the study of the human CNS. Of particular interest is its potential for non-invasively mapping the pathways of neuronal fibre bundles in the living brain, as it enables the possibility of inferring neuronal connectivity between brain regions using fibre-tracking algorithms [Basser et al. (2000); Conturo et al. (1999); Mori and van Zijl (2002)]. The reliability of brain connectivity information depends on the accuracy of the fibre orientation estimates within each imaging voxel, which in turn is dependent on the fibre orientation reconstruction method, the particular diffusion imaging parameters used, and the quality of DW images. Several approaches have been developed for estimating fibre orientations and DTI is the first and the most common method, which involves the application of a relatively low diffusion weighting (i.e. b-value) to characterize diffusion anisotropy and infer the principal orientation of the white matter tracts within each imaging voxel [Basser et al. (1994a,b); Basser and Pierpaoli (1996)]. As described in Chapter 2.4.3, a number of methods have been proposed to enable resolution of multiple fibre orientations within a voxel. Many of these methods are based

on the q-space theory. Some of these methods rely on full 3D sampling of q-space using very large b-values in order to perform the required 3D FT [Assaf and Basser (2005); Wedeen et al. (2005); Wu and Alexander (2007)]. Other methods, while still based on q-space theory, make certain simplifying assumptions to allow the 3D FT to be performed using a reduced dataset, and operate on the less demanding HARDI acquisition strategy, with moderate to high b-values [Ozarslan et al. (2006); Tuch (2004); Jansons and Alexander (2003); Descoteaux et al. (2007); Hess et al. (2006)]. Other methods have also been proposed based on a mixture model rather than the q-space formalism [Assaf et al. (2004); Behrens et al. (2007); Hosey et al. (2005, 2008); Tournier et al. (2004, 2007)].

Although the above q-space approaches can be utilized to successfully estimate complex fibre directions, the failure to satisfy the SGP approximation has been a recurrent criticism. However, the effect of a long δ on the DW signal and the angular accuracy of the estimated orientation have not been fully characterized. It has been suggested that using a finite δ may enhance the MR signal contrast between DW gradient orientations [Hall and Alexander (2006); Lin et al. (2003)], whereas the underlying mechanism requires further clarification. In this chapter, we show that, while being a deficiency in q-space applications to determine spin displacement, the application of a longer δ is actually beneficial for resolving fibre orientations, as it enhances both the DW signal and the contrast between the DW encoding directions. We investigate the relationship between δ and the DW signal measured as a function of orientation for single fibre bundles under the same effective diffusion time ($\Delta_e = \Delta - \delta/3$) [Blees (1994); Callaghan (1993); Callaghan et al. (1999)] and TE for a given b-value, using DMS simulations and two experimental phantoms, one consisting of water capillaries, and the other consisting of an ex-vivo nerve preparation. In addition, we performed QBI [Tuch (2004)] on both simulated (DMS) and experimental (water capillaries) crossing fibres to demonstrate the benefits of using a long δ.

5.2 Hypothesis

Under the SGP approximation, the labelling and unlabelling of the spins is assumed to take place instantaneously. The displacement measured in q-space then corresponds to the distance from the initial position of the spin at the first DW gradient pulse to its final position at the second DW gradient pulse (Figs. 5.1(a) & 5.2(a)). On the contrary, with a finite δ, the particle is labelled with a position given by the centre of mass of its path during the application of the gradient pulse [Mitra and Halperin (1995)]. Therefore, the effective displacement that is actually estimated corresponds to the distance between the spin's average position during the first DW pulse and its average position during the second DW pulse (Figs. 5.1(b) & 5.2(b)). In restricted geometries, the average position of a spin during each DW pulse will tend towards the centroid of the restricted

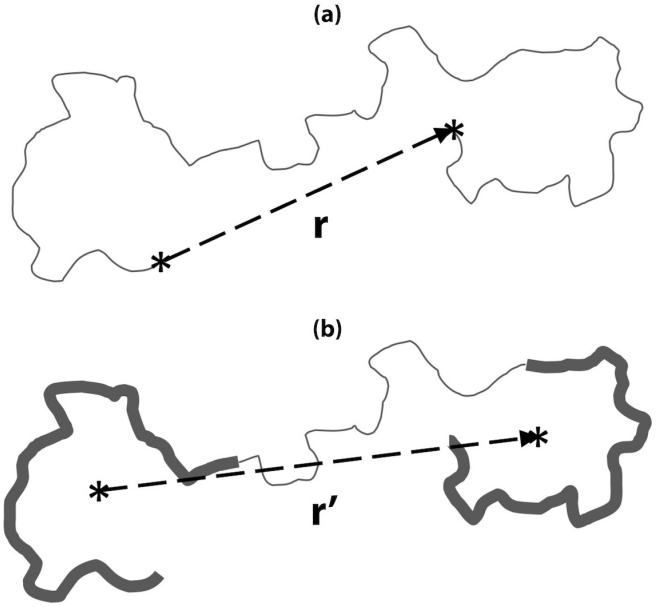

Figure 5.1: Spin trajectory in a free diffusion environment. - The centre of mass position of the spin during each gradient pulse is indicated by the symbol "⋆". (a) For a short δ, the encoding of the spin is assumed to occur immediately and gives a spin displacement, r. (b) For a long δ, the spin is labelled at the position of the centroid of its path during the application of the diffusion gradient pulse, as shown in bold trajectories [Mitra and Halperin (1995)]. The resultant displacement r' will be closed to r in a free diffusion environment and thus similar diffusion signal decay will be observed.

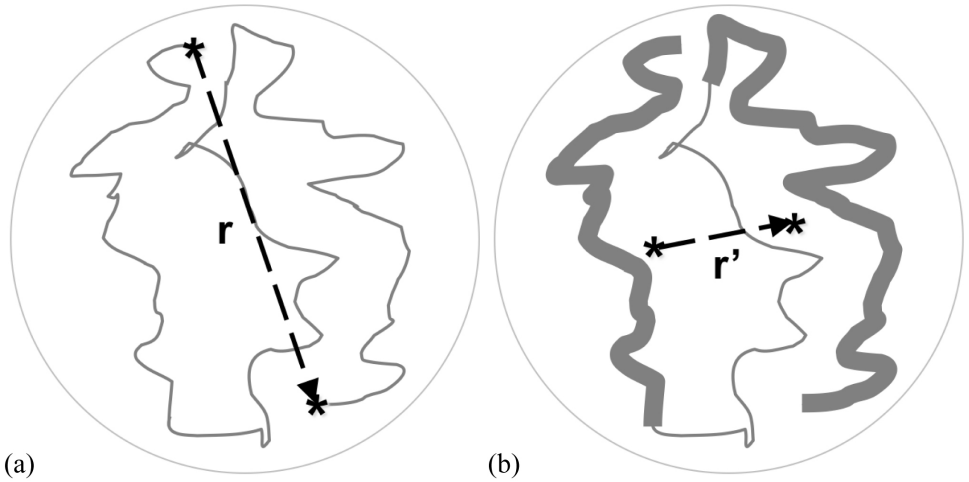

Figure 5.2: Spin trajectory in a restricted environment. - The centre of mass position of the spin during each gradient pulse is indicated by the symbol "⋆". (a) For short a δ, the encoding of the spin is assumed to occur immediately, which results in larger spin displacement, as denote by r. (b) For a long δ, the spin is labelled at the position of the centroid of its path during the application of the diffusion gradient pulse, as shown in bold trajectories [Mitra and Halperin (1995)]. The resultant displacement r' is decreased in a restricted environment and thus less signal decay will be observed.

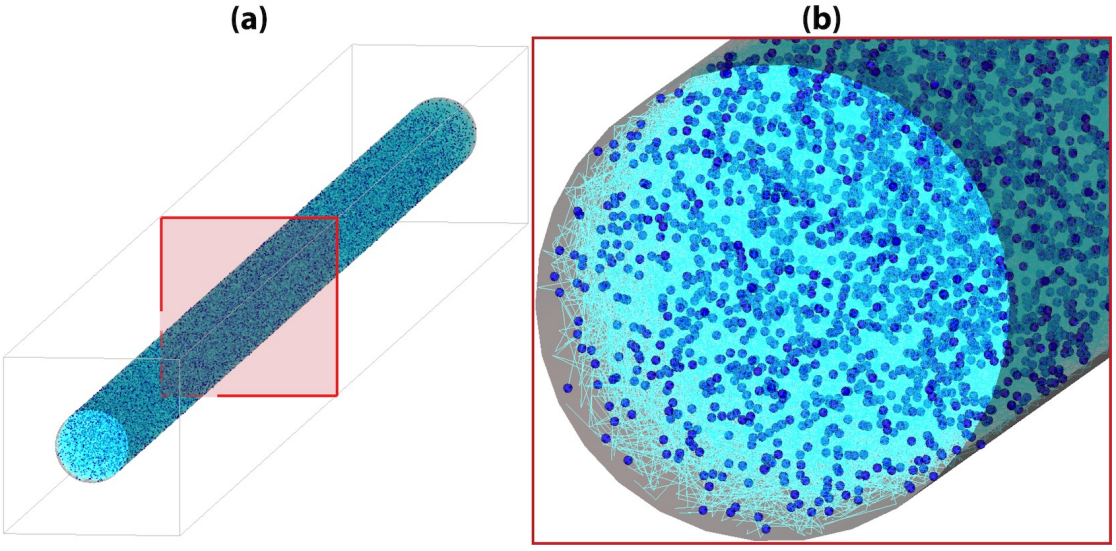

Figure 5.3: DMS: Single fibre model. - (a) The single restricted fibre model considered in the simulations of DMS. (b) A cross section of (a) illustrating the fibre geometry, diffusing particles (blue spheres), and their motion trajectories (light blue curves).

compartment (Fig. 5.2(b)). Therefore, the estimated displacement decreases with increasing δ, and in consequence the measured DW signal attenuation is reduced. Over the timescale of the DW experiment, the diffusion in myelinated WM fibres can be approximated as restricted in directions perpendicular to the fibre axis (i.e. the radial direction), and free along the fibre axis (i.e. the axial direction) [Assaf et al. (2004); Assaf and Basser (2005)]. In this case, increased δ should result in reduced tranverse DW signal attenuation, with no change in the axial DW signal. This should therefore improve the contrast between diffusion gradient directions, and also improve the overall SNR of DW images, both of which are actually helpful to estimate fibre orientations.

5.3 Materials and Methods

This hypothesis described above (Chapter 5.2) was tested using single fibre phantoms including DMS MC simulations, an MR water microcapillary phantom model, and excised rat sciatic nerves. Furthermore, we performed QBI [Tuch (2004)] to study the δ effect on fibre orientation mapping using simulated and experimental diffusion phantoms.

5.3.1 DMS Experimental Design

To test our hypothesis that the application of a long δ may be beneficial for fibre orientation estimation, we began with the simulation approach using DMS, by which we simply created a single restricted and impermeable cylinder to model a neuronal fibre. The initial positions of the diffusing particles were randomly distributed completely inside the fibre. The global parameters

used for the random walk MC simulations were as follows: $N_p = 10^5$, $N_I = 1.5\times10^5$, $t_s = 1$ μm, and $D = 2\times10^{-3}$ mm^2/s, which produced a RMS distance of 0.1 μm. Then, we used DMS to simulated a PGSE sequence to study the effect of δ on the dMRI signal acquired as a function of orientation. We applied a δ of 1/5/55 ms, and other parameters including Δ_e (= 60 ms), TE, b-value, and q-value were all kept constant in each condition. Note that we did not model the effect of T_2 relaxation and MR noise in either of the simulations in order to investigate the pure δ effect.

In the first part of the simulation, we studied the dependence on b-value. The fibre diameter was fixed at 5 μm, and b-values of 4,000 and 8,000 s/mm^2 were obtained by increasing the diffusion gradient intensity. For each δ, the noiseless DW signal was synthesized along a set of 360 uniformly distributed gradient directions spanning the plane containing the fibre direction. In the second part of the simulation, we studied the dependence on fibre diameter. Fibre diameters of 4 and 8 μm were studied using a fixed b-value of 5,000 s/mm^2, with the same DW gradient scheme as for the first simulation.

5.3.2 Microcapillary Phantom

A single fibre phantom was manufactured using plastic microcapillaries with inner and outer diameter of 20 and 90 μm (flexible fused silica capillary tubing, Polymicro Technologies, Phoenix, Arizona, USA) [Cho et al. (2008); Tournier et al. (2008); Yeh et al. (2008)]. Numerous capillaries were compactly aligned in the same direction in a flat plastic holder. Fig. 5.4(a) shows the photo of the single fibre phantom. A crossing fibre phantom was build by stacking two single fibre phantoms shown in Fig. 5.4(a) onto each other. The whole phantom was immersed in water, shaken in order to remove the bubbles and left for a period of days to ensure complete filling of the capillaries. Fig. 5.4(b) shows a T_2-weighted image of a crossing fibre phantom for the case of 45° angle.

For the case of single fibre phantom (see Chapter 5.3.4 below for the case of crossing fibre phantom), data were acquired using a 9.4 Tesla MR spectrometer (Bruker BioSpin, Ettlingen, Germany) equipped with a micro-imaging gradient system, which gives a maximum intensity of 1,460 mT/m. The micro-imaging system enables high b-value and high q-space diffusion studies satisfying the narrow pulse approximation, making investigations into the effects of various δ feasible. DW datasets were acquired using a 2D-FT stimulated-echo diffusion sequence with the following parameters: matrix size = 32×32, field-of-view (FOV) = 25×25 mm, slice thickness = 1.5 mm, TR/TE = 2,300/80 ms, δ = 2/12/36 ms, and Δ_e = 100 ms. For each δ, the b-value dependence was investigated by varying G in accordance with δ, to produce b-values of 1,000 and 4,000 s/mm^2, corresponding to q-values of 16 and 32 mm^{-1}. The DW gradient scheme consisted of 40 orienta-

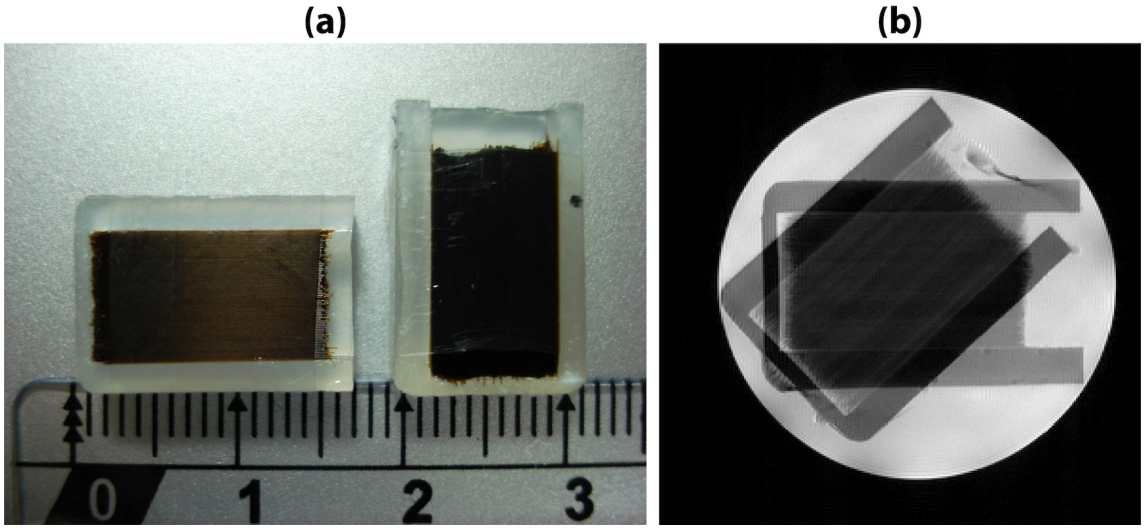

Figure 5.4: Microcapillary diffusion phantom. - (a) the two placeholders containing the plastic microcapillaries (the scale markings are in centimetres). (b) a T_2-weighted image of the microcapillary phantom, for the case of a 45° crossing angle.

tions applied at 9° intervals in the plane containing the fibre direction. Image pairs with opposing gradient directions were combined using geometric averaging to reduce imaging cross-term effects [Neeman et al. (1991)].

5.3.3 Sciatic Nerve Phantom

The sciatic nerves were dissected from a healthy 8-month-old male Sprague-Dawley (SD) rat. Previous morphometric studies on sciatic nerves of SD rats performed using histological staining have shown that the average inner and outer axonal diameters are around 4.9 and 7.3 μm respectively, i.e. the myelin thickness is close to 1.2 μm [Wright and Nukada (1994)]. The animal was first overdosed with an intraperitoneal injection of sodium pentobarbital (Sigma, USA) and then transcardiatic perfusion was performed using 0.9 % isotonic saline in order to preserve the integrity of neuronal cells. The sciatic nerves were extracted from both sides from the sciatic notch to the knees (∼1 cm in length) and aligned along the same direction. They were then immersed in 0.9 % isotonic saline for the imaging experiment, which was performed within 1 hour of the nerve preparation. Animal preparation procedures were in accordance with the Guidelines for Care and Use of Experimental Animals of the Laboratory Animal Centre in National Yang-Ming University.

DW datasets were collected using the 9.4 Tesla Bruker Spectrometer using the micro-imaging gradient system. A PGSE diffusion sequence was used with the following parameters: matrix size = 64×64, FOV = 7.5×7.5 mm, slice thickness = 6.5 mm, TR/TE = 3,600/94.6 ms, Δ_e = 50 ms, δ = 2/4/8/16/32 ms, The DW gradient intensity G was varied to obtain the same b-value

under various δ, for b-values = 1,000/4,000/8,000/12,000 s/mm^2. The DW encoding scheme of 36 gradient orientations applied at 10° intervals was used for data acquisition. As before, image pairs with opposing gradient directions were combined using geometric averaging to reduce imaging cross-term effects [Neeman et al. (1991)].

5.3.4 QBI of Crossing Fibre Phantoms

To evaluate the influence of δ effect on mapping fibre directions, we collected ground-truth dMRI datasets of 45° crossing fibres through DMS and the plastic microcapillary phantom described in Chapter 5.3.2.

Synthetic dMRI data were generated via DMS. Two cylindrical fibre bundles with a diameter of 10 μm intersecting at 45° were created, and MC simulations were performed using $N_p = 2{\times}10^5$, $N_I = 1.5{\times}10^5$, $t_s = 1$ μs, and $D = 2{\times}10^{-3}$ mm^2/s. Synthetic diffusion signal was calculated using a PGSE pulse sequence with $\Delta_e = 60$ ms, $\delta = 1/5/55$ ms, b-value = 5,000 s/mm^2, SNR = 15. The HARDI DW gradient scheme constituted 80 unique orientations generated using an electrostatic repulsion model [Jones et al. (1999)], along with their opposite directions, for a total of 160 gradient directions. The data syntheses were repeated 1,000 times for each δ.

Experimental dMRI data of microcapillary phantom were acquired on the 9.4 Tesla Bruker spectrometer using a 2D-FT stimulated echo sequence with the following parameters: matrix size = 32×32, FOV = 24×24 mm, slice thickness = 3.2 mm, TR/TE = 2,300/80 ms, Δ_e = 100 ms, δ = 2/12/36 ms, and b-value = 4,000 s/mm^2. The same HARDI sampling scheme composed of 160 gradient directions was used. As before, image pairs with opposing gradient directions were combined using geometric averaging to reduce imaging cross-term effects [Neeman et al. (1991)].

5.3.5 Data Analysis

Single Fibre Phantom Data. The single fibre phantom data (i.e. Chapter 5.3.1, 5.3.2, and 5.3.3) are displayed using polar plots, showing the DW signal measured as a function of DW gradient orientation under different values of δ. The DW signal of each phantom data was normalized to the null signal intensity (i.e. $b \sim 0$) for comparison.

Crossing Fibre Phantom Data. The crossing fibre data (i.e. Chapter 5.3.4) were reconstructed using QBI [Tuch (2004)] to provide the ODF, with angular sampling resolution of 4° (16-fold tessellated icosahedrons). To reduce the error caused by the discrete spherical sampling of ODF, we randomly rotated the angular sampling scheme and computed the ODF 1,000 times for each voxel [Cho et al. (2009)]. During each ODF calculation, we considered local maximum vectors of

each ODF with lengths greater than 50 % of the peak ODF value as the potential fibre directions. Finally, the mean of potential directions were regarded as the final fibre orientations. The quality of the orientation estimation was assessed using:

1. *Azimuthal and elevation angles.* In voxels where QBI successfully distinguished two fibre directions, we projected the two directions onto the azimuthal and elevation plane, and then computed the mean and the standard deviation across voxels.

2. *Success rate.* The proportion of voxels within which the two main fibre directions could be identified.

5.4 Results

5.4.1 Single Fibre Studies

The results obtained from the single fibre studies showed that the application of longer δ resulted in higher DW signal being measured along the radial directions, with little or no change along the axis of the fibres (Fig. 5.5, 5.6, 5.7 & 5.8).

Figs. 5.5 & 5.6 are the results of DMS simulations. For a fixed fibre diameter of 5 μm, the effect of a longer δ was more evident at the higher b-value of 8,000 s/mm^2 (Fig. 5.5). The effect is also more evident for larger axon diameters: the increase in DW signal in the radial direction was more obvious for the 8 μm diameter fibre than for the 4 μm fibre, under the same b-value of 5,000 s/mm^2 (Fig. 5.6). Note the axial DW signal was very close to zero due to the almost complete dephasing of the signal for unrestricted diffusion.

The results of the single fibre DW water microcapillary phantom are shown in Fig. 5.7. For b-value = 1,000 s/mm^2, the radial DW signal increased by 5.4 % and 16.4 % when δ was increased from 2 ms to 12 ms and 36 ms respectively. The effect was even greater at b-value = 4,000 s/mm^2, with increases of 29.8 % and 74.8 % respectively. In both cases, there were little or no changes in axial DW signal.

The same trends were also observed in the rat sciatic nerve data (Fig. 5.8). At b-value of 1,000 s/mm^2, the effect of increasing δ was negligible. However, the effect could be readily observed at b-values of 4,000 s/mm^2 and greater, with longer δ leading to enhanced radial DW signal. The effect of δ became even more evident at the higher b-values of 8,000 and 12,000 s/mm^2. Consistent with the simulations and phantom experiments, the use of long δ led to an overall increase in the DW signal for a given b-value.

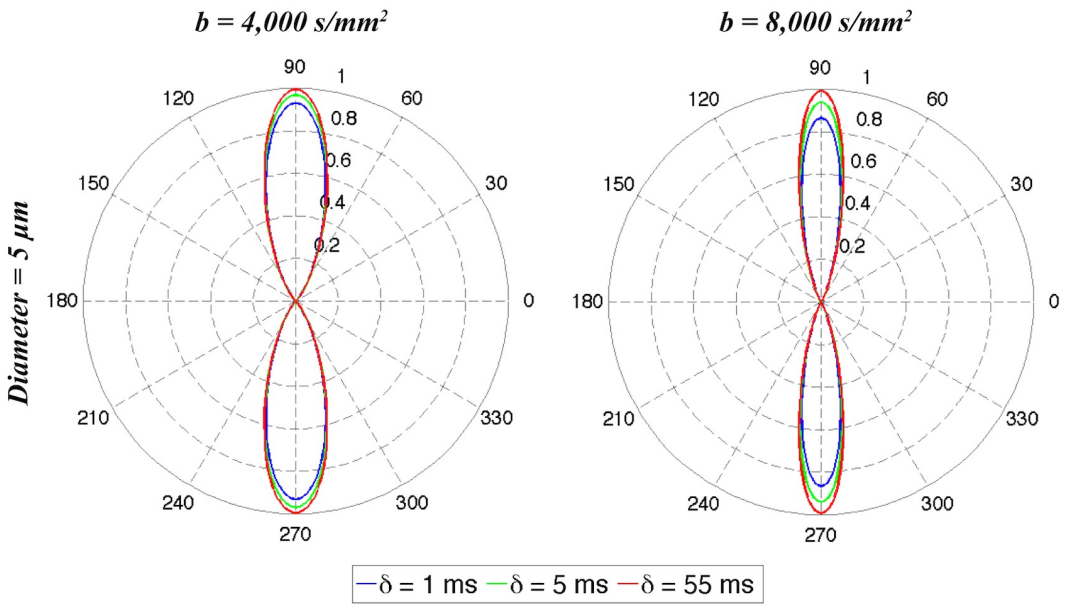

Figure 5.5: The δ effect on the DW signal and the dependency on b-value: DMS simulations. - Polar plots of the normalized DW signal obtained from the single fibre DMS simulation data using $\delta = 1/5/55$ ms, shown in blue/green/red respectively. The angles noted on the plots were determined from the direction of the simulated fibre and the DW gradient orientations. Two b-values of 4,000 and 8,000 s/mm^2 were applied while using a fixed fibre diameter of 5 μm.

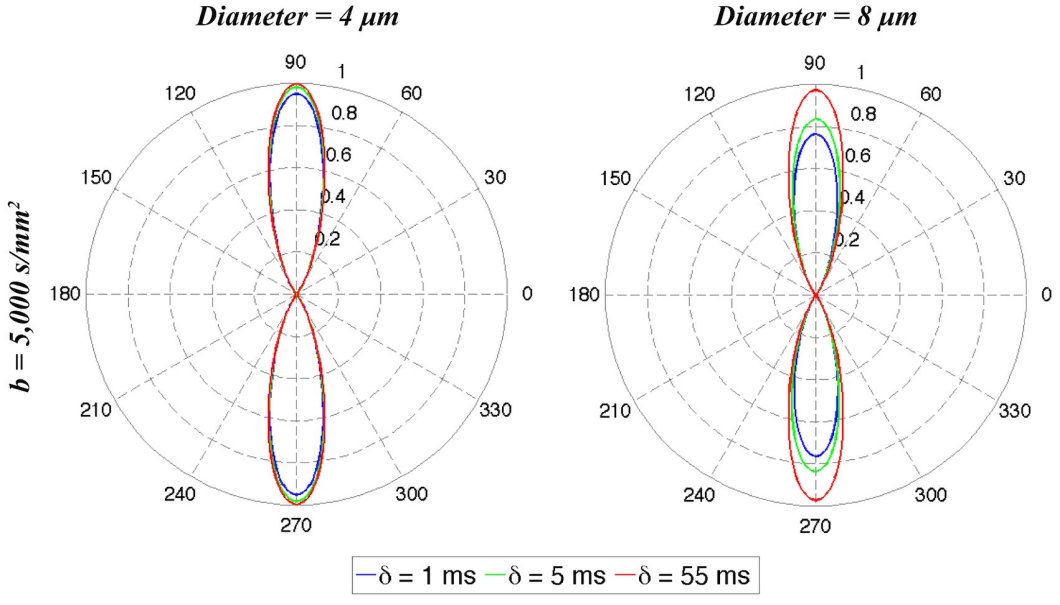

Figure 5.6: The δ effect on the DW signal and the dependency on fibre diameter: DMS simulations. - Polar plots of the normalized DW signal obtained from the single fibre DMS simulation data using $\delta = 1/5/55$ ms, shown in blue/green/red respectively, with the axial (fibre) axis oriented left-right (i.e. 0° and 180°). The fibre diameter was set at 4 μm and 8 μm while applying a fixed b-value of 5,000 s/mm^2.

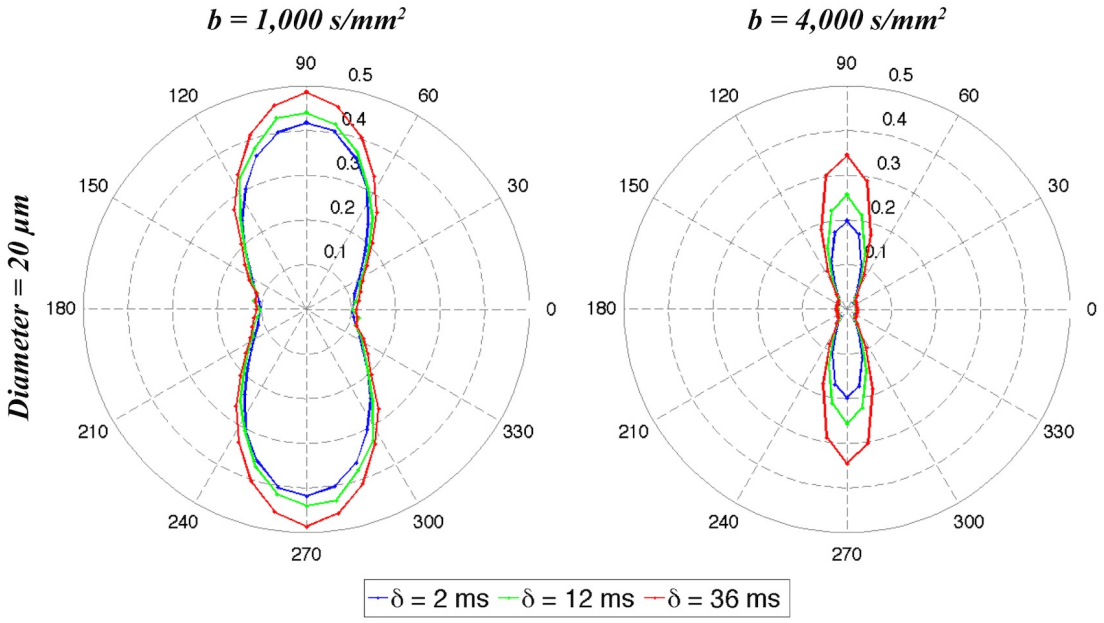

Figure 5.7: The δ effect on the DW signal and the dependency on b-value: microcapillary phantom. - Polar plots of the DW signal normalized to the b=0 signal, obtained from the water capillary phantom, using δ = 2 (blue), 12 (green), and 36 (red) ms, with the axial (fibre) axis oriented left-right (i.e. 0° and 180°). The results were obtained using two b-values of 1,000 and 4,000 s/mm^2 while fixing TE = 80 ms. The internal diameter of the plastic capillaries was 20 μm.

5.4.2 Crossing Fibre Studies

Figs. 5.9 & 5.10 show the plots of fibre orientation estimation obtained from the QBI-ODF reconstruction of the crossing fibre data obtained from DMS simulations and microcapillary phantom dMRI experiments. The estimated fibre orientations were projected onto the azimuthal and elevations planes for each voxel containing crossing fibres. Both the accuracy and precision were increased using a longer δ. The quantitative results are summarized in Tables 5.1 & 5.2. As suggested by the experiments on the single fibre phantom, the results in the table show that applying a longer δ improves the precision of the estimated fibre orientations slightly, and improves the success rate significantly. Consistent with previous studies [Tournier et al. (2008); Zhan and Yang (2006)], a significant bias was found with QBI, with the separation between the two fibre orientations being underestimated.

5.5 Discussion

In recent years, a variety of diffusion imaging techniques based on the q-space theory have been proposed to map complex neuronal fibre architecture [Assaf et al. (2004); Assaf and Basser (2005); Tuch (2004); Wedeen et al. (2005); Wu and Alexander (2007)], but the failure to

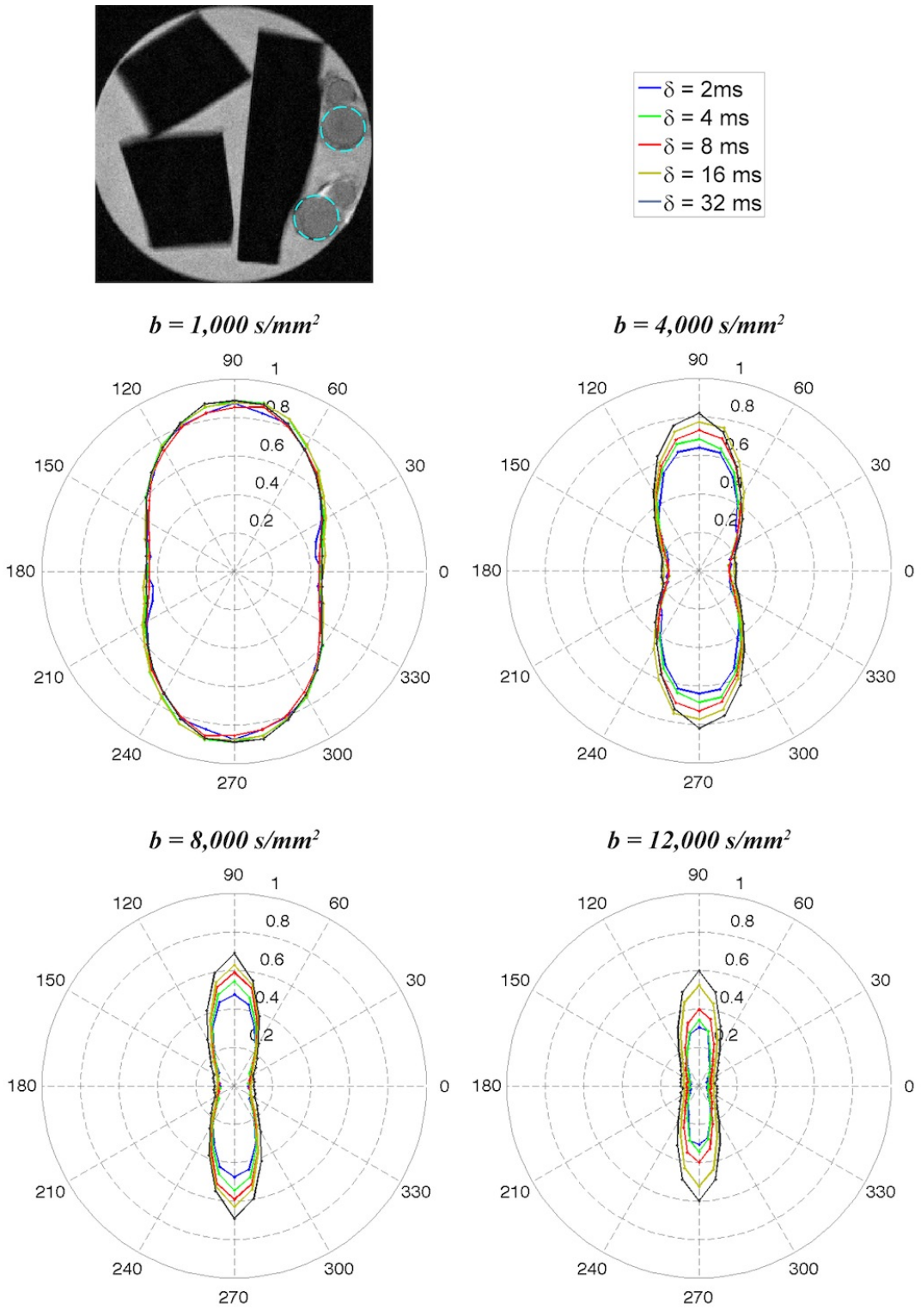

Figure 5.8: The δ effect on the DW signal and the dependency on b-value: sciatic nerve model. - The results were obtained from the rat sciatic nerve phantom using δ = 2/4/8/16/32 ms (colored in blue/green/red/yellow/grey) and a range of b-values from 1,000 s/mm^2 to 12,000 s/mm^2. A T_2-weighted image of the sciatic nerves is shown in the top left panel, with the regions of interest from which the signal was measured highlighted in light blue circles.

Table 5.1: The fibre orientations of the two crossing fibre populations measured using QBI from the DMS simulation data under various δ at b-value = 5,000 s/mm^2. The T_2-decay was not modeled for this simulation.

	Fibre orientation 1		Fibre orientation 2		
	Azimuth	Elevation	Azimuth	Elevation	Success rate
δ = 1 ms	3.5° ± 5.4°	0.1° ± 2.5°	41.7° ± 4.6°	-0.2° ± 2.3°	70 %
δ = 5 ms	3.5° ± 4.6°	0.1° ± 2.3°	42.0° ± 3.6°	-0.4° ± 2.1°	84 %
δ = 55 ms	2.8° ± 2.9°	0.1° ± 1.4°	42.4° ± 2.2°	-0.3° ± 1.7°	91 %

Table 5.2: The fibre orientations of the two crossing fibre populations measured using QBI from the microcapillary phantom data under various δ using fixed TE of 80 ms at b-value = 4,000 s/mm^2.

	Fibre orientation 1		Fibre orientation 2		
	Azimuth	Elevation	Azimuth	Elevation	Success rate
δ = 2 ms	5.2° ± 4.0°	0.4° ± 2.9°	36.3° ± 11.0°	0.2° ± 2.7°	74 %
δ = 12 ms	4.2° ± 2.8°	0.1° ± 1.7°	40.0° ± 4.5°	0.6° ± 2.0°	86 %
δ = 36 ms	3.8° ± 1.8°	0.1° ± 1.2°	40.6° ± 4.2°	0.5° ± 1.3°	90 %

meet the SGP approximation on clinical systems has been a recurrent criticism. In this chapter, we show that rather than being a deficiency, the use of long δ is not a disadvantage for fibre orientation estimation, since it provides a moderate boost in signal, and an increase in angular contrast due to the differential radial/axial effect. We described the theory for the long δ effect (Section 5.2), which is supported by the simulations of DMS and dMRI experiments on microcapillary phantom and animal models. While it is not possible to validate this effect using clinical MR scanners due to the limited gradient amplitude, our results imply that the current practice of using long δ for dMRI on human clinical MR scanners, which is enforced by hardware limitations, may also be beneficial for estimating fibre orientations. However, it is still important to note that this only applies to ODF estimation; and that for true q-space displacement measurements, the narrow pulse approximation is still required.

5.5.1 Impact of T_2-decay

In most clinical studies, as spin-echo sequences are typically used, the effect of T_2-decay is important and may have a greater impact on the amount of signal available than the long δ effect. This can be investigated by considering a PGSE diffusion sequence, assuming a T_2 value for white matter at 3T of 60 ms [Alexander and Barker (2005)]. Under the condition of constant Δ_e and b-value, the minimum TE values for δ = 1/5/55 ms are 68.5/73.8/140.53 ms respectively. In this case, the T_2 effect clearly dominates over the δ effect. In other words, the increase in minimum TE associated with a longer δ leads to a reduction in the signal that is much greater than any increase

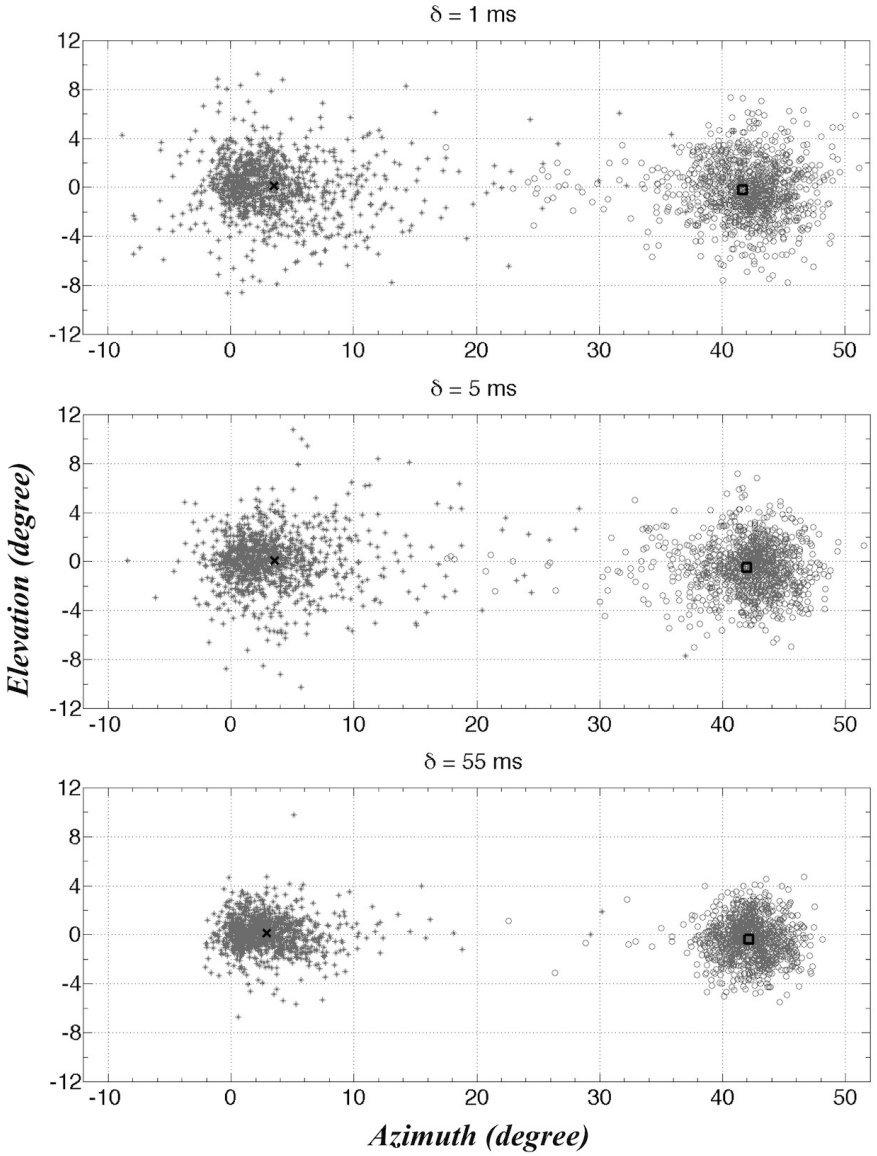

Figure 5.9: Fibre orientation estimation of the crossing fibre DMS simulation data. - (Crossing angle = 45°, b-value = 5,000 s/mm^2). From top to bottom: δ = 1, 5 and 55 ms. For all voxels contained in the fibre-crossing region, fibre orientations are projected onto the azimuthal (x-axis) and elevation (y-axis) planes. The two directions are displayed by "*" and "-" symbols, and the black cross ($\times$) and the black square ($\square$) represent their mean values.

associated with the longer DW pulse. However, under these conditions, the DW gradient amplitude G increases as δ decreases, since $b = (\gamma G\delta)^2(\Delta - \delta/3)$ and $\Delta_e = \Delta - \delta/3$ is constant. In practice the shortest achievable DW pulse duration would therefore be determined by the available gradient strength. Under the more clinically relevant condition of constant (i.e. maximum available) DW gradient amplitude G and constant b-value, a shorter δ leads to a marked increase in Δ_e, and hence to a marked increase in minimum TE. In this case, a longer δ is clearly optimal, leading to shorter

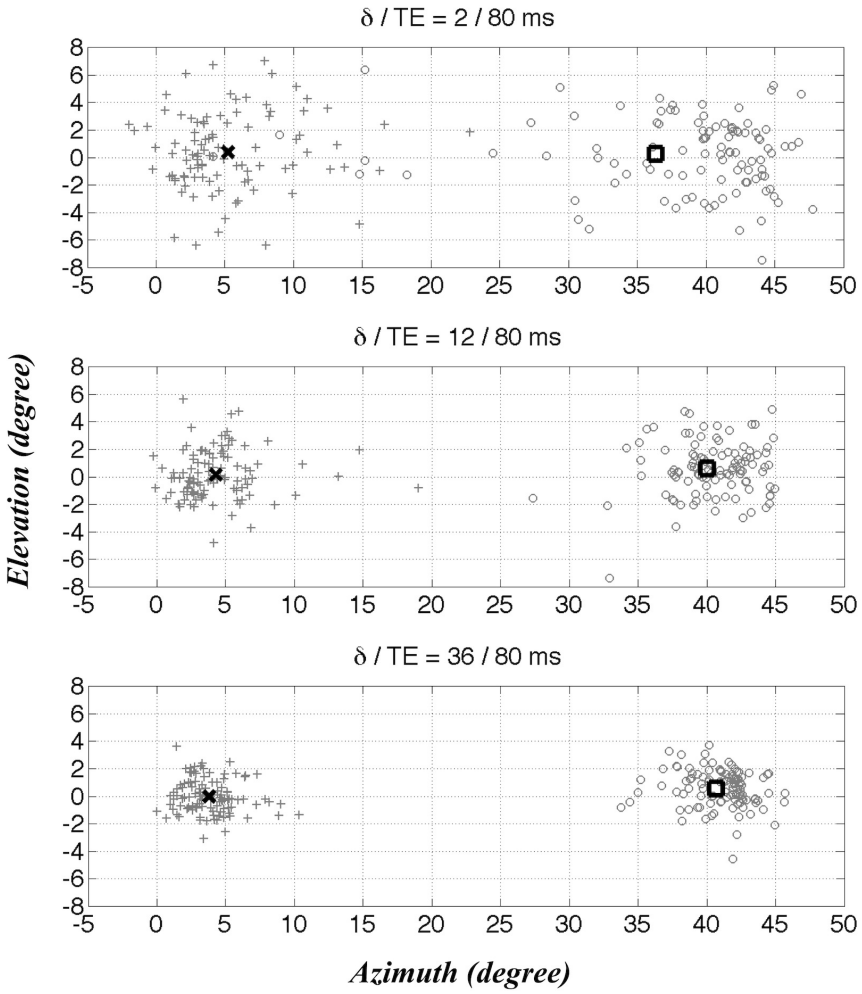

Figure 5.10: Fibre orientation estimation of the crossing fibre microcapillary phantom data. - (Crossing angle = 45°, b-value = 4,000 s/mm^2). From top to bottom: δ = 2, 12 and 36 ms. For all voxels contained in the fibre-crossing region, fibre orientations are projected onto the azimuthal (x-axis) and elevation (y-axis) planes. The two directions are displayed by "+" and "-" symbols, and the black cross (×) and the black square (□) represent their mean values.

echo times as well as increased transverse DW signal. This suggests that the current practice of using long DW pulse durations to minimize the diffusion time (and hence TE) is optimal for the purpose of fibre orientation determination (for a given desired b-value). Furthermore, if the MR system is capable of achieving higher gradient strengths, this should be used to shorten the TE in order to obtain DW images with higher SNR.

5.5.2 Validity of Single Restricted Fibre Simulation

As shown in the simulation results in Fig. 5.5, there was remarkably little attenuation of the radial DW signal under the application of a long δ at both b-value 4,000 s/mm^2 and 8,000 s/mm^2. Indeed,

there was almost no signal decay with $\delta = 55$ ms. According to the Einstein equation (Eq. (2.10)), with $\delta = 55$ ms the RMS displacement should be $r = 25.7$ μm, which is much greater than the fibre diameter (5 μm); hence, during the application of the diffusion gradient pulse each spin will have sufficient time to explore the entire restricted space and its effective position for both the labelling and unlabelling will be very close to the central axis of the fibre. Since the resultant spin displacements will be small, there will be almost no radial signal decay, even using a high b-value of 8,000 s/mm^2. This effect (i.e. the almost complete absence of transverse DW attenuation with long δ) is likely to be exaggerated in our simulation applied in this study, since (i) no extra-axonal compartment is included in the model; and (ii) the axonal compartment is modeled as fully restricted (this second point is also true of the water capillary phantom). Water molecules in the extra-axonal compartment would presumably be more mobile, and their DW signal would therefore be more strongly reduced. They would however contribute equally to the $b = 0$ signal (ignoring any differences in T_2), leading to greater DW attenuation for the combined sample. However, if the intra- and extra-axonal compartments can be assumed to be non-exchanging (see below), the DW signal corresponding to the intra-axonal volume fraction is likely to exhibit this effect as suggested by the simulations.

Likewise, membrane permeability is expected to lead to greater DW attenuation if the diffusion time is comparable with the average lifetime of molecules within the intra-axonal compartment. However, the *intracellular* water pre-exchange lifetime (or the residence time) in the rat brain has been estimated to be greater than 500 ms [Quirk et al. (2003)], which is much longer than the diffusion times of 50-100 ms that are typically used for human studies. Moreover, these measurements were taken from deep gray matter structures; the equivalent lifetimes in myelinated white matter are likely to be considerably longer due to the additional barrier imposed by the myelin sheath. This suggests that modeling diffusion within axons as restricted is a valid approximation, and this assumption has indeed been successfully used in other modeling frameworks (e.g. [Assaf et al. (2004); Assaf and Basser (2005)]).

5.5.3 Inference of Finite δ on Fibre Radius Estimation

The simulation results in Fig. 5.6 show the dependence on fibre diameter. Intuitively, the spin displacements will be shorter along the radial direction of a completely restricted fibre with a smaller diameter, which gives reduced DW signal attenuation. Similarly, a short δ in a larger diameter fibre results in greater DW signal attenuation. However, using a long δ the DW signal attenuation is similar for both fibre diameters studied. The present results therefore have interesting

implications for the measurement of axonal diameters. The main determinant for the effect of DW pulse duration is the size of the restricting compartment (i.e. axonal diameter) relative to the RMS displacement over the timescale of the DW pulse duration. Assuming a diffusion coefficient $D = 2{\times}10^{-3}$ mm^2/s, the time required for the RMS displacement to exceed an axonal diameter $r = 5$ μm is approximately 2 ms, after which time the average position of the spins will tend towards the central axis of the axon. This implies that for diffusion pulses much longer than 2 ms, the radial signal will be independent of axonal radius for radii less than 5 μm. This value is even smaller for smaller radii, as it scales with r^2: with $r = 2$ μm, δ should be in the region of 300 μs or less. The smallest measurable axonal diameter is therefore determined by the shortest DW pulse duration achievable. On the other hand, this also implies that if long diffusion gradient pulses are used (as is the case in clinical diffusion MR imaging protocols), the DW signal intensity is largely independent of the axonal fibre diameter (within the biologically relevant range). Interestingly, this may indicate that indices that are sensitive to changes in the apparent radial diffusivity, such as fractional anisotropy (FA), are unlikely to be sensitive to axonal diameters in a clinical setting (i.e. when long δ are used).

5.5.4 Validity of Microcapillary Phantom Model

The water capillary single fibre phantom study confirms that the application of a long δ results in less signal attenuation than a short δ, with all other imaging parameters fixed. The effect of δ was exaggerated using this model as the internal diameter of the plastic capillaries was 20 μm, which is larger than the typical range for neuronal fibres of 1 to 10 μm. Nonetheless, this single fibre phantom model provides an experimental demonstration of the physical phenomenon in a fully restricted environment.

5.5.5 The δ Effect on Real Biological Tissues

The excised rat sciatic nerves were used to investigate the effect of long δ on biological tissues. As expected, the radial DW signal intensity decreased using a shorter δ, with little or no changes in the axial direction. The application of a long δ 'stretches' the DW signal profile, thereby increasing the angular contrast between the DW signals acquired along different directions. This is beneficial for fibre orientation estimation as it provides improved discrimination between different fibre orientations [Cho et al. (2008)]. It is interesting to note that as suggested by the simulations, the attenuation of the DW signal in the radial direction when using a long δ is not affected by b-value as strongly as might be expected, going from ~90 % at $b = 1{,}000$ s/mm^2 to ~60 % at $b = 12{,}000$

s/mm^2. Indeed, this is consistent with the previous suggestion of increased DW attenuation for the extra-axonal compartment, with little or no DW attenuation for the intra-axonal compartment. Unfortunately, this hypothesis cannot be tested with the results shown in the present chapter, and further work (beyond the scope of this study) would be required to verify whether this is indeed the case.

5.5.6 Inference of q-value

Note that in our single fibre studies, we investigated the δ-effect against b-values rather than q-values. For a fixed q-value, keeping the diffusion time Δ constant implies that the diffusion pulses will actually be spaced closer together (for non-negligible δ) than for the fixed b-value case (where $\Delta_e = \Delta - \delta/3$ is kept constant). This should result in an even greater effect of long δ for the constant q-value case. Therefore, the δ-effect for fibre orientation estimation is applicable to both b-value and q-value formulations.

5.5.7 Inference of finite δ on clinical applications

To demonstrate that using long diffusion gradient pulses is actually beneficial for the purpose of fibre orientation estimation, we performed QBI analyses on the simulated and the microcapillary crossing fibre phantoms. We observe that using a long δ can decrease the standard deviation of the azimuthal and elevation angle, as well as increase the percentage success rate, as shown in Tables 5.1 & 5.2 and Fig. 5.9 & Fig. 5.10. This may be due both to the increased overall signal at long δ, and the improved angular contrast. While the use of long δ is therefore beneficial, it should however be noted that these results also confirm the significant bias in the separation angle previously reported for QBI [Zhan and Yang (2006); Tournier et al. (2008)].

For simplicity, in this chapter we only used the QBI reconstruction method to analyze the HARDI data. However, we expect that a long δ will also be beneficial for other diffusion imaging approaches to discriminate crossing fibres. In diffusion spectrum imaging (DSI) [Lin et al. (2003); Wedeen et al. (2005)] for example, although the finite δ is problematic for measuring microstructural dimensions due to the underestimation of the extent of the spin propagator [Mitra and Halperin (1995); Lätt et al. (2007); Bar-Shir et al. (2008)], such effect may not be a drawback for mapping fibre orientations. In general, since using a long δ enhances the DW angular contrast and the overall signal of DW images, it should also be beneficial for other diffusion techniques for fibre orientation estimation.

In most clinical sites, δ is already set to the longest possible in order to achieve the required

b-value in the shortest TE [Alexander and Barker (2005)]. Here, we have shown that far from being problematic, a long δ may actually be beneficial for fibre orientation estimation, and thus for fibre-tracking applications. Our results indicate that for most current DW MRI techniques to map complex fibre architecture, which utilize intermediate to high b-values, the application of a long δ should not be considered a limitation for the purposes of fibre orientation estimation.

5.6 Conclusion

Due to MR hardware limitations, it is necessary for current DW acquisition protocols on clinical scanners to use long δ values. Although a longer δ is problematic for quantitative q-space analyses, we have shown that it can actually enhance both the overall signal of DW images and the contrast between DW gradient directions. We have demonstrated and validated this effect through simulations and experiments, and the results support that a long δ value is advantageous for resolving crossing fibres and estimating their orientations. This effect is expected to be beneficial for related post-processing methods including fibre-tracking applications and segmentation based on diffusion data.

5.7 Acknowledgments

Many thanks to the Functional and Micro-Magnetic Resonance Imaging Centre funded by the National Research Program of Taiwan for Genomic Medicine for the technical support, and also to Ke-Hsin Chen for the great assistance for the animal preparation.

Chapter 6

Evaluation of Fibre Radius Mapping Using Clinical Diffusion MRI Systems

Contents

6.1 Introduction

For current clinical application of dMRI, diffusion tensor imaging (DTI) is still the most widespread method to characterize diffusion anisotropy for inferring the integrity and orientation of the WM tracts [Basser et al. (1994b, 2000)]. However, DT indices such as the mean diffusivity (MD) and fractional anisotropy (FA) (Eq. (2.26) & (2.27)) are the quantities describing water diffusion behavior in biological tissues, which may not directly reflect the microstructure features or conditions of biological tissues. That is, for instance, the FA values of the two groups of fibre bundles may be equivalent (i.e. the same degree of diffusion anisotropy) although their diameters are different [Shemesh et al. (2010c)]. In recent years, a number of elaborate microscopic dMRI techniques have been proposed to directly probe microstructural characteristics of tissues, such as cell size, fibre density, and membrane permeability. These direct measures of tissue properties can be utilized as novel biomarkers to monitor tissue status.

The origin of microscopic dMRI can be referred to the q-space imaging (QSI) by which dMRI can be utilized to probe the size of microstructures from the PGSE dMRI data (Chapter 2.3.2) [Callaghan (1993); Cory and Garroway (1990)]. Ong *et al.* utilized the QSI principle to generate the mean axon diameter maps of mice's spinal cords, which were then validated using simulations and histology [Ong et al. (2008)]. Assaf *et al.* developed 'AxCaliber' to estimate fibre diameter distribution by fitting the model of restricted and hindered water diffusion in the intra- and extra-axonal space (Chapter 2.5.1) [Assaf et al. (2004, 2008)]. Ozarslan *et al.* and Shemesh *et al.* performed MSDI experiments by employing a double-pulsed-field-gradient sequence to explore compartment anisotropy, pore size and shape at microscopic level [Ozarslan and Basser (2008); Ozarslan et al. (2009); Ozarslan (2009); Shemesh and Cohen (2008); Shemesh et al. (2009a,b, 2010a,b,c)]. Xu *et al.* applied an OGSE sequence, which enables DW experiments at a high temporal resolution, to increase the sensitivity of DW measurements to tissue microstructure [Stepisnik (1993); Xu et al. (2009a,b)].

The advanced dMRI techniques described above are useful methodologies for imaging microstructures, however, it is difficult to implement these methods on the current clinical MR scanners because of the following reasons: Both AxCaliber and QSI require adequate gradient intensity in order to fulfill the narrow gradient pulse requirement; while OGSE needs high gradient capability (e.g. strength and slew rate) to increase the sensitivity and resolution of dMRI measurements. Owing to the safety consideration and hardware limitations, a high gradient system cannot be installed on a clinical MRI system. As for MSDI, although it has the potential to deliver microscopic information with lower gradient strengths via an angular double PGSE approach, at

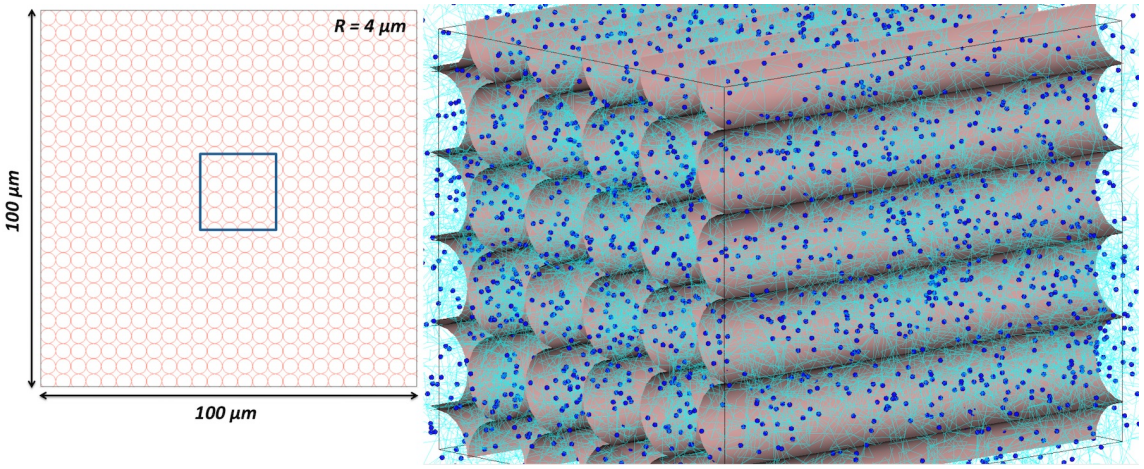

Figure 6.1: An example of the MC simulation environment for fibre radius mapping. - (Left) The transverse view of the simulation scene, which contained 625 mesh-based cylinders. For each cylinder, the radius (R) and the length were 4 and 500 μm respectively. (Right) A zoomed area within the square in the left column, illustrating the diffusing particles (dark blue) and their motion trajectories (light blue).

the present time MSDI is limited to theoretical descriptions, simulations, and experimental studies on preclinical MRI systems. In addition, the double-PGSE-based MSDI approach relies on a prior knowledge on fibre orientations that are actually unknown for most of the neuronal pathways. An alternative MSDI method utilizes a bipolar double-pulsed-field-gradient sequence, by which the pore size and shape of randomly oriented porous media can be accurately estimated [Shemesh et al. (2010a)]. However, this pulse sequence generally needs to increase the number of averaging in order to compensate the low SNR caused by a very long TE. Thus, it is not suitable for clinical application where the scan time has to be taken into account. Furthermore, the MSDI pulse sequences are not available on the modern MRI scanners since they are not yet commercial packages.

Alexander developed an optimization framework for dMRI experimental design on a conventional PGSE pulse sequence, which allows in vivo estimate of fibre diameter and density without a prior knowledge on fibre orientations [Alexander (2008); Alexander et al. (2010)]. The method is able to effectively create the optimal dMRI protocols for measuring the cellular sizes or fibre radii found in the human brains, nevertheless the difficulties still remain for clinical examinations in two aspects. Firstly, the optimized imaging strategy is generated for a specific fibre radius, whereas the WM of human brain covers a range of fibre diameter approximately from 1 to 10 μm; secondly, a high gradient intensity (at least 70 mT/m) is essential for accurate estimation of small fibre radii, while common clinical MR scanners are equipped with a standard gradient system that has a maximum amplitude of 40 mT/m. Accordingly, the purpose of this study is to assess the possibility of mapping fibre radii using standard clinical MRI scanners with the constraints on the gradient

system capabilities, as well as to investigate the impact of dMRI parameters. Based on DMS, we make efforts to translate the method of direct microstructure mapping to clinically feasible MRI systems, respecting the hardware and safety constraints. The procedure for evaluation is as following, and the details are described in the Methods session: (a) *DMS Monte Carlo simulations*: We performed large-scale Monte Carlo simulations of Brownian dynamics of water molecules in 3D spaces that contained axonal fibres with various sizes. (b) *Clinical diffusion imaging protocols*: Based on a single PGSE pulse sequence, we designed a series of dMRI protocols conformed to the capabilities of clinical MR systems. (c) *DMS MR signal syntheses*: A step-by-step MR signal synthesizer was utilized to generate DW signal, which was determined by the trajectory of water diffusion in (a) and the sequence parameters in (b). (d) *Model parameter estimation*: We applied the method described in [Alexander (2008)] to extract tissue microstructural characteristics from the synthetic DW datasets in (c).

6.2 Methods

6.2.1 DMS: Monte Carlo Simulations

Random walk MC simulations were performed using DMS to simulate 3D water diffusion in a cubic network of straight parallel impermeable fibres constructed by mesh-based cylinders. We created four simulation environments with the same intracellular fraction ($f_i = 0.74$), and each of them contains 25×25 fibres with a specific radius R (= 1/2/4/6 μm). Fig. 6.1 illustrates an example of the virtual WM tissue and the corresponding MC simulation. Each simulation run employed $N_p = 10^5$ and $N_I = 10^4$ iterations to produce a system complexity of 10^9, which ensured the reliability of the synthetic dMRI signal [Alexander (2008); Hall and Alexander (2009); Alexander et al. (2010)]. A constant diffusivity D of 2×10^{-3} mm^2/s was assumed to be equivalent in the intra- and extra-axonal space, and a simulation time step t_s of 10 μs was chosen to give a suitable RMS distance (r) of 0.32 μm.

6.2.2 Clinical Diffusion MRI Protocols

Table 6.1 summarizes a set of simulated PGSE dMRI protocols created to comply with the capabilities of the standard clinical gradient system. To remain a clinically acceptable scan time within half an hour, each protocol contained 120 DW acquisitions with different M and N combinations, where M was the number of q-space sampling shells and N was the number of DW gradient orienta-

Table 6.1: The design of simulated clinical dMRI protocols. (M: the number of q-space sampling shells; N: the number of diffusion gradient orientations per shell.)

Protocol	M	N	δ (ms)	TE (ms)	*b*-value (s/mm^2)
1	3	40	4, 8, 12	70.5	80, 350, 800
2			8, 16, 20	81.2	350, 1430, 2250
3			16, 20, 24	86.5	1430, 2250, 3250
4	4	30	4, 8, 12, 16	75.8	80, 350, 800, 1430
5			8, 12, 16, 20	81.2	350, 800, 1430, 2250
6			12, 16, 20, 24	86.5	800, 1430, 2250, 3250
7	5	24	4, 8, 12,16, 20	81.2	80, 350, 800, 1430, 2250
8			8, 12,16, 20, 24	86.5	350, 800, 1430, 2250, 3250
9	6	20	4, 8, 12,16, 20, 24	86.5	80, 350, 800, 1430, 2250, 3250

tions per shell. We utilized a pair of trapezoidal waveforms to model DW gradients with amplitude (G) and slew rate being fixed at 40 mT/m and 200 T/m/s respectively. The DW gradient pulse duration (δ) and separation (Δ) were varied simultaneously to keep a constant effective diffusion time Δ_e of 50 ms so as to reach adequate diffusion sensitizing factors (i.e. b-values) for short δs. Note that all of the b-values employed in this study were all clinically achievable. In each imaging protocol, the echo time (TE) was determined by the maximum δ and its corresponding Δ. TE was fixed within an imaging protocol in order to avoid the dependence on the precise knowledge of T_2 [Alexander (2008)]. A T_2 of 70 ms typically found in WM at a 3T MR scanner was used. Fig. 6.2 is an example of the designed dMRI protocol illustrating the PGSE pulse sequence diagrams.

6.2.3 DMS: MR Signal Syntheses

Synthetic DW signal (S) is computed by performing the numerical integration using the following equation:

$$S = S_0 exp\left(-\frac{TE}{T_2}\right)\left|\sum_{p=1}^{N_p} exp(j\phi_p) + \eta\right| \tag{6.1}$$

Comparing to Eq. (3.5), Eq. (6.1) takes into account the T_2-decay, and ϕ_p is the accumulated phase of the p-th particle calculated via a step-by-step spin phase integrator as follows:

$$\phi = \gamma \sum_{i=0}^{N_{TE}} \alpha \vec{G}(t_i) \cdot \vec{R}(t_i) t_s \tag{6.2}$$

In Eq. (6.2), α is +1 before and -1 after the refocusing radiofrequency pulse for a single PGSE pulse sequence. For a given time point t_i, where $t_i = i \times ts$, $\vec{G}(t_i)$ is the gradient vector derived from the imaging protocol; and $\vec{R}(t_i)$ is the particle's spatial position obtained from its diffusion trajectory (see Chapter 3.4 for references).

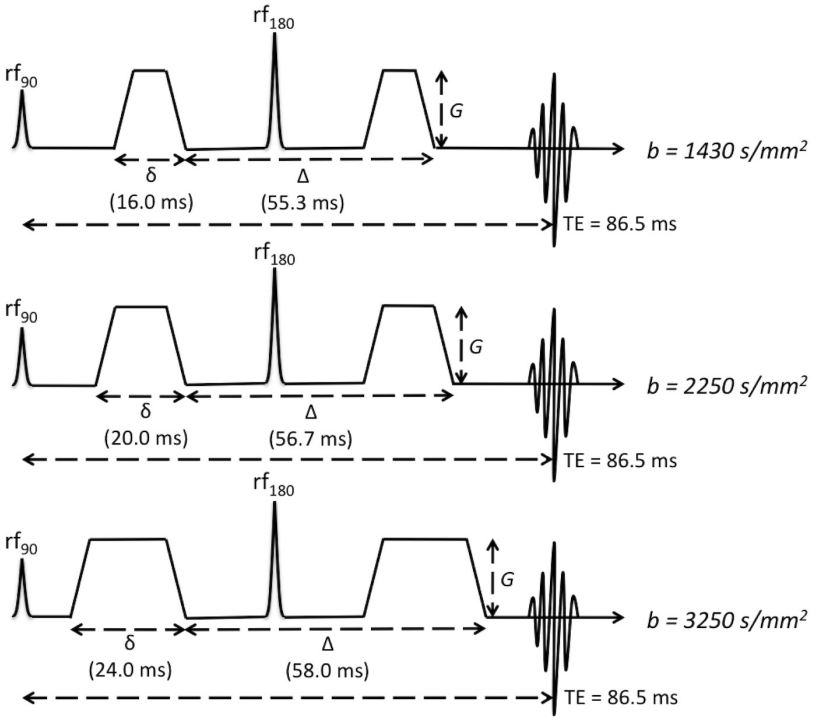

Figure 6.2: An example of the designed dMRI protocol. - The figure illustrates the pulse sequences of *Protocol* 3 in Table 6.1, where 'rf_{90}' and 'rf_{180}' are the excitation and refocusing radiofrequency pulses respectively.*Protocol* 3 contained three q-space sampling shells ($M = 3$) and each shell had 40 DW orientations ($N = 40$). For each PGSE sequence, both Δ_e and TE were fixed, and thus Δ increased simultaneously while a greater δ was used, which produced a larger b-value as well (from top to bottom).

6.2.4 Model Parameter Estimation

Parameter estimation was performed using the Markov Chain Monte Carlo (MCMC) method implemented with a Rician noise model to sample the posterior distribution of model parameters [Alexander (2008); Alexander et al. (2010)]. As described in [Alexander (2008)], the dependent parameters of the simple axon model were the volume fraction of the intracellular space (i.e. f_i), the fibre radius and orientation, and the axial ($D_{\parallel}$) and transverse ($D_{\perp}$) apparent diffusion coefficient. We first analyzed the synthetic dMRI datasets using DT reconstruction [Basser et al. (1994b)], from which the initial estimates for f_i, $D_{\parallel}$, and $D_{\perp}$ were obtained. Note that f_i related to the axon density and was initialized to the FA defined as the normalized standard deviation of the eigenvalues calculated from the DT model (Eq. (2.27)) [Basser and Pierpaoli (1996)]. The fibre direction (along z-axis) and radius (R) were initialized to the ground-truth values given in the MC simulations. Rician noise was added to the DW signal taking into consideration for the effect of varying TE between the protocols. The SNR was 50 on the null DW signal (i.e. $G = 0$) at the longest TE of 86.5 ms. In the procedure of MCMC, the burn-in period, sampling interval,

Table 6.2: Mean ± standard deviations of the posterior distributions on R for the corresponding dMRI protocol.

Protocol	*M*	*R* = 1 μm	*R* = 2 μm	*R* = 4 μm	*R* = 6 μm
1	3	1.54 ± 0.68	2.11 ± 0.61	4.11 ± 0.68	5.70 ± 0.65
2		1.22 ± 0.44	1.78 ± 0.33	3.91 ± 0.29	6.07 ± 0.58
3		1.02 ± 0.31	1.86 ± 0.26	3.88 ± 0.33	5.91 ± 0.34
4	4	1.07 ± 0.50	1.93 ± 0.65	3.81 ± 0.50	6.11 ± 0.41
5		1.17 ± 0.31	1.84 ± 0.53	3.93 ± 0.48	6.11 ± 0.54
6		1.04 ± 0.27	1.78 ± 0.30	3.90 ± 0.38	6.12 ± 0.44
7	5	1.29 ± 0.35	1.95 ± 0.63	3.92 ± 0.44	6.22 ± 0.43
8		0.96 ± 0.32	1.79 ± 0.26	3.92 ± 0.27	5.94 ± 0.41
9	6	1.14 ± 0.37	1.69 ± 0.47	3.91± 0.35	6.00 ± 0.37

and sampling count were 10^5, 10^3, and 10^2 respectively. The MCMC was repeated for 10 times to collect 10^3 samples.

6.3 Results

6.3.1 Fibre Radius Estimates

Fig. 6.3 shows the histograms of R estimates derived from the posterior distribution for each true radius R, and Table 6.2 summarizes the mean and standard deviation (σ) of the distributions for each case. Overall, all of the protocols accurately estimated large radii ($R = 4$ and 6 μm) but produced bias for small radii, especially for R =1 μm; nevertheless, the fibres can be still recognized as a small size.

6.3.2 Effect of b-value

For $M = 3$ (i.e. *Protocol* 1, 2, and 3), a consistent decrease in σ was observed from *Protocol* 1 to *Protocol* 3. The results showed that the precision of R estimate was better at high q- or b-values. A similar finding was observed for $M = 4$: σ tended to decrease from *Protocol* 4 that covered low b-value range to *Protocol* 6 that utilized high b-values. Likewise for $M = 5$, *Protocol* 8 produced a finer precision (i.e. lower σ) than *Protocol* 7.

6.3.3 Effect of q-space Sampling Shells

To study the impact of the number of q-space sampling shells (M), we compared the results between *Protocol* 3 ($M = 3$), 6 ($M = 4$), 8 ($M = 5$), and 9 ($M = 6$), as each of them had the highest precision on R estimate for the corresponding M according to our results above. There were no

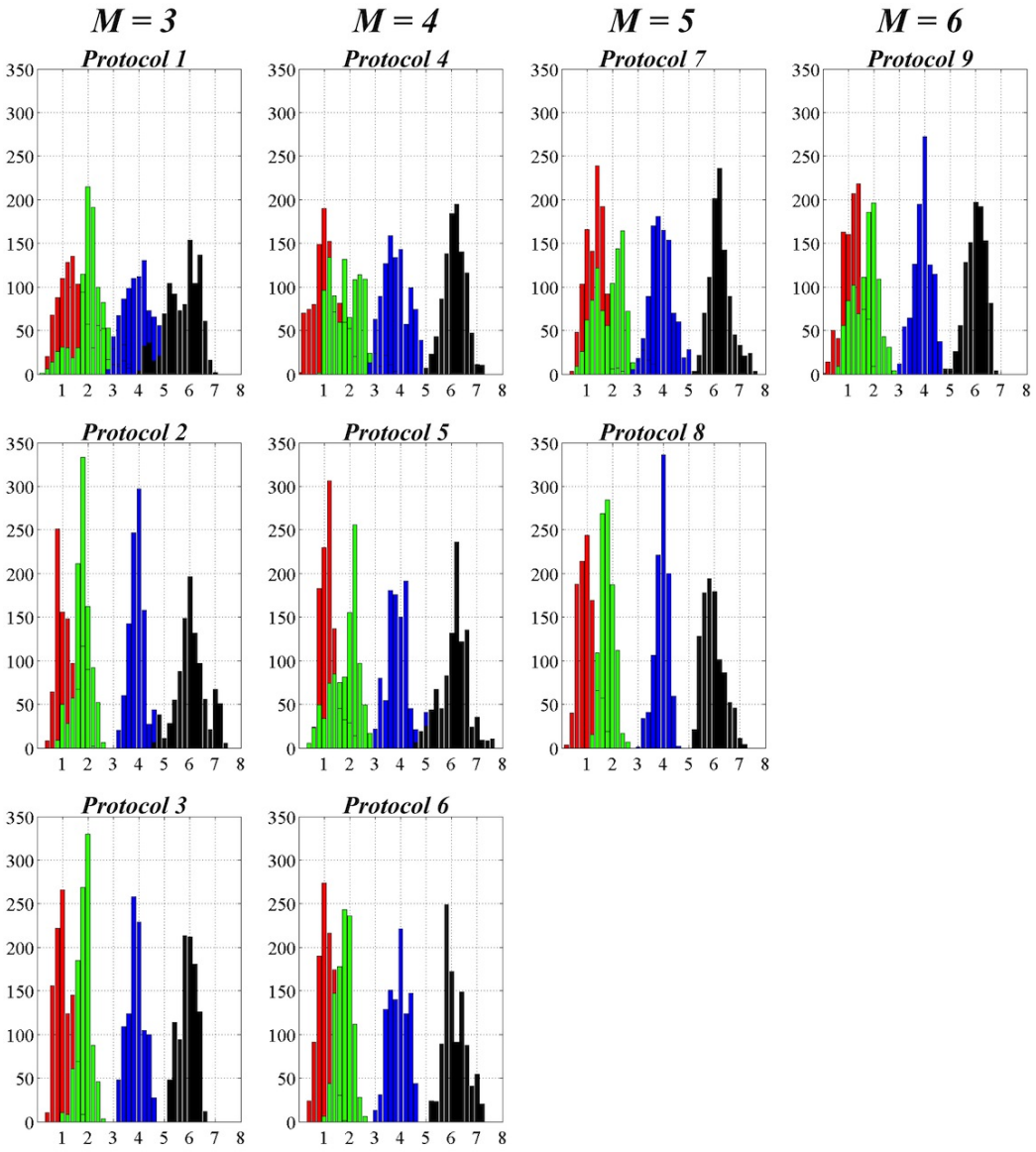

Figure 6.3: Histograms of samples obtained from the MCMC posterior distributions on R. - (Red/green/blue/black: $R = 1/2/4/6$ μm).

significant differences between *Protocol* 3, 6, and 8; all of them showed less overlapping for small radii estimation ($R = 1$ and 2 μm) and produced sharper distribution for larger radii. *Protocol* 9 could estimate large radii ($R = 4$ and 6 μm) but failed to distinguish small radii ($R = 1$ and 2 μm) and produced larger deviations.

6.4 Discussion

The microscopic dMRI technique provides valuable measures directly associated with tissue characteristics. Before applying to a clinical MRI system and acquiring human brain data, this chapter, based on computer simulations, was dedicated to investigate the potential of mi-

croscopic dMRI for the clinical application. We utilized a simulation approach since it provided insights into the mechanisms affecting the signal generation, which we may not be able to appreciate by simply analyzing the real MR data. In addition, simulations allowed us to assess and adapt pulse sequence parameters for understanding their impact on the microscopic imaging. As the DMS enabled us to generate various DW imaging protocols for synthesizing dMRI datasets, we put efforts to design a set of PGSE pulse sequences complied with the capacity of the standard clinical MR scanners in order to translate the methods of direct microstructure estimates to clinically feasible systems.

In the work of [Alexander (2008)], cares have been taken to generate optimal experimental protocols through a mathematical framework minimizing the variance on the parameter estimates for the gradient systems capable of delivering up to 70 mT/m or 200 mT/m. In this study, we designed dMRI respecting the limits of acquisition time, the hardware and safety constraints. First, we kept the maximal gradient strength at 40 mT/m, a standard clinically imposed limit. Second, the purpose of keeping Δ_e at 50 ms was not only to boost the diffusion weighting (reflected in the b-values), but also to approach the time scale where even the sparser restrictions (i.e. for the larger cells) could be sensed by the overall ensemble of diffusing particles. Taking these two conditions together, we proposed a set of PGSE protocols achievable within a clinically acceptable time of around 30 minutes. Although the variance of the estimates deviated somewhat from its optimal value, this study helped us to investigate the impact of each sequence parameter on fibre radius estimation.

Synthetic DW signal can be derived from an analytical or a numerical model. As shown in [Alexander (2008)], simulated DW signal was generated using an analytical expression for the two-compartment system (i.e. the bi-Gaussian mixture model) [Niendorf et al. (1996); Clark and Bihan (2000); Maier et al. (2004)], and the same model was implemented to sample the posterior distributions on the parameter estimates. In this study, we replaced the dMRI signal generation by a step-by-step signal synthesizer based on random walk MC simulations. Even though in the limit of a very large number of particles (10^5 in our case) and of the Gaussian phase approximation [Balinov et al. (1993)], the differences between the signals generated by the two techniques should be negligible. Nevertheless, the random walk technique decoupled the signal generation part from the signal estimation part. Thus, it should cancel any possible bias in the consequent MCMC sampling on the parameter posterior distribution. Furthermore, any potential deviations from the aforementioned statistical limits were taken into account.

In this study, we simulated a simple WM model using a single axonal size with a non-exchangeable cell membrane. Further works are in the process of simulating more realistic WM

fibres of human brains, such as in the presence of cell size distribution. Moreover, Zhang *et al*. have showed the effect of fibre orientation dispersion may not be negligible as it will lead to an overestimation of the cell size [Zhang et al. (2011)]. Axonal membrane permeability should also have a minor influence on mapping WM fibre diameter, although the exchange rate has been proposed to be much slower in myelinated fibres [Quirk et al. (2003)]. In addition, according to the study in the previous chapter (Chapter 5), we have shown that a long diffusion gradient pulse duration (i.e. a finite δ) may limit the resolution of fibre radius mapping, whereas the δ-effect did not seem to be evident in the results presented in this chapter. This may be due to that the T_2 signal attenuation had dominated impact over the δ effect in our simulations, however it requires further clarifications in the future.

According to our simulation results, we observed that b-value was a determinant for the fiber radius estimation. This finding was consistent with the b-values derived from an optimization procedure as demonstrated in [Alexander (2008); Alexander et al. (2010)], where the minimal b-value was 500 s/mm^2. Moreover, we found that introducing low b-values spread out the posterior distribution of MCMC samples. This may be due to that lower b-values enhanced the sensitization towards rapidly diffusing populations and thus, decreased the precision on more slowly moving spins for encoding the size of restrictions. In summary, based on the diffusion signal synthesizer of DMS and an MCMC sampler, we concluded the following: contrary to the scheme underpinned by the equidistant strategy over a large range of q-values [Hansen and Vestergaard-Poulsen (2006); Vestergaard-Poulsen et al. (2007)], sampling moderate to high q- or b-values may be more efficient.

6.5 Conclusion

Within a clinical acceptable acquisition time of 30 minutes, our simulation results showed that using three or four shells with moderate to high b-values was able to deliver the microstructure information using a clinical MR scanner. This study comprises the algorithmic and experimental development, and we believe that the results may advance significantly clinical applications of microscopic dMRI as well as translate the quest for disease biomarkers directly to the clinical practice.

Part IV

CONCLUSION

Chapter 7

Conclusion

Contents

7.1 Summary of Contributions

This section summarizes the achievements of this thesis, which mainly fall into two areas:

I. Methodological Contributions - This thesis has presented a new simulation framework, *Diffusion Microscopist Simulator*, which is adaptable to study various dMRI research topics (Chapter 3).

II. Experimental Contributions - The performance and validity of DMS have been verified through several benchmark experiments (Chapter 4). Based on DMS simulations, this thesis has two major application contributions. In Chapter 5, we have validated that current practice of using long δ is actually beneficial for mapping fibre orientations, even though it does not satisfy the underlying assumption made in the q-space theory. In Chapter 6, we have demonstrated that the microscopic dMRI has the potential to estimate axon radius using a clinical MRI system.

7.2 Discussion on Future Works

This section summarizes the possible extension of DMS and recommendations for future works.

7.2.1 Methodological Aspect

The first generation of DMS is already suitable for various applications, as demonstrated by our benchmark experiments in Chapter 4 and research applications in Chapters 5 & 6. Owing to its framework design, future extension of DMS is straightforward. The following are the ideas of technical improvement for DMS:

I. 3D Mesh-based Reconstruction of Histological Images - The most difficult task in MC simulations of dMRI is likely to be the construction of a 3D simulation scene that is comparable to a biological environment. Neural tissues, for instance, contain different types of cells with diverse sizes and shapes, such as glial cells, astrocytes, neuron bodies, axons, dendrites, etc. Even for the WM fibres, tissue components such as cell nucleus, microfilament, microtubule, or myelin sheath are often ignored in dMRI simulations owing to their complexity. Mathematically modeling each cell type is not practical as the analytical expression for complicated geometries may not exist. In addition, since cells are tightly packed together, i.e. the space between cells are extremely narrow (at a *nanometric* scale), it is a great challenge to

represent those configurations in 3D.

The first generation of DMS can create various axon fibre configurations. The cross section of an axon can be arbitrary shape and the axonal projection can be any curve in 3D. Therefore, it is feasible to construct different axon conditions, such as axon beading [Budde and Frank (2010)] or degeneration [Landman et al. (2010)] model. A network of axons, i.e. fibre bundles, can be built by providing network coordinates, and thus DMS is able to create complex fibre bundles such as crossing, kissing, and branching fibres, as demonstrated in Chapter 4.5. For neuronal cells, however, it is much more difficult to construct randomly distributed but highly compact cells. We are currently in the process of programming a fully automatic algorithm to generate 3D meshes without overlapping in order to perform MC simulations in more complicated neural media, such as those present in brain gray matter.

Another task in progress to build a realistic scene of biological tissue is to directly reconstruct via 3D rendering of binary images scanned from a biological sample, for instance, using electron microscopy. An example is provided by Panagiotaki *et al.*, who succeeded to construct the tissue samples from confocal microscopy images [Panagiotaki et al. (2010)]. A potential technical difficulty of this approach comes from that the histological image is quite thin (∼tens nm) comparing to a reasonable spatial dimension for MC simulations (∼hundreds μm), and therefore it requires more than thousands of histological images which is a huge amount of works for the preparation. The possible solution to this issue is to only model and store a certain number of basic cell types from a small number of histological images. If it is feasible to assume that the distribution of cell types is homogeneous for a specific brain region, then we may fill the MC simulation space by repeatedly placing those basic cellular structures via the automatic positioning algorithm described above.

II. Adaptive Spatial Subvolume - The spatial partition algorithm dividing the global space into the spatial subvolumes has been implemented in DMS in order to increase the computing speed. The algorithm uses a fine grid of the size $N_x \times N_y \times N_z$ decided by the user, without any consideration of the density of polygon meshes. In the future, an *adaptive* partition algorithm will be developed by taking the polygons' distribution into account. It means that a finer grid will be further applied to split the local subvolumes containing more polygons. Likewise, for those containing fewer or no polygons will be merged with the neighboring subvolumes. We expect that it will be helpful to increase the efficiency as well as to save the memory consumption for the MC simulation.

III. Molecular Interactions - In physics, the origin of diffusion mixing comes from the collisions

between molecules in liquids or gases. DMS is possible to model such particle-to-particle (molecule-to-molecule) interaction. For this case, each diffusing particle will update its spatial location following a series of interactions with the surrounding particles and membranes. A specific spatial subvolumes can be also constructed to record particle's locations so as to process interactions with the neighboring particles.

A practical issue to implement the molecular interaction is that each particle is no longer an independent object, and thus parallel processing via multi-threading or distribution on a grid may not be carried out. Thus, it will result in a remarkable increase of the MC simulation time.

IV. MRI Simulator - Stöcker *et al*. have presented a MRI simulator that integrates with the Bloch equation-based model of a spin system, which considers the influence of the off-resonance effects, parallel receive and transmit, nonlinear gradient fields, and spatiotemporal parameter variations at different levels to reflect modern MRI systems [Stöcker et al. (2010)]. The MRI simulator is highly useful in many aspects, such as for the development of new pulse sequences, the design of radiofrequency pulses, and the modeling of the MRI artifacts, etc. However, their simulator does not take the diffusion term into consideration.

The current DMS simulates the dMRI echo signal by modeling the net dephasing caused by water diffusion. In the future, DMS will be extended to model tissue properties including the spin-lattice (T_1) and spin-spin (T_2) relaxation times, which can be assigned to each tissue components according to their properties. The synthesis of overall MRI signal will combine with the Bloch-Torrey equation to model the spin system (Eq. 2.11). This will enable us to simulate and program, for instance, the new dMRI pulse sequences (e.g. MSDI and OGSE methods) as well as the k-space readout strategies (e.g. segmented echo planar imaging) to improve diffusion imaging. In addition, the artifacts that appear in the practical MR images, such as the eddy current, cross-term effects, or magnetic field (i.e. B_0) inhomogeneities can be modeled in order to improve the image quality. The MRI simulator would also be helpful to understand the spin's behavior and to design imaging strategy on the ultra-high field MRI system.

V. GPU-based Computation - An inherent drawback of MC simulation methods to the analyses of dMRI experiments is that a great number of diffusing particles and simulation iteration count (i.e. N_p and N_I) are necessary to reduce the statistical errors. Hall and Alexander [Hall and Alexander (2009)] have proposed that, for a basic dMRI MC simulation of human WM fibres, typically the simulation complexity ($= N_p \times N_I$) has to be greater than 10^8, for in-

stance, using $N_p = 10^5$ and $N_I = 10^3$. For dMRI simulations in biological microstructures, the simulation time step (i.e. t_s) has to be small enough to produce a RMS distance associated with tissue's geometry. For the simulation of a cell membrane's properties, for example, the layer thickness of polar membrane interface is at *nanometric* scale [Le Bihan (2007)], which requires a much smaller t_s so as to reach adequate temporal resolution and prevent from the jump RMS distance effect [Regan and Kuchel (2000)]. However, typical dMRI simulation timescales often span tens to hundreds of milliseconds, it results in a great increase in N_I ($= N_{TE}/t_s$ for DMS). For those cases, a computer equipped with a high computing performance facility is necessary to yield a reasonable simulation time.

Another approach that is possible to improve the computing efficiency for DMS algorithms is to use graphics processing unit (GPU), which is particularly appropriate for parallel computations. The parallel structure of GPUs makes them more efficient than the general-purpose CPUs for algorithms where large blocks of data are processed in parallel. Modern GPUs enable several hundreds of threads to be launched simultaneously, and thus the computing speed of GPU accelerated simulations can be considerably increased. A recent study has demonstrated that the MC simulation of dMRI PGSE experiments may be accelerated by up to three orders of magnitude [Waudby and Christodoulou (2011)]. Furthermore, importantly, the hardware (i.e. the video card) is easily available to install on desktop computers and laptops. I expect that if DMS supports the GPU-based calculation in the future, it will be helpful in several aspects as well as advance its usage.

7.2.2 Experimental and Application Aspect

I. Correlation Between Simulations and Experiments - The simulation method is usually challenged by its intrinsic systematic bias due to the imperfect modeling of realistic conditions. Compared to actual experiments, simulations are often considered as a simplified system. *So why is MC simulation important for diffusion MRI?* MC simulation framework is able to provide the details regarding particles' motion as function of time. Thus, DMS can be used to address specific question about the properties of a model system and parameters, often more straightforwardly than experiments on the actual system. For many aspects of biophysical mechanism, it is these details that are of interest (for instance, what is the impact of cellular permeability on dMRI measures? Likewise, is it possible to measure the membrane permeability by dMRI?). Of course, experiments play an essential role in validating the simulation methodology: comparisons of simulation and experimental data serve to

test the accuracy of the results and to provide criteria for improving the modeling and the methodology.

A significant aspect of simulation is that the features (e.g. cell membrane's shape and property) are completely under the control of users, so that the role of specific property can be examined by altering its attribute. In dMRI, tissue modeling is the task of intensively research in order to clarify the relationship between MRI signal and tissue microscopic characteristics. Budde and Frank provide an excellent example of how simulations and experiments can be complementary tools to study the impact of tissue property [Budde and Frank (2010)]. They constructed a biophysical model for beading axonal membranes, which was validated by the histological evidence of biological nerve fibres, thus highlighting the significant impact of morphological variations of axons on ADC. In their study, the role of simulation offers the flexibility to adjust the magnitude of morphological variations of the axonal membranes, while the role of dMRI experiment verifies the phenomenon in realistic biological conditions.

In the future, DMS will be further applied to investigate different tissue characteristics under healthy and pathological states via cross validation between simulations and experiments. This also reflects the benefit and the need of 3D rendering of histological images for the reconstruction of tissue configuration, as described in the previous section (Chapter 7.2.1). Although DMS simulations were mostly applied to simulate the tissues in the CNS system, DMS has the potential to be broadly applied to different MRI research fields such as diffusion in the porous media [Shemesh et al. (2010a)], the acinar tree of lung [Perez-Sanchez et al. (2009)], etc.

II. Microscopic Diffusion MRI - In recent years, dMRI has had a variety of applications especially for the brain research, however, for the methodological aspect, the analysis of dMRI data seems to approach to a bottleneck in terms of delivering new information about tissue properties. The microscopic dMRI has become a field of interest recently because of its capability of providing the quantities directly associated with tissue characteristics rather than a depiction of tissue-related diffusion behavior given by the current dMRI methods.

One of the main purposes of DMS is to help invent and improve the dMRI methodology, as well as to translate the microscopic dMRI methods onto the human MRI systems. The advantage of DMS is that it is able to simulate a variety of MRI pulse sequences and parameters. In our benchmark experiments described in Chapter 4, we have already demonstrated that DMS is versatile to simulate different kinds of microscopic dMRI methods (i.e. q-space imaging based on the single PGSE, double PGSE sequences, and the temporal diffusion spec-

troscopy based on the OGSE sequence). DMS is also a useful tool for the active imaging paradigm (Chapter 2.5.4) [Alexander (2008)], since it can be applied to synthesize dMRI data to evaluate the results of experimental design (e.g. the optimized gradient waveform for the purpose of fibre diameter mapping [Drobnjak et al. (2010)]).

III. Biophysical Model of Diffusion - Novikov *et al.* have published a series of excellent articles concerning the influence of medium and barriers on water diffusion via theoretical descriptions and 2D simulations [Novikov and Kiselev (2010); Novikov et al. (2011)]. They explain the relationship between the diffusion transport and the effect of permeable barriers, which can be applied to a biological system to quantify the cell membrane permeability and the surface area. These studies are of great help to understand the fundamental diffusion physics in biological tissues. In the future, we will apply DMS to simulate 3D water diffusion in biological systems of various properties, in order to understand the features measured by dMRI. Indeed, the most constructive outcome of *Diffusion Microscopist Simulator* would be its potential to investigate the biophysical mechanisms from the microscopic point of view. Obviously, numerous questions remain without answers yet, nevertheless, the prospect of clarifying the interrelationship between dMRI and the microscopic characteristics of brain tissue is likely to be achievable in the future.

Bibliography

Alexander, D. C.: 2008, 'A general framework for experiment design in diffusion MRI and its application in measuring direct tissue-microstructure features'. *Magn Reson Med* **60**(2), 439–48. [xvi, xviii, xxvii, 4, 28, 37, 99, 100, 101, 102, 105, 106, 115]

Alexander, D. C. and G. J. Barker: 2005, 'Optimal imaging parameters for fiber-orientation estimation in diffusion MRI'. *NeuroImage* **27**(2), 357–67. [89, 95]

Alexander, D. C., P. L. Hubbard, M. G. Hall, E. A. Moore, M. Ptito, G. J. M. Parker, and T. B. Dyrby: 2010, 'Orientationally invariant indices of axon diameter and density from diffusion MRI'. *NeuroImage* **52**(4), 1374–89. [xviii, xxvii, 29, 37, 78, 99, 100, 102, 106]

Amiry-Moghaddam, M. and O. P. Ottersen: 2003, 'The molecular basis of water transport in the brain'. *Nat Rev Neurosci* **4**(12), 991–1001. [xvii, 36]

Assaf, Y. and P. J. Basser: 2005, 'Composite hindered and restricted model of diffusion (CHARMED) MR imaging of the human brain'. *NeuroImage* **27**(1), 48–58. [xxv, 22, 79, 81, 87, 92]

Assaf, Y., T. Blumenfeld-Katzir, Y. Yovel, and P. J. Basser: 2008, 'AxCaliber: a method for measuring axon diameter distribution from diffusion MRI'. *Magn Reson Med* **59**(6), 1347–54. [xvi, xxv, 4, 25, 26, 78, 98]

Assaf, Y., R. Z. Freidlin, G. K. Rohde, and P. J. Basser: 2004, 'New modeling and experimental framework to characterize hindered and restricted water diffusion in brain white matter'. *Magn Reson Med* **52**(5), 965–78. [xvii, xxv, 25, 37, 72, 79, 81, 87, 92, 98]

Avram, L., Y. Assaf, and Y. Cohen: 2004, 'The effect of rotational angle and experimental parameters on the diffraction patterns and micro-structural information obtained from q-space diffusion NMR: implication for diffusion in white matter fibers'. *J Magn Reson* **169**(1), 30–8. [26]

Balinov, B., B. Jonsson, P. Linse, and O. Soderman: 1993, 'The NMR self-diffusion method applied to restricted diffusion. Simulation of echo attenuation from molecules in spheres and between planes'. *J Magn Reson A* **104**, 17–25. [105]

Balls, G. and L. Frank: 2009, 'A simulation environment for diffusion weighted MR experiments in complex media'. *Magn Reson Med* **62**(3), 771–8. [xviii, xix, 37, 38, 41, 56]

Bar-Shir, A., L. Avram, E. Ozarslan, P. J. Basser, and Y. Cohen: 2008, 'The effect of the diffusion time and pulse gradient duration ratio on the diffraction pattern and the structural information estimated from q-space diffusion MR: experiments and simulations'. *J Magn Reson* **194**(2), 230–6. [78, 94]

Barzykin, A.: 1998, 'Exact solution of the Torrey-Bloch equation for a spin echo in restricted geometries'. *Physical Review B* **58**, 14171–4. [xviii, 37]

Basser, P. J., J. Mattiello, and D. L. Bihan: 1994a, 'Estimation of the Effective Self-Diffusion Tensor from the NMR Spin Echo'. *J Magn Reson B* **103**, 247–254. [xvi, 4, 14, 17, 78]

Basser, P. J., J. Mattiello, and D. LeBihan: 1994b, 'MR diffusion tensor spectroscopy and imaging'. *Biophysical Journal* **66**(1), 259–67. [xvi, 4, 14, 20, 64, 78, 98, 102]

Basser, P. J., S. Pajevic, C. Pierpaoli, J. Duda, and A. Aldroubi: 2000, 'In vivo fiber tractography using DT-MRI data'. *Magn Reson Med* **44**(4), 625–32. [xvi, 4, 68, 78, 98]

Basser, P. J. and C. Pierpaoli: 1996, 'Microstructural and physiological features of tissues elucidated by quantitative-diffusion-tensor MRI'. *J Magn Reson B* **111**(3), 209–19. [21, 78, 102]

Basser, P. J. and C. Pierpaoli: 1998, 'A simplified method to measure the diffusion tensor from seven MR images'. *Magn Reson Med* **39**(6), 928–34. [21]

Beaulieu, C.: 2002, 'The basis of anisotropic water diffusion in the nervous system - a technical review'. *NMR Biomed.* **15**(7-8), 435–55. [xvii, 19, 37]

Behrens, T. E. J., H. J. Berg, S. Jbabdi, M. F. S. Rushworth, and M. W. Woolrich: 2007, 'Probabilistic diffusion tractography with multiple fibre orientations: What can we gain?'. *NeuroImage* **34**(1), 144–55. [24, 25, 79]

Blees, M.: 1994, 'The effect of finite duration of gradient pulses on the pulsed-field-gradient NMR method for studying restricted diffusion'. *J Magn Reson.* [17, 79]

Bloch, F.: 1946, 'Nuclear induction'. *Physical Review* **70**, 460–74. [12]

Brown, R.: 1828, 'A brief account of microscopical observations made in the months of June, July, and August 1827 on the particles contained in the pollen of plants; and on the general existence of active molecules in organic and inorganic bodies'. *Philosoph Mag* **44**, 161. [xv, 4, 12]

Budde, M. D. and J. A. Frank: 2010, 'Neurite beading is sufficient to decrease the apparent diffusion coefficient after ischemic stroke'. *Proc Natl Acad Sci USA* **107**(32), 14472–7. [xviii, xix, 37, 38, 42, 111, 114]

Callaghan, P., S. L. Codd, and J. D. Seymour: 1999, 'Spatial coherence phenomena arising from translational spin motion in gradient spin echo experiments'. *Concepts Magn Reson* **11**, 181–202. [17, 79]

Callaghan, P. and J. Stepisnik: 1995, 'Frequency-domain analysis of spin motion using modulated-gradient NMR'. *Journal of Magnetic Resonance Series A* **117**, 118–122. [27]

Callaghan, P. T.: 1993, *Principles of nuclear magnetic resonance microscopy.* Oxford University Press. [xxv, 14, 16, 17, 19, 26, 54, 56, 78, 79, 98]

Caprihan, A., L. Z. Wang, and E. Fukushima: 1996, 'A multiple-narrow-pulse approximation for restricted diffusion in a time-varying field gradient'. *J Magn Reson A* **118**, 94–102. [78]

Carr, H. and E. Purcell: 1954, 'Effects of diffusion on free precession in nuclear magnetic resonance experiments'. *Physical Review* **94**, 630–38. [12]

Chao, Y.-P., K.-H. Cho, C.-H. Yeh, K.-H. Chou, J.-H. Chen, and C.-P. Lin: 2009, 'Probabilistic topography of human corpus callosum using cytoarchitectural parcellation and high angular resolution diffusion imaging tractography'. *Hum Brain Mapp* **30**(10), 3172–87. [25]

Chen, K. C. and C. Nicholson: 2000, 'Changes in brain cell shape create residual extracellular space volume and explain tortuosity behavior during osmotic challenge'. *Proc Natl Acad Sci USA* **97**(15), 8306–11. [xvi, 36]

Chin, C.-L., F. W. Wehrli, Y. Fan, S. N. Hwang, E. D. Schwartz, J. Nissanov, and D. B. Hackney: 2004, 'Assessment of axonal fiber tract architecture in excised rat spinal cord by localized NMR q-space imaging: simulations and experimental studies'. *Magn Reson Med* **52**(4), 733–40. [xvii, 37]

Cho, K.-H., C.-H. Yeh, Y.-P. Chao, J.-J. Wang, J.-H. Chen, and C.-P. Lin: 2009, 'Potential in reducing scan times of HARDI by accurate correction of the cross-term in a hemispherical encoding scheme'. *J Magn Reson Imaging* **29**(6), 1386–94. [84]

Cho, K.-H., C.-H. Yeh, J.-D. Tournier, Y.-P. Chao, J.-H. Chen, and C.-P. Lin: 2008, 'Evaluation of the accuracy and angular resolution of q-ball imaging'. *NeuroImage* **42**(1), 262–71. [67, 72, 82, 93]

Ciccarelli, O., M. Catani, H. Johansen-Berg, C. Clark, and A. Thompson: 2008, 'Diffusion-based tractography in neurological disorders: concepts, applications, and future developments'. *Lancet Neurol* **7**(8), 715–27. [25]

Clark, C. A. and D. L. Bihan: 2000, 'Water diffusion compartmentation and anisotropy at high b values in the human brain'. *Magn Reson Med* **44**(6), 852–9. [30, 105]

Close, T. G., J.-D. Tournier, F. Calamante, L. A. Johnston, I. Mareels, and A. Connelly: 2009, 'A software tool to generate simulated white matter structures for the assessment of fibre-tracking algorithms'. *NeuroImage* **47**(4), 1288–300. [72]

Cohen, Y. and Y. Assaf: 2002, 'High b-value q-space analyzed diffusion-weighted MRS and MRI in neuronal tissues - a technical review'. *NMR Biomed.* **15**(7-8), 516–42. [xvii, 19, 36, 78]

Colvin, D., T. Yankeelov, M. Does, Z. Yue, C. Quarles, and J. Gore: 2008, 'New insights into tumor microstructure using temporal diffusion spectroscopy'. *Cancer Res* **68**(14), 5941. [28]

Conturo, T. E., N. F. Lori, T. S. Cull, E. Akbudak, A. Z. Snyder, J. S. Shimony, R. C. McKinstry, H. Burton, and M. E. Raichle: 1999, 'Tracking neuronal fiber pathways in the living human brain'. *Proc Natl Acad Sci USA* **96**(18), 10422–7. [xvi, 4, 78]

Cooper, R. L., D. B. Chang, A. C. Young, C. J. Martin, and D. Ancker-Johnson: 1974, 'Restricted diffusion in biophysical systems. Experiment'. *Biophysical Journal* **14**(3), 161–77. [xvii, 36]

Cory, D. and A. Garroway: 1990, 'Measurement of translational displacement probabilities by NMR: an indicator of compartmentation'. *Magnetic Resonance in Medicine* pp. 435–44. [xxv, 13, 19, 26, 98]

Darquié, A., J. B. Poline, C. Poupon, H. Saint-Jalmes, and D. L. Bihan: 2001, 'Transient decrease in water diffusion observed in human occipital cortex during visual stimulation'. *Proc Natl Acad Sci USA* **98**(16), 9391–5. [29]

Descoteaux, M., E. Angelino, S. Fitzgibbons, and R. Deriche: 2007, 'Regularized, fast, and robust analytical Q-ball imaging'. *Magn Reson Med* **58**(3), 497–510. [79]

Descoteaux, M., R. Deriche, D. L. Bihan, J.-F. Mangin, and C. Poupon: 2011, 'Multiple q-shell diffusion propagator imaging'. *Med Image Anal* **15**(4), 603–21. [22]

Descoteaux, M., R. Deriche, T. R. Knösche, and A. Anwander: 2009, 'Deterministic and probabilistic tractography based on complex fibre orientation distributions'. *IEEE Trans Med Imaging* **28**(2), 269–86. [25, 64, 68, 72]

Does, M. D., E. C. Parsons, and J. C. Gore: 2003, 'Oscillating gradient measurements of water diffusion in normal and globally ischemic rat brain'. *Magn Reson Med* **49**(2), 206–15. [57, 58]

Drobnjak, I., B. Siow, and D. C. Alexander: 2010, 'Optimizing gradient waveforms for microstructure sensitivity in diffusion-weighted MR'. *J Magn Reson* **206**(1), 41–51. [29, 115]

Einstein, A.: 1905, 'Uber die von der molekularkinetischen Theorie der Warme geforderte Bewegung von in ruhenden Flussigkeiten suspendierten Teilchen'. *Ann Physik* **4**, 549–60. [xv, 4, 12, 15]

Einstein, A.: 1956, *Investigations on the theory of Brownian motion, In R. Furthe and A.D. Cowper, editors*, Collection of papers translated from the German. Dover, New York,. [12, 14]

Fick, A.: 1855, 'On liquid diffusion'. *Philosoph Mag* **10**, 30–39. [12]

Fieremans, E., Y. D. Deene, S. Delputte, M. S. Ozdemir, E. Achten, and I. Lemahieu: 2008a, 'The design of anisotropic diffusion phantoms for the validation of diffusion weighted magnetic resonance imaging'. *Phys Med Biol* **53**(19), 5405–19. [72]

Fieremans, E., Y. D. Deene, S. Delputte, M. S. Ozdemir, Y. D'Asseler, J. Vlassenbroeck, K. Deblaere, E. Achten, and I. Lemahieu: 2008b, 'Simulation and experimental verification of the diffusion in an anisotropic fiber phantom'. *J Magn Reson* **190**(2), 189–99. [xviii, 37, 72]

Fillard, P., M. Descoteaux, A. Goh, S. Gouttard, B. Jeurissen, J. Malcolm, A. Ramirez-Manzanares, M. Reisert, K. Sakaie, F. Tensaouti, T. Yo, J.-F. Mangin, and C. Poupon: 2011, 'Quantitative evaluation of 10 tractography algorithms on a realistic diffusion MR phantom'. *NeuroImage* **56**(1), 220–34. [72]

Finsterbusch, J.: 2009, 'Extension of the double-wave-vector diffusion-weighting experiment to multiple concatenations'. *J Magn Reson* **198**(2), 174–82. [26]

Finsterbusch, J.: 2010, 'Numerical simulations of short-mixing-time double-wave-vector diffusion-weighting experiments with multiple concatenations on whole-body MR systems'. *J Magn Reson* **207**(2), 274–82. [26]

Finsterbusch, J. and M. A. Koch: 2008, 'A tensor approach to double wave vector diffusion-weighting experiments on restricted diffusion'. *J Magn Reson* **195**(1), 23–32. [26]

Flint, J., B. Hansen, P. Vestergaard-Poulsen, and S. J. Blackband: 2009, 'Diffusion weighted magnetic resonance imaging of neuronal activity in the hippocampal slice model'. *NeuroImage* **46**(2), 411–8. [xix, 29, 38, 62]

Ford, J. C., D. B. Hackney, E. Lavi, M. Phillips, and U. Patel: 1998, 'Dependence of apparent diffusion coefficients on axonal spacing, membrane permeability, and diffusion time in spinal cord white matter'. *J Magn Reson Imaging* **8**(4), 775–82. [xviii, 37]

Hagmann, P., L. Cammoun, X. Gigandet, S. Gerhard, P. E. Grant, V. Wedeen, R. Meuli, J.-P. Thiran, C. J. Honey, and O. Sporns: 2010, 'MR connectomics: Principles and challenges'. *J Neurosci Methods* **194**(1), 34–45. [25]

Hagmann, P., L. Cammoun, X. Gigandet, R. Meuli, C. J. Honey, V. J. Wedeen, and O. Sporns: 2008, 'Mapping the structural core of human cerebral cortex'. *PLoS Biol* **6**(7), e159. [25]

Hagmann, P., L. Jonasson, T. Deffieux, R. Meuli, J.-P. Thiran, and V. J. Wedeen: 2006, 'Fibertract segmentation in position orientation space from high angular resolution diffusion MRI'. *NeuroImage* **32**(2), 665–75. [25]

Hagmann, P., M. Kurant, X. Gigandet, P. Thiran, V. J. Wedeen, R. Meuli, and J.-P. Thiran: 2007, 'Mapping human whole-brain structural networks with diffusion MRI'. *PLoS ONE* **2**(7), e597. [25]

Hahn, E.: 1950, 'Spin echoes'. *Physical Review* **80**, 580–594. [12]

Hall, M. G. and D. C. Alexander: 2006, 'Finite pulse widths improve fibre orientation estimates in diffusion tensor MRI'. *ISMRM 14th Scientific Meeting & Exhibition* p. 1076. [79]

Hall, M. G. and D. C. Alexander: 2009, 'Convergence and parameter choice for Monte-Carlo simulations of diffusion MRI'. *IEEE Trans Med Imaging* **28**(9), 1354–64. [xviii, xix, 37, 38, 41, 49, 56, 100, 112]

Hansen, B. and P. Vestergaard-Poulsen: 2006, 'Mapping the parameter space of a T2-dependent model of water diffusion MR in brain tissue'. *Magn Reson Imaging* **24**(8), 1031–8. [106]

Harkins, K. D., J.-P. Galons, T. W. Secomb, and T. P. Trouard: 2009, 'Assessment of the effects of cellular tissue properties on ADC measurements by numerical simulation of water diffusion'. *Magn Reson Med* **62**(6), 1414–22. [xviii, 37]

Hazlewood, C. F., H. E. Rorschach, and C. Lin: 1991, 'Diffusion of water in tissues and MRI'. *Magn Reson Med* **19**(2), 214–6. [xvi, 36]

Hess, C. P., P. Mukherjee, E. T. Han, D. Xu, and D. B. Vigneron: 2006, 'Q-ball reconstruction of multimodal fiber orientations using the spherical harmonic basis'. *Magn Reson Med* **56**(1), 104–17. [72, 79]

Hosey, T., G. Williams, and R. Ansorge: 2005, 'Inference of multiple fiber orientations in high angular resolution diffusion imaging'. *Magn Reson Med* **54**(6), 1480–9. [22, 79]

Hosey, T. P., S. G. Harding, T. A. Carpenter, R. E. Ansorge, and G. B. Williams: 2008, 'Application of a probabilistic double-fibre structure model to diffusion-weighted MR images of the human brain'. *Magnetic resonance imaging* **26**(2), 236–45. [79]

Imae, T., H. Shinohara, M. Sekino, S. Ueno, H. Ohsaki, K. Mima, and K. Ohtomo: 2009, 'Estimation of cell membrane permeability and intracellular diffusion coefficient of human gray matter'. *Magn Reson Med Sci* **8**(1), 1–7. [xviii, 37]

Jansons, K. M. and D. C. Alexander: 2003, 'Persistent angular structure: new insights from diffusion magnetic resonance imaging data'. *Inverse problems* **19**, 1031–46. [22, 79]

Johansen-Berg, H. and T. E. Behrens: 2009, *Diffusion MRI: From quantitative measurement to in-vivo neuroanatomy*. Academic Press. [25]

Jones, D. K., M. A. Horsfield, and A. Simmons: 1999, 'Optimal strategies for measuring diffusion in anisotropic systems by magnetic resonance imaging'. *Magn Reson Med* **42**(3), 515–25. [44, 68, 84]

Kärger, J., H. Pfeifer, and W. Heinik: 1988, 'Principles and application of self-diffusion measurements by nuclear magnetic resonance'. *Adv Magn Reson* **12**, 1–89. [xvii, 37]

King, M. D., J. Houseman, D. G. Gadian, and A. Connelly: 1997, 'Localized q-space imaging of the mouse brain'. *Magn Reson Med* **38**(6), 930–7. [78]

Koch, M. A. and J. Finsterbusch: 2008, 'Compartment size estimation with double wave vector diffusion-weighted imaging'. *Magn Reson Med* **60**(1), 90–101. [26]

Koch, M. A. and J. Finsterbusch: 2009, 'Numerical simulation of double-wave vector experiments investigating diffusion in randomly oriented ellipsoidal pores'. *Magn Reson Med* **62**(1), 247–54. [xviii, 26, 37]

Komlosh, M. E., F. Horkay, R. Z. Freidlin, U. Nevo, Y. Assaf, and P. J. Basser: 2007, 'Detection of microscopic anisotropy in gray matter and in a novel tissue phantom using double Pulsed Gradient Spin Echo MR'. *J Magn Reson* **189**(1), 38–45. [26]

Kroenke, C. D. and J. J. Neil: 2004, 'Use of magnetic resonance to measure molecular diffusion within the brain extracellular space'. *Neurochem Int* **45**(4), 561–8. [xvii, 37]

Landman, B. A., J. A. D. Farrell, S. A. Smith, D. S. Reich, P. A. Calabresi, and P. C. M. van Zijl: 2010, 'Complex geometric models of diffusion and relaxation in healthy and damaged white matter'. *NMR Biomed.* **23**(2), 152–62. [xviii, xix, 37, 38, 41, 111]

Latour, L. L., K. Svoboda, P. P. Mitra, and C. H. Sotak: 1994, 'Time-dependent diffusion of water in a biological model system'. *Proc Natl Acad Sci USA* **91**(4), 1229–33. [xvii, 36]

Lätt, J., M. Nilsson, C. Malmborg, H. Rosquist, R. Wirestam, F. St**r**ahlberg, D. Topgaard, and S. Brockstedt: 2007, 'Accuracy of q-space related parameters in MRI: simulations and phantom measurements'. *IEEE Trans Med Imaging* **26**(11), 1437–47. [78, 94]

Lauterbur, P.: 1973, 'Image formation by induced local interactions: examples em- ploying nuclear magnetic resonance'. *Nature* **242**, 190–191. [13]

Lazar, M.: 2010, 'Mapping brain anatomical connectivity using white matter tractography'. *NMR Biomed.* **23**(7), 821–35. [25]

Le Bihan, D.: 2003, 'Looking into the functional architecture of the brain with diffusion MRI'. *Nat Rev Neurosci* **4**(6), 469–80. [xvi, xviii, 19, 31, 36, 38]

Le Bihan, D.: 2007, 'The 'wet mind': water and functional neuroimaging'. *Phys Med Biol* **52**(7), R57–90. [4, 29, 30, 42, 44, 45, 58, 60, 61, 62, 63, 72, 113]

Le Bihan, D. and E. Breton: 1985, 'Imagerie de diffusion in vivo par résonance magnétique nucléaire'. *Comptes-Rendus de l' Académie des Sciences* **301**(15), 1109–12. [13]

Le Bihan, D., E. Breton, D. Lallemand, P. Grenier, E. Cabanis, and M. Laval-Jeantet: 1986, 'MR imaging of intravoxel incoherent motions: application to diffusion and perfusion in neurologic disorders'. *Radiology* **161**(2), 401–7. [xv, xvi, xvii, 4, 5, 13, 19, 20, 36, 37]

Le Bihan, D., S. Urayama, T. Aso, T. Hanakawa, and H. Fukuyama: 2006, 'Direct and fast detection of neuronal activation in the human brain with diffusion MRI'. *Proc Natl Acad Sci USA* **103**(21), 8263–8. [xvi, 4, 29, 31, 62]

Lin, C. P., W. Y. Tseng, H. C. Cheng, and J. H. Chen: 2001, 'Validation of diffusion tensor magnetic resonance axonal fiber imaging with registered manganese-enhanced optic tracts'. *NeuroImage* **14**(5), 1035–47. [72]

Lin, C.-P., V. J. Wedeen, J.-H. Chen, C. Yao, and W.-Y. I. Tseng: 2003, 'Validation of diffusion spectrum magnetic resonance imaging with manganese-enhanced rat optic tracts and ex vivo phantoms'. *NeuroImage* **19**(3), 482–95. [22, 72, 79, 94]

Lipinski, H. G.: 1990, 'Monte Carlo simulation of extracellular diffusion in brain tissues'. *Phys Med Biol* **35**(3), 441–7. [xviii, xix, 37, 38]

Lori, N. F., T. E. Conturo, and D. L. Bihan: 2003, 'Definition of displacement probability and diffusion time in q-space magnetic resonance measurements that use finite-duration diffusion-encoding gradients'. *J Magn Reson* **165**(2), 185–95. [78]

Maier, S. E., S. Vajapeyam, H. Mamata, C.-F. Westin, F. A. Jolesz, and R. V. Mulkern: 2004, 'Biexponential diffusion tensor analysis of human brain diffusion data'. *Magn Reson Med* **51**(2), 321–30. [30, 105]

Mansfield, P.: 1977, 'Multi-planar image formation using NMR spin echoes'. *J Phys C* **10**, 55–58. [13]

Miller, K. L., D. P. Bulte, H. Devlin, M. D. Robson, R. G. Wise, M. W. Woolrich, P. Jezzard, and T. E. J. Behrens: 2007, 'Evidence for a vascular contribution to diffusion FMRI at high b value'. *Proc Natl Acad Sci USA* **104**(52), 20967–72. [xvii, 37]

Mitra, P. P.: 1995, 'Multiple wave-vector extensions of the NMR pulsed-field-gradient spin-echo diffusion measurement'. *Physical Review B* **51**(21), 15074–15078. [26]

Mitra, P. P. and B. I. Halperin: 1995, 'Effects of finite gradient-pulse widths in pulsed-field-gradient diffusion measurements'. *J Magn Reson A* **113**, 94–101. [xxiv, 78, 79, 80, 94]

Mori, S., B. J. Crain, V. P. Chacko, and P. C. van Zijl: 1999, 'Three-dimensional tracking of axonal projections in the brain by magnetic resonance imaging'. *Ann Neurol* **45**(2), 265–9. [xvi, 4]

Mori, S. and P. C. M. van Zijl: 2002, 'Fiber tracking: principles and strategies - a technical review'. *NMR Biomed.* **15**(7-8), 468–80. [24, 78]

Moseley, M., J. Kucharczyk, H. Asgari, and D. Norman: 1991, 'Anisotropy in diffusion-weighted MRI'. *Magn Reson Med* **19**, 321–26. [20]

Moseley, M. E., Y. Cohen, J. Mintorovitch, L. Chileuitt, H. Shimizu, J. Kucharczyk, M. F. Wendland, and P. R. Weinstein: 1990a, 'Early detection of regional cerebral ischemia in cats: comparison of diffusion- and T2-weighted MRI and spectroscopy'. *Magn Reson Med* **14**(2), 330–46. [13, 20]

Moseley, M. E., J. Kucharczyk, J. Mintorovitch, Y. Cohen, J. Kurhanewicz, N. Derugin, H. Asgari, and D. Norman: 1990b, 'Diffusion-weighted MR imaging of acute stroke: correlation with T2-weighted and magnetic susceptibility-enhanced MR imaging in cats'. *AJNR Am J Neuroradiol* **11**(3), 423–9. [20, 62]

Neeman, M., J. P. Freyer, and L. O. Sillerud: 1991, 'A simple method for obtaining cross-term-free images for diffusion anisotropy studies in NMR microimaging'. *Magn Reson Med* **21**(1), 138–143. [83, 84]

Nicholson, C. and J. Phillips: 1981, 'Ion diffusion modified by tortuosity and volume fraction in the extracellular micorenvrionment of the rat cerebellum'. *J Physiol* **321**, 225–57. [xvi, 36]

Niendorf, T., R. M. Dijkhuizen, D. G. Norris, M. van Lookeren Campagne, and K. Nicolay: 1996, 'Biexponential diffusion attenuation in various states of brain tissue: implications for diffusion-weighted imaging'. *Magn Reson Med* **36**(6), 847–57. [30, 105]

Nilsson, M., E. Alerstam, R. Wirestam, F. Staohlberg, S. Brockstedt, and J. Latt: 2010, 'Evaluating the accuracy and precision of a two-compartment Kärger model using Monte Carlo simulations'. *J Magn Reson* **206**(1), 59–67. [xviii, 37]

Novikov, D. S., E. Fieremans, J. H. Jensen, and J. A. Helpern: 2011, 'Random walks with barriers'. *Nature physics* **7**(6), 508–514. [115]

Novikov, D. S. and V. G. Kiselev: 2010, 'Effective medium theory of a diffusion-weighted signal'. *NMR Biomed.* **23**(7), 682–97. [115]

Novikov, E. G., D. van Dusschoten, and H. V. As: 1998, 'Modeling of self-diffusion and relaxation time NMR in multi-compartment systems'. *J Magn Reson* **135**(2), 522–8. [xvii, 37]

Ogawa, S., T. Lee, A. R. Kay, and D. W. Tank: 1990, 'Brain magnetic resonance imaging with contrast dependent on blood oxygenation'. *Proc Natl Acad Sci USA* **87**, 9868–72. [29]

Ong, H. H., A. C. Wright, S. L. Wehrli, A. Souza, E. D. Schwartz, S. N. Hwang, and F. W. Wehrli: 2008, 'Indirect measurement of regional axon diameter in excised mouse spinal cord with q-space imaging: simulation and experimental studies'. *NeuroImage* **40**(4), 1619–32. [78, 98]

Ozarslan, E.: 2009, 'Compartment shape anisotropy (CSA) revealed by double pulsed field gradient MR'. *J Magn Reson* **199**(1), 56–67. [xxvii, 22, 26, 98]

Ozarslan, E. and P. J. Basser: 2007, 'MR diffusion - "diffraction" phenomenon in multi-pulse-field-gradient experiments'. *J Magn Reson* **188**(2), 285–94. [26, 56]

Ozarslan, E. and P. J. Basser: 2008, 'Microscopic anisotropy revealed by NMR double pulsed field gradient experiments with arbitrary timing parameters'. *J Chem Phys* **128**(15), 154511. [xxvii, 26, 56, 98]

Ozarslan, E., N. Shemesh, and P. J. Basser: 2009, 'A general framework to quantify the effect of restricted diffusion on the NMR signal with applications to double pulsed field gradient NMR experiments'. *J Chem Phys* **130**(10), 104702. [xxvii, 26, 98]

Ozarslan, E., T. M. Shepherd, B. C. Vemuri, S. J. Blackband, and T. H. Mareci: 2006, 'Resolution of complex tissue microarchitecture using the diffusion orientation transform (DOT)'. *NeuroImage* **31**(3), 1086–103. [79]

Panagiotaki, E., M. Hall, H. Zhang, B. Siow, M. Lythgoe, and D. Alexander: 2010, 'High-fidelity meshes from tissue samples for diffusion MRI simulations'. *Medical Image Computing and Computer-Assisted Intervention–MICCAI 2010* pp. 404–411. [111]

Parsons, E., M. Does, and J. Gore: 2003, 'Modified oscillating gradient pulses for direct sampling of the diffusion spectrum suitable for imaging sequences'. *Magnetic resonance imaging* **21**(3-4), 279–285. [28]

Peled, S.: 2007, 'New perspectives on the sources of white matter DTI signal'. *IEEE Trans Med Imaging* **26**(11), 1448–55. [xvii, xviii, 37]

Peled, S., D. Cory, S. Raymond, D. Kirschner, and F. Jolesz: 1999, 'Water diffusion, T2, and compartmentation in frog sciatic nerve'. *Magn Reson Med* **42**(5), 911–918. [30]

Perez-Sanchez, J. M., I. Rodriguez, and J. Ruiz-Cabello: 2009, 'Random Walk Simulation of the MRI Apparent Diffusion Coefficient in a Geometrical Model of the Acinar Tree'. *Biophysj* **97**(2), 656–664. [114]

Perrin, M., C. Poupon, Y. Cointepas, B. Rieul, N. Golestani, C. Pallier, D. Rivière, A. Constantinesco, D. L. Bihan, and J. F. Mangin: 2005a, 'Fiber tracking in q-ball fields using regularized particle trajectories'. *Inf Process Med Imaging* **19**, 52–63. [68]

Perrin, M., C. Poupon, B. Rieul, P. Leroux, A. Constantinesco, J.-F. Mangin, and D. Lebihan: 2005b, 'Validation of q-ball imaging with a diffusion fibre-crossing phantom on a clinical scanner'. *Philos Trans R Soc Lond, B, Biol Sci* **360**(1457), 881–91. [72]

Poupon, C., C. A. Clark, V. Frouin, J. Régis, I. Bloch, D. L. Bihan, and J. Mangin: 2000, 'Regularization of diffusion-based direction maps for the tracking of brain white matter fascicles'. *NeuroImage* **12**(2), 184–95. [xvi, 4, 68]

Poupon, C., B. Rieul, I. Kezele, M. Perrin, F. Poupon, and J.-F. Mangin: 2008, 'New diffusion phantoms dedicated to the study and validation of high-angular-resolution diffusion imaging (HARDI) models'. *Magn Reson Med* **60**(6), 1276–83. [72]

Price, W.: 1997, 'Pulsed-field gradient nuclear magnetic resonance as a tool for studying translational diffusion: Part 1. Basic theory'. *Concepts Magn Reson* **9**(5), 299–336. [16]

Purcell, E., H. Torrey, and R. Pound: 1946, 'Resonance absorption by nuclear magnetic moments in a solid'. *Physical Review* **69**, 37. [12]

Quirk, J. D., G. L. Bretthorst, T. Q. Duong, A. Z. Snyder, C. S. Springer, J. J. H. Ackerman, and J. J. Neil: 2003, 'Equilibrium water exchange between the intra- and extracellular spaces of mammalian brain'. *Magn Reson Med* **50**(3), 493–9. [26, 92, 106]

Regan, D. G. and P. W. Kuchel: 2000, 'Mean residence time of molecules diffusing in a cell bounded by a semi-permeable membrane: Monte Carlo simulations and an expression relating membrane transition probability to permeability'. *Eur Biophys J* **29**(3), 221–7. [113]

Regan, D. G. and P. W. Kuchel: 2002, 'Simulations of molecular diffusion in lattices of cells: insights for NMR of red blood cells'. *Biophysical Journal* **83**(1), 161–71. [63]

Schwarcz, A., P. Bogner, P. Meric, J.-L. Correze, Z. Berente, J. Pál, F. Gallyas, T. Doczi, B. Gillet, and J.-C. Beloeil: 2004, 'The existence of biexponential signal decay in magnetic resonance diffusion-weighted imaging appears to be independent of compartmentalization'. *Magn Reson Med* **51**(2), 278–85. [xvii, 37]

Seunarine, K. K. and D. C. Alexander: 2009, *Multiple fibers: beyond the diffusion tensor. In Diffusion MRI: from quantitative measurement to in vivo neuroanatomy (Editors: Timothy E J Behrens and H Johansen-Berg)*. 55-72. Elsevier. [22]

Shemesh, N. and Y. Cohen: 2008, 'The effect of experimental parameters on the signal decay in double-PGSE experiments: Negative diffractions and enhancement of structural information'. *J Magn Reson* **195**(2), 153–161. [xxvii, 98]

Shemesh, N., E. Ozarslan, T. Adiri, P. J. Basser, and Y. Cohen: 2010a, 'Noninvasive bipolar double-pulsed-field-gradient NMR reveals signatures for pore size and shape in polydisperse, randomly oriented, inhomogeneous porous media'. *J Chem Phys* **133**(4), 044705. [xxvii, 56, 98, 99, 114]

Shemesh, N., E. Özarslan, A. Bar-Shir, P. J. Basser, and Y. Cohen: 2009a, 'Observation of restricted diffusion in the presence of a free diffusion compartment: Single- and double-PFG experiments'. *J Magn Reson* **200**(2), 214–225. [xxvii, 26, 54, 56, 72, 98]

Shemesh, N., E. Özarslan, P. J. Basser, and Y. Cohen: 2009b, 'Measuring small compartmental dimensions with low-q angular double-PGSE NMR: The effect of experimental parameters on signal decay'. *J Magn Reson* **198**(1), 15–23. [xxvii, 26, 56, 98]

Shemesh, N., E. Ozarslan, P. J. Basser, and Y. Cohen: 2010b, 'Detecting diffusion-diffraction patterns in size distribution phantoms using double-pulsed field gradient NMR: Theory and experiments'. *J Chem Phys* **132**(3), 034703. [xxvii, 56, 98]

Shemesh, N., E. Ozarslan, M. E. Komlosh, P. J. Basser, and Y. Cohen: 2010c, 'From single-pulsed field gradient to double-pulsed field gradient MR: gleaning new microstructural information and developing new forms of contrast in MRI'. *NMR Biomed.* **23**(7), 757–80. [98]

Stanisz, G. J., A. Szafer, G. A. Wright, and R. M. Henkelman: 1997, 'An analytical model of restricted diffusion in bovine optic nerve'. *Magn Reson Med* **37**(1), 103–11. [xvii, 37]

Stejskal, E. and J. Tanner: 1965, 'Spin diffusion measurements: spin echoes in the presence of a time-dependent field gradient'. *J Chem Phys* **42**, 288–92. [13, 16]

Stepisnik, J.: 1993, 'Time-dependent self-diffusion by NMR spin-echo'. *Physica B: Condensed Matter* **183**(4), 343–350. [xxv, 27, 58, 98]

Stöcker, T., K. Vahedipour, D. Pflugfelder, and N. J. Shah: 2010, 'High-performance computing MRI simulations'. *Magn Reson Med* **64**(1), 186–93. [112]

Torrey, H.: 1956, 'Bloch equations with diffusion terms'. *Physical Review* **104**, 563–65. [13, 16]

Tournier, J.-D., F. Calamante, and A. Connelly: 2007, 'Robust determination of the fibre orientation distribution in diffusion MRI: non-negativity constrained super-resolved spherical deconvolution'. *NeuroImage* **35**(4), 1459–72. [79]

Tournier, J.-D., F. Calamante, D. G. Gadian, and A. Connelly: 2004, 'Direct estimation of the fiber orientation density function from diffusion-weighted MRI data using spherical deconvolution'. *NeuroImage* **23**(3), 1176–85. [22, 79]

Tournier, J.-D., S. Mori, and A. Leemans: 2011, 'Diffusion tensor imaging and beyond'. *Magn Reson Med* **65**(6), 1532–56. [22]

Tournier, J.-D., C.-H. Yeh, F. Calamante, K.-H. Cho, A. Connelly, and C.-P. Lin: 2008, 'Resolving crossing fibres using constrained spherical deconvolution: validation using diffusion-weighted imaging phantom data'. *NeuroImage* **42**(2), 617–25. [72, 82, 87, 94]

Tuch, D. S.: 2004, 'Q-ball imaging'. *Magn Reson Med* **52**(6), 1358–72. [22, 72, 79, 81, 84, 87]

van der Weerd, L., S. M. Melnikov, F. J. Vergeldt, E. G. Novikov, and H. V. As: 2002, 'Modelling of self-diffusion and relaxation time NMR in multicompartment systems with cylindrical geometry'. *J Magn Reson* **156**(2), 213–21. [xvii, 37]

Vestergaard-Poulsen, P., B. Hansen, L. Ostergaard, and R. Jakobsen: 2007, 'Microstructural changes in ischemic cortical gray matter predicted by a model of diffusion-weighted MRI'. *J Magn Reson Imaging* **26**(3), 529–40. [106]

Wang, L., A. Caprihan, and E. Fukushima: 1995, 'The narrow-pulse criterion for pulsed-gradient spin-echo diffusion measurements'. *J Magn Reson A* **117**(2), 209–19. [18]

Waudby, C. A. and J. Christodoulou: 2011, 'GPU accelerated Monte Carlo simulation of pulsed-field gradient NMR experiments'. *J Magn Reson* **211**(1), 67–73. [113]

Wedeen, V. J., P. Hagmann, W.-Y. I. Tseng, T. G. Reese, and R. M. Weisskoff: 2005, 'Mapping complex tissue architecture with diffusion spectrum magnetic resonance imaging'. *Magn Reson Med* **54**(6), 1377–86. [22, 79, 87, 94]

Wedeen, V. J., R. P. Wang, J. D. Schmahmann, T. Benner, W. Y. I. Tseng, G. Dai, D. N. Pandya, P. Hagmann, H. D'Arceuil, and A. J. de Crespigny: 2008, 'Diffusion spectrum magnetic resonance imaging (DSI) tractography of crossing fibers'. *NeuroImage* **41**(4), 1267–77. [25]

Wesbey, G., M. Moseley, and R. Ehman: 1984a, 'Translational molecular self-diffusion in magnetic resonance imaging. I. Effects on observed spin-spin relaxation.'. *Invest Radiol* **19**, 484–90. [xv, 4, 13, 20]

Wesbey, G., M. Moseley, and R. Ehman: 1984b, 'Translational molecular self-diffusion in magnetic resonance imaging. II. Measurement of the self-diffusion coefficient.'. *Invest Radiol* **19**, 491–98. [xv, 4, 13, 20]

Wheeler-Kingshott, C. A. M. and M. Cercignani: 2009, 'About "axial" and "radial" diffusivities'. *Magn Reson Med* **61**(5), 1255–60. [xvii, 37]

Wiegell, M. R., H. B. Larsson, and V. J. Wedeen: 2000, 'Fiber crossing in human brain depicted with diffusion tensor MR imaging'. *Radiology* **217**(3), 897–903. [21]

Wright, A. and H. Nukada: 1994, 'Sciatic nerve morphology and morphometry in mature rats with streptozocin-induced diabetes'. *Acta neuropathol* **88**(6), 571–578. [83]

Wu, Y.-C. and A. L. Alexander: 2007, 'Hybrid diffusion imaging'. *NeuroImage* **36**(3), 617–29. [79, 87]

Xu, J., M. D. Does, and J. C. Gore: 2009a, 'Quantitative characterization of tissue microstructure with temporal diffusion spectroscopy'. *J Magn Reson* **200**(2), 189–97. [xxvii, 57, 58, 98]

Xu, J., M. D. Does, and J. C. Gore: 2009b, 'Sensitivity of MR diffusion measurements to variations in intracellular structure: Effects of nuclear size'. *Magn Reson Med* **61**(4), 828–833. [xxvii, 28, 98]

Yablonskiy, D. A., G. L. Bretthorst, and J. J. H. Ackerman: 2003, 'Statistical model for diffusion attenuated MR signal'. *Magn Reson Med* **50**(4), 664–9. [xvii, 37]

Yeh, C.-H., K.-H. Cho, H.-C. Lin, J.-J. Wang, and C.-P. Lin: 2008, 'Reduced encoding diffusion spectrum imaging implemented with a bi-Gaussian model'. *IEEE Trans Med Imaging* **27**(10), 1415–24. [22, 23, 82]

Zhan, W. and Y. Yang: 2006, 'How accurately can the diffusion profiles indicate multiple fiber orientations? A study on general fiber crossings in diffusion MRI'. *J Magn Reson* **183**(2), 193–202. [87, 94]

Zhang, H., P. L. Hubbard, G. J. M. Parker, and D. C. Alexander: 2011, 'Axon diameter mapping in the presence of orientation dispersion with diffusion MRI'. *NeuroImage* **56**(3), 1301–15. [29, 106]